

**Thermodynamics of finite-momentum states : from
degenerate atomic gases to helical magnets**

by

Sungsoo Choi

B.A., Seoul National University, 2003

M.S., Tufts University, 2005

A thesis submitted to the
Faculty of the Graduate School of the
University of Colorado in partial fulfillment
of the requirements for the degree of
Doctor of Philosophy
Department of Physics

2012

This thesis entitled:
Thermodynamics of finite-momentum states : from degenerate atomic gases to helical magnets
written by Sungsoo Choi
has been approved for the Department of Physics

Leo Radzihovsky

Victor Gurarie

Date _____

The final copy of this thesis has been examined by the signatories, and we find that both the content and the form meet acceptable presentation standards of scholarly work in the above mentioned discipline.

Choi, Sungsoo (Ph.D., Physics)

Thermodynamics of finite-momentum states : from degenerate atomic gases to helical magnets

Thesis directed by Professor Leo Radzihovsky

We present a theoretical study of finite momentum states in the context of degenerate gases and iron-based magnet. The unifying theme of these seemingly disparate states of condensed matter is the finite momentum of their respective ground states and the associated enhanced fluctuations.

For the degenerate atomic gases, we study in the first part of the thesis a system of two species of bosonic atoms interacting through a p -wave Feshbach resonance as realized in Rubidium-85/Rubidium-87 mixture. In mapping out the phase diagram, we show that the system exhibits atomic (ASF), molecular (MSF) and atomic-molecular (AMSF) superfluid phases, where atoms, molecules, and atoms and molecules Bose condense, respectively. The ASF and MSF states are respectively characterized by a nonzero s -wave atomic and p -wave (orbital) spinor molecular condensates. The AMSF is distinguished by the presence of both of these condensates, with the s -wave atomic condensate component necessarily periodically modulated at a wavevector that is tunable with a magnetic field; that is, generically AMSF is a robust supersolid, that simultaneously breaks spatial translational and gauge symmetries. We explore the rich phenomenology of these phases and phase transitions between them, that we find to be strongly influenced by the quantum and thermal fluctuations.

In the second part of the thesis, we study magnetism in Fe_{1+y}Te , a parent compound of the iron-based high-temperature superconductors. Motivated by earlier studies that have provided evidences of finite momentum spiral states in these materials, we show that a spin-1 exchange model, supplemented by a single-ion anisotropy accounts well for the experimentally observed magnetic phase diagram, that prominently exhibits commensurate bi-collinear and incommensurate spin-spiral orders with the associated low-energy spin-wave spectra. We derive the low energy hydrodynamic models for these magnetic states and use it to describe the magneto-structural and

commensurate-incommensurate transitions, and the static and dynamic structure functions across temperature - Fe doping phase diagram.

Dedication

To my parents, daughter Lyla Yoonjeong, and my wife Sanghee.

Acknowledgements

It has been a long journey in the world of physics and there are so many people I cannot forget. Here I would like to mention the most important connections in my life.

First and foremost, I thank Leo. Since he allowed me to work with him, he gave full support on me. Leo is such a brilliant and exceptional physicist. He was available 24 hours no matter how simple question I asked. Furthermore his dedication to his work and family made me think about my life. I cannot thank more and it was such a great privilege for me to have Leo as my advisor.

For the second part of my thesis, I thank Gang. He is one of the smartest physicist I have ever met, and I was so lucky to work with him and learn from him. He was always the last guy who stayed at the Gamow tower at night and I will never forget him.

I thank my office buddies, Quan and Ke, who have endured me over very long times. Not only they helped me to understand physics, they always help me to overcome any trouble I had. It was a great fun to work for the Boulder summer school too. I could not finish my study without their help.

Jaehyung and Jonghyoun are two friends who I have discussed most during my time in CU. Our discussion went from physics to our daily lives and they were always trying to help me.

I would like to thank my committee members, Victor, Eric, Ana Maria, Andrew, and Dmitry (even though he was not in my committee) for their time and critical comment, and their support for my work. It was a great privilege to have distinguished scientists in my committee.

I would also like to thank my teachers, Mike, Matt and Henry for giving me unforgettable lectures. Especially I was so impressed by Mike for his clear and insightful explanation of condensed

matter physics.

There are so many physics crews, Haeyoung, Jiyong, Soobong, Eungook, Changhyun, Daesoo, Chiho, and others from Seoul National University, and Ron, Brian, John, Jer, Jesper, James, Eddie, Shuming, Xiao, and others from CU, and Seungryong, Zinseok, Dongki, Dr. Yeongwoo Yi, Dr. Cheolsoo Park, Dr. Taewoo Lee, Dr. Junseong Heo, from Korean Lunch group, who helped and supported me always and I will not forget.

I would like to thank my old friends, Yeojoon, Junwon, Jihoon, Jaehong, Jinho, Seongsoon, Kunpil, and Joongun.

Yeongyun and Miyoung helped me to start and finish my life in boulder. I would like to thank them too.

Finally I would like to thank my family. I want to thank my parents who always supported me no matter what happened. I want to thank Sanghee, my beautiful wife and Lyla (Yoonjeong), my beautiful daughter. They were always behind me and I would not finish my work without them.

Contents

| Chapter | |
|---|----|
| 1 Introduction | 1 |
| 1.1 Overall Background | 1 |
| 1.2 Degenerate atomic gases | 2 |
| 1.3 Iron-based superconductors and antiferromagnets | 4 |
| 1.4 Theoretical and experimental motivation | 5 |
| 1.5 Outline of the thesis | 7 |
| 2 p -wave resonant Bose gas | 9 |
| 2.1 Introduction | 9 |
| 2.1.1 Background and Motivation | 9 |
| 2.1.2 Summary of results | 11 |
| 2.2 Model | 16 |
| 2.3 Phases and their symmetries | 21 |
| 2.3.1 Atomic superfluid phases, ASF | 22 |
| 2.3.2 Molecular superfluid phases, MSF | 23 |
| 2.3.3 Atomic-molecular superfluid phases, AMSF | 24 |
| 2.4 Mean Field Theory | 28 |
| 2.4.1 Order parameters | 28 |
| 2.4.2 Atomic Superfluid (ASF) | 30 |

| | | |
|----------|---|-----------|
| 2.4.3 | Molecular Superfluid (MSF) | 32 |
| 2.4.4 | Atomic Molecular Superfluid (AMSF) | 33 |
| 2.5 | Elementary excitations | 42 |
| 2.5.1 | ASF phases | 44 |
| 2.5.2 | MSF phases | 46 |
| 2.5.3 | AMSF phases | 52 |
| 2.6 | Phase Transitions | 59 |
| 2.6.1 | MSF_p - AMSF_p polar transition | 59 |
| 2.6.2 | MSF_{fm} - AMSF_{fm} ferromagnetic transition | 61 |
| 2.7 | Topological Defects | 62 |
| 2.7.1 | Defects in ASF | 63 |
| 2.7.2 | Defects in MSF | 64 |
| 2.7.3 | Defects in AMSF | 65 |
| 2.8 | Local Density Approximation | 67 |
| 2.9 | Summary and Conclusions | 70 |
| 3 | Finite momentum phase of Fe_{1+y}Te | 72 |
| 3.1 | Introduction | 72 |
| 3.1.1 | Iron-based superconductors and magnetism | 72 |
| 3.1.2 | Summary of results | 74 |
| 3.2 | Model of FeTe | 77 |
| 3.2.1 | Microscopic model | 77 |
| 3.2.2 | Effective continuum model | 82 |
| 3.2.3 | Magnetoelastic coupling for the single-ion anisotropy | 85 |
| 3.3 | Magnetostructural transition | 87 |
| 3.4 | Ordered state and commensurate-incommensurate transition | 91 |
| 3.4.1 | Dynamic structure function in the soliton regime | 94 |

| | | |
|-------|---|-----|
| 3.5 | Structure function for Fe_{1+y}Te | 96 |
| 3.5.1 | Static structure function in paramagnetic state, PM_O | 97 |
| 3.5.2 | Dynamic structure function in paramagnetic state, PM_O | 100 |
| 3.5.3 | Dynamic structure function in planar spiral state | 103 |
| 3.6 | Summary and Conclusion | 110 |
| 4 | Conclusions and outlook | 111 |
| | Bibliography | 113 |
| | Appendix | |
| A | Order parameter structure of AMSF phase | 124 |

Figures

Figure

- 2.1 Schematic temperature-detuning phase diagram for a balanced two-species p -wave resonant Bose gas. As illustrated, it exhibits atomic (ASF), molecular (MSF), and atomic-molecular (AMSF) superfluid phases. The novel AMSF state is characterized by a p -wave, molecular and a finite-momentum Q (see Fig. 2.2) atomic superfluidity. 11
- 2.2 Schematic momentum $Q(\nu)$ characteristic of the AMSF (polar) state, ranging between zero and the p -wave FR width-dependent value. 12
- 2.3 A cartoon of a p -wave molecule decaying into two oppositely moving two species of atoms, illustrating a resonant mechanism for a finite momentum \mathbf{Q} atomic superfluidity (indicated by wavy lines) in the AMSF phase. 13
- 2.4 Schematic of the AMSF_p polar state. The thick arrow indicates the atomic condensate momentum \mathbf{Q} and the \hat{n} arrow denotes the quantization axis along which the projection of molecular internal orbital angular momentum vanishes. 26
- 2.5 Schematic of the AMSF_{fm} ferromagnetic state. The thick arrow indicates the atomic condensate momentum \mathbf{Q} , lying in the plane transverse to the quantization axis $\hat{\ell}$, along which the projection of the molecular internal orbital angular momentum is $\ell_z = +1$ 27
- 2.6 Mean-field phase diagram of a p -wave resonant two-component Bose gas for large positive detuning. Molecules are gapped, reducing the system to a conventional two-component Bose gas, for $\lambda_1\lambda_2 > \lambda_{12}^2$ displaying three types of ASF phases. . . . 31

| | | |
|------|--|----|
| 2.7 | Schematic atomic (thick) and molecular (thin) order parameters versus the FR detuning ν for the polar phase, with $\nu_{c1} = \nu_c^{\text{MSF}_p\text{-AMSF}_p}$ and $\nu_{c2} = \nu_c^{\text{AMSF}_p\text{-ASF}}$ | 37 |
| 2.8 | Mean field phase diagrams for polar phase as a function of atomic and molecular chemical potentials, μ_a , μ_m , respectively. Ferromagnetic phase is similar but with different parameters. (a) For $\lambda(g_1 + g_2) - \tilde{g}_{am}^2 > 0$, all three superfluid phases, ASF, AMSF, and MSF appear and are separated by continuous phase transitions (thick black lines), (b) For $\lambda(g_1 + g_2) - \tilde{g}_{am}^2 < 0$, AMSF is unstable, and the ASF and MSF are separated by a first-order transition (hatched double line). | 38 |
| 2.9 | Schematic atomic (thick) and molecular (thin and dashed) order parameters versus the FR detuning ν for ferromagnetic phases. The $\text{AMSF}_{\text{fm}}\text{-AMSF}_p$ phase transition at ν_{c2} leads to kinks (change in slope) in the molecular (u) and atomic (Ψ) order parameter, later indicated by a black dot. Without loss of generality we chose \hat{n} axis (component of u) to lie along \mathbf{Q}_0 . The critical detunings are denoted by $\nu_{c1} = \nu_c^{\text{MSF}_{\text{fm}}\text{-AMSF}_{\text{fm}}}$, $\nu_{c2} = \nu_c^{\text{AMSF}_{\text{fm}}\text{-AMSF}_p}$, and $\nu_{c3} = \nu_c^{\text{AMSF}_p\text{-ASF}}$ | 39 |
| 2.10 | Schematic detuning dependence of the momentum \mathbf{Q}_0 of the atomic condensate starting with the ferromagnetic MSF_{fm} , with $\nu_{c1} = \nu_c^{\text{MSF}_{\text{fm}}\text{-AMSF}_{\text{fm}}}$, $\nu_{c2} = \nu_c^{\text{AMSF}_{\text{fm}}\text{-AMSF}_p}$, and $\nu_{c3} = \nu_c^{\text{AMSF}_p\text{-ASF}}$ | 40 |
| 2.11 | A lowest-order diagrammatic correction to molecular interaction coupling g_i | 41 |
| 2.12 | A next lowest-order diagrammatic corrections to molecular interaction couplings g_i | 41 |
| 2.13 | Schematic ASF single BEC (ASF_σ) excitation spectrum. The lowest curve is the atomic Bogoliubov mode and the upper curves are gapped atomic (thin) and molecular (thick) modes. | 45 |
| 2.14 | Schematic ASF double BEC (ASF_{12}) excitation spectrum. There are two gapless atomic Bogoliubov modes (thin) as well as three gapped molecular modes (thick). . . . | 47 |

- 2.15 Schematic excitation spectrum for the polar molecular superfluid, MSF_p . The doubly-degenerate atomic spectrum (upper thin curve) exhibits a minimum gap at nonzero k , a precursor of finite momentum atomic condensation inside the AMSF_p . The molecular spectra (thick curves), one longitudinal (lowest) and two degenerate transverse (middle) modes are of Bogoliubov type. 49
- 2.16 Schematic Excitation spectrum for the ferromagnetic molecular superfluid, MSF_{fm} . The doubly-degenerate atomic spectrum (thin curves) exhibits a minimum gap at nonzero k , a precursor of finite momentum atomic condensation. The molecular spectrum (thick curves), consists of a longitudinal gapless quadratic ferromagnetic spin-wave mode (lowest), a Bogoliubov sound mode and a quadratic gapped mode. 51
- 2.17 The diagram defining various vectors appearing in Eq. (2.169). $\vec{V} = \hat{n} \cos(\varphi - 2\theta_+) - \hat{m} \sin(\varphi - 2\theta_+)$, while $\varphi - 2\theta_+$ is measured relative to \hat{n} axis and φ_0 is measured relative to \hat{z} 56
- 2.18 (a) 2π “spin” vortex with equal counter-propagating atomic currents, $\mathbf{j}_1, \mathbf{j}_2$. (b) 2π “charge” vortex with equal co-propagating currents, confined to a domain wall (grey area), of width $\xi \sim 1/Q$, with atomic order parameter suppressed. In the presence of a molecular 4π -vortex domain wall is no longer required, and the “charge” vortex is deconfined. 67
- 2.19 $\pi - \pi$ vortex in $\alpha = 0$ limit. (a) In $\theta_1 - \theta_2$ representation; black (grey) arrows indicate θ_1 (θ_2). (b) In $\theta_+ - \theta_-$ representation, the pair of arrows indicate θ_+ and θ_- , while wavy line indicates a domain wall. For $\alpha \neq 0$, the Feshbach resonance coupling “squeezes” the θ_+ π -vortex textures into a domain wall of width $\xi \sim 1/Q$. In the presence of an additional molecular 2π vortex, the domain wall is absent and the composite defect is deconfined. 68
- 2.20 N, ν, T dependent cuts through the bulk phase diagram with increasing radial position r through the atomic cloud. Stars indicate system’s parameters (local chemical potentials μ_a, μ_m) at the trap center. 69

| | | |
|------|---|----|
| 2.21 | Schematic illustration of the shell structure expected in the p -wave resonant atomic cloud, corresponding to the phase diagram cuts in Fig. 2.20. | 71 |
| 3.1 | The schematic global phase diagram of Fe_{1+y}Te in T and y (doping) space. | 75 |
| 3.2 | Left : Bi-collinear state with spins locked by the single-ion anisotropy to the xy -plane along the b -axis, and exchange couplings of the model Eq. (3.5) indicated; Upper right : the electron configuration of Fe^{2+} in the orthorhombic phase; Lower right : the choice of coordinates. | 78 |
| 3.3 | Phase diagram of our microscopic Hamiltonian. Solid lines are phase boundary determined by comparing the classical energies. | 80 |
| 3.4 | The spin wave dispersion of the incommensurate spin spiral state for $J_{2a} = J_{2b} = 1$, $J_1 = 0.4$, $A_a = 0.1$, $A_b = 0.12$. Upper : the dispersion along (k, k) . Lower : the dispersion along $(k, -k)$ | 82 |
| 3.5 | The spin wave dispersion of the bi-collinear spin state for $J_{2a} = J_{2b} = 1$, $J_1 = 0.4$, $A_a = 0.1$, $A_b = 0.3$. Upper : the dispersion along (k, k) . Lower : the dispersion along $(-k, k)$ | 83 |
| 3.6 | The global phase diagram in the reduced exchange, r and bulk modulus B plane. For low Fe doping, experiments [45, 46, 139] suggest that the reducing temperature takes the system across the first-order phase boundary in the positive $r-B$ quadrant, leading to a simultaneous orthorhombic distortion and development of bi-collinear magnetic order. | 90 |
| 3.7 | Energy ($E(k)$) as a function of momentum Q in commensurate-incommensurate transition in φ representation of Eq. (3.61). Q_c represents the CI transition point. | 93 |
| 3.8 | $\theta(x)$ (Elliptic integral of the second kind) displaying a train of domain walls in the incommensurate state, just above Q_c , as well as the average tilted form $\bar{\theta}(x) = qx$ | 95 |
| 3.9 | A train of domain walls in the incommensurate state, $\delta\theta = \theta(x) - \bar{\theta}(x)$, just above Q_c , after $\bar{\theta}(x) = qx$ has been subtracted. | 96 |

| | | |
|------|---|-----|
| 3.10 | The spectra showing two shifted parabolas hybridized weakly (in proportion to D_{ab}) at their crossings. | 99 |
| 3.11 | The static structure function where the shift of peaks from incommensurate wavevector q_1 (red line) to commensurate wavevector $q_0/2$ (blue line) are shown. The dashed lines are the value in between. The plot is drawn in arbitrary unit. | 100 |
| 3.12 | The dynamic structure function in function of k (top) and ω (bottom). We can see the shift of peaks from the incommensurate state (red) where D_{ab} is small to commensurate state (blue) where D_{ab} is large. The dashed lines are the value in between. The lorentzian peak at $\omega = 0$ represents the relaxational dynamics which is the main feature of disordered phase. | 102 |
| 3.13 | The dynamic structure function in disordered phase above the commensurate state in k and ω space. | 104 |

Chapter 1

Introduction

1.1 Overall Background

One of the fundamental questions in condensed matter physics is classification and characterization of different phases of matter. In many cases, the low temperature regime and small energy scales are at the central focus of these studies since much of interesting physics like superfluidity, superconductivity, and magnetism appear in these conditions. It is therefore quite uncommon and exotic for a system to exhibit low temperature phases characterized by a finite momentum where nonzero kinetic energy plays a crucial role. Indeed the success of the fundamental theories of superfluidity and superconductivity relies heavily on their simple ground state structure. However, in the recent decades a number of systems have been discovered or theoretically proposed to exhibit ground states with finite momentum. In fact, many exotic physical phenomena are closely related with finite momentum phases. One of the most familiar and oldest examples are density wave states such as charge-density wave (CDW) and spin-density wave (SDW) that play an important role in modern condensed matter physics.

Since the pioneering work by Peierls in 1930s [1], the density waves have attracted a lot of interest [2, 3]. CDW and SDW appear materials and have been argued to play a central role to understanding of the high T_c superconductors [4, 5] where the pairing mechanism and pseudo-gap states are still not understood and are hotly debated. More recently, it is discovered that iron-based materials also show superconductivity at higher transition temperature [6, 7] and as a result have attracted considerable attention in the condensed matter community. For iron based

superconductors, it is also believed that density waves (especially SDW) play a similarly important role.

In the area of exotic superconductivity, Fulde-Ferrel-Larkin-Ovchinnikov (FFLO) state is another famous and long-sought-after finite momentum superconducting ground state [8, 9]. It is expected to be driven by a high Zeeman field, that leads to partial polarization of the Fermi sea. The corresponding spin-up and spin-down Fermi surfaces mismatch determines the finite momentum of the modulated ground state. Despite many efforts for an experimental realization of the FFLO state, because of many complexities of traditional solid state systems, there is little direct evidence for a realization of this fascinating state. However, some prospects have recently appeared in degenerate atomic gases, that offer a number of advantages over their solid-state cousins.

Such states are of considerable interest because in addition to internal symmetry breaking (be it superfluidity, superconductivity, magnetism, etc), they also spontaneously break spatial symmetries, which leads to interesting interplay of Goldstone modes and topological defects. In this thesis, we investigate two novel putative realizations of such finite momentum states in the context of degenerate atomic gases and the other in antiferromagnetic parent compound of iron-based superconductors, that have received considerable attention recently. A unifying theme of these physically quite distinct systems is the finite momentum (i.e., periodically modulated) superfluid and magnetic orders, respectively. Before turning to details, we next briefly outline each system.

1.2 Degenerate atomic gases

The development of the laser cooling and trapping of neutral atoms has led to tremendous progress and milestones in the newly burgeoning field of condensed matter of degenerate atomic gases. Because trapped atomic gases are extremely dilute, studies of condensed matter phenomena in such systems seems at first sight quite paradoxical. However, magically the interplay of their quantum degeneracy and strong interactions enables rich phenomenology even in these extremely dilute regimes.

The necessary strong interactions in these gaseous systems have primarily been realized in

two independent ways. One powerful method (that we mention for completeness but is not the subject of this thesis) is through the introduction on an optical lattice, generated via an AC Stark effect of crossed detuned laser beams generating a periodic standing wave. By suppressing atomic motion, the generated periodic potential strongly quenches the kinetic energy, thereby enhancing the dimensionless measure of the interaction relative to kinetic energy. This highly tunable (in terms of geometry and strength of the periodic potential) technique has lead to a realization of large number of phenomena, the earliest and best studied of these, the superfluid-insulator transition in bosonic atoms [10, 11, 12]. Optical lattices thereby give considerable promise for engineering a broad range of quantum many-body lattice models experimentally and exploring their exotic phenomenology.

A second methods of generating strong interactions (that is central to the first part of this thesis) is through the so-called Feshbach resonances [13]. These have been first demonstrated experimentally in [14] and have become a standard and highly tunable tool of controlling interactions in fermionic and bosonic atomic gases. This tunable interaction phenomenon is associated to the existence of two-body resonant scattering, that appears when a quasi-bound state of two atoms in a non-scattering internal state (the so-called closed channel) is tuned to cross and thereby strongly affect the low-energy continuum of atomic scattering (the so-called open channel) states. The two channels are distinguished by the two-atom electron spins, with the open channel an approximate spin-triplet and closed channel an approximate singlet. Consequently they have different Zeeman energies, allowing the center of mass rest energy ν of closed channel bound state to be tuned, relative to the open channel two-atom continuum, via an external magnetic field. This yields an unprecedented tunability of the effective atomic interaction strength by varying a magnetic field. For fermionic trapped gases, it enabled a realization of a fermionic atom-paired s -wave superfluidity and exploration of its BEC-BCS crossover and resonant universality [15, 16, 17, 18, 19, 20, 21, 22, 23, 24, 25, 26, 27, 28, 29, 30, 31, 32, 33].

These and many other studies have thereby raised a question of the analog of such BCS-BEC crossover for resonant bosonic atoms. For bosonic, single species s -wave FR this question has been extensively explored and answered, starting with the early work of Radzihovsky *et al.* and Romans

et al. [34, 35, 36, 37, 38]. These works find that in contrast to smooth evolution for fermionic gases, bosons necessarily exhibit a phase transition between an atomic (ASF) and molecular (MSF) forms of superfluidity of such a resonant gas.

A natural extension of such resonant system to a far richer p -wave bosonic resonant gas, which is motivated by p -wave resonance in mixtures of ^{85}Rb - ^{87}Rb gases [39], and richness of p -wave superfluidity in fermionic systems is the subject of this thesis. As we will show, out of wealth of interesting phenomena that such system exhibits, the most interesting one is a robust realization of a finite-momentum superfluid at intermediate detunings.

We present the more detailed motivation in Sec. 1.4.

1.3 Iron-based superconductors and antiferromagnets

The other major subject of this thesis is the physics of iron telluride (FeTe), one of the parent materials of the iron-based superconductor. Iron-based superconductor received huge attention recently and there have been tremendous research activities already. While the subject is quite different from ultracold atomic gases, still there is an interesting and important physics behind FeTe related with finite momentum phases, in particular, SDW.

Traditionally, iron or other magnetic elements are considered to be a bad candidate for a superconducting material since the magnetism (e.g. ferromagnetism) disfavors superconductivity (e.g. seen from the Meissner effect). Therefore it was quite a surprise when Hosono and coworkers discovered a superconductivity [6] from LaFeAsO. Since then, many iron based superconductors discovered and typically classified as 1111 material (e.g. LaFeAsO), 122 material (e.g. BaFe₂As₂), and etc depending on their structures [7].

Even though there are many different iron-based superconductors, they share interesting features which make them distinct from cuprate superconductors. First of all, the phase diagram is very similar to that of cuprates while the mechanism and pairing symmetry are believed to be different [7]. As in the case of cuprates, the phase diagram is consist of antiferromagnetic order and superconducting dome where both can be controlled by the doping of chemical substitutions. The

similarity of phase diagram implies that the pairing mechanism is believed to be unconventional, i.e. non-phonon mediated, but might be different from cuprates. Another distinct feature of iron-based superconductors is their pairing symmetry. Unlike from the cuprates which show d -wave symmetry, (unconventional) s -wave symmetry is predicted and observed in iron-based superconductors [40, 41, 42]. However the node and the sign-changing order parameter are found in most of the compounds which makes it distinct from conventional BCS superconductors. The gap structure is believed to be s_{\pm} or s_{++} which is still on active research. Finally the parent compounds of iron-based superconductors are mostly metallic while most cuprates are based on the Mott-insulators. Due to the metallic nature of compounds, the Fermi surface nesting is expected and observed in many cases which leads the discussion about the effects of nesting. Actually it is widely accepted that the nesting and density wave order will be the key to explain the superconducting mechanism in iron based superconductor.

More recently the materials with simpler structure draw attentions from researchers. In particular, FeTe and FeSe attracted considerable interest due to their structural simplicity and are expected to simplify the deciphering of superconductivity mechanism the superconducting mechanism directly.

In this thesis, we study self-doped Fe_{1+y}Te focusing on its magnetic structure and dynamic properties. Even though Fe_{1+y}Te is not a superconducting material itself (doping of Se or S is needed for superconductivity), it exhibits interesting physics such as commensurate-incommensurate transition. We will describe more detailed motivation of Fe_{1+y}Te in Sec. 1.4.

1.4 Theoretical and experimental motivation

The main goal of this thesis is to explore the physics of the finite momentum ground states, focusing on two specific experimental realizations. In particular, we investigate the system of degenerate gases and iron based material based on following theoretical and experimental motivations.

First we study the finite momentum state in the degenerate bosonic gases with p -wave Feshbach interaction. There has been an earlier work by Radzihovsky *et al.* on bosonic system with

s -wave interaction [34, 35, 36], followed by a number of interesting generalization to lattice systems and recent numerical studies [37, 38]. Unlike the fermionic BEC-BCS crossover where the order parameter structure remains the same throughout the phase diagram, they found a true phase transition between atomic superfluid (ASF corresponds to BCS) and molecular superfluid (MSF corresponds to BEC). Therefore extending this study to a finite angular momentum symmetry of the interaction, (e.g. p -wave) is one of the main motivation of our work.

In addition to the theoretical motivation, there are few experiments that observed p -wave FR in ultracold atoms [43, 44]. First, Gaebler *et al.* observed the p -wave FR from ^{40}K [44]. Using fermionic atoms, they were able to make the cold molecular gas and found that it exhibits the angular momentum structure of p -wave interaction. p -wave FR was also found in bosonic atoms. Papp *et al.* first observed p -wave FR in bosonic atoms between ^{87}Rb and ^{85}Rb isotopes [39]. We note that two different bosonic species are needed to have p -wave interaction due to bosonic symmetry. Similar to the fermionic counterpart, these rubidium gases has been confirmed to display the p -wave two-body scattering properties. Unfortunately both realizations are unstable due to three-body processes, thereby creating considerable challenges for reaching to the degenerate regime where interesting quantum many body effects are realized. We hope that these challenges can be overcome (e.g., via stabilization in an optical lattice [37, 38]), allowing predictions in this thesis to be testable.

While finishing our study on bosonic p -wave FR interaction, we learned of an interesting inelastic neutron scattering experiments on FeTe conducted by Reznik group and turned our attention to Fe_{1+y}Te which was found to exhibit several novel characteristics.

The most interesting of these is an unconventional bi-collinear planar magnetic state, with a commensurate, planar spin-spiral order characterized by $(\pi/2, \pi/2)$ wavevector in the orthorhombic ab -plane [45]. A magnetic transition to this state is accompanied by a structural transition to an orthorhombic (with slight monoclinicity) state [46]. At low temperature, the magnetic order also undergoes a commensurate-incommensurate (CI) transition with iron doping at $y_c = 0.12$. Low doping ($y < 0.12$) corresponds to the bi-collinear commensurate state while spin-spiral (incommen-

surate phase) state are observed at large doping ($y > 0.12$).

Furthermore, even though Fe_{1+y}Te is metallic, several experiments support the local magnetic moment picture for Fe_{1+y}Te . It is found that Fe_{1+y} follows Curie-Weiss law with a relatively large magnetic moment [46]. Also nesting along the magnetic ordering wavevector is not observed from DFT calculation and ARPES experiment [47, 48]. There have been several analytical and numerical studies to explain the observed phenomenology of FeTe [49, 50, 51, 52, 53]. Although these models were successful in describing the observed bi-collinear and spin-spiral order, because of the underlying spin-rotational invariance of these models, they predict these magnetically ordered states to exhibit gapless spectra. This contrasts the gapped excitation spectrum observed in the commensurate bi-collinear state.

In addition, the aforementioned recent paper by Parshall *et al.* added a new interesting phenomenology to be explained and was the main motivation for our work. At low temperature below T_N , they observed a commensurate Bragg peak corresponding to the previously established bi-collinear order at $q_0 = [1/2, 0, 1/2]$. However, below above T_N their inelastic neutron scattering measurements showed that the dynamic structure peak shifts to an incommensurate wavevector $q_1 = [0.45, 0, 0.5]$.

In the second part of this thesis, we present a model that is a qualitative extension of the earlier model by Turner *et al.* [49]. By introducing a single ion anisotropy derivable from the magnetoelastic coupling, we are able to describe much of the above phenomenology of Fe_{1+y}Te , from the gap structure of the excitation spectrum to the commensurate-incommensurate transition. We present the details in Chapter 3.

1.5 Outline of the thesis

The remainder of this thesis is organized as follows.

In Chapter 2, we present the study on the bosonic dilute gas with p -wave Feshbach interaction. We start from more detailed background and set up our model. Then we give the global phase diagram based on the mean-field theory followed by the analysis on the excitations and topological

defects.

The study on the static and dynamic properties of FeTe is given in Chapter 3. After presenting our model, we analyze the magneto-structural transition of FeTe. Then the commensurate-incommensurate transition is studied in the context of Pokrovsky-Talapov theory. We present the magnetic dynamic properties of FeTe and calculate the dynamic structure factor throughout the phase diagram. We show that they are consistent with the experiment.

In Chapter 4, we conclude with future directions and a summary of the thesis.

Chapter 2

p-wave resonant Bose gas

2.1 Introduction

2.1.1 Background and Motivation

Since the experimental realization of Bose-Einstein condensation (BEC) in trapped alkali atomic gases [54, 55], the resulting burgeoning field of degenerate atomic gases has seen an ever-expanding research activity. It has been fueled by the steady advances in new experimental techniques to control and interrogate the continually growing class of degenerate atomic systems. A Feshbach resonance (FR) has been one of these exceptionally fruitful experimental “knobs”, that lends exquisite tunability (via magnetic field) of interactions in the ultra-cold atomic gases. For fermionic trapped gases, it enabled a realization of a fermionic atom-paired *s*-wave superfluidity and exploration of its BEC-BCS crossover and resonant universality [15, 16, 17, 18, 19, 20, 21, 22, 23, 24, 25, 26, 27, 28, 29, 30, 31, 32, 33].

Motivated by the demonstration of *p*-wave FR in ^{40}K and ^6Li , *p*-wave paired fermionic superfluidity has also been extensively explored theoretically [56, 57, 33, 58], predicting to exhibit an even richer phenomenology. A recent laboratory production of *p*-wave Feshbach molecules [44, 59] shows considerable promise toward a realization of *p*-wave fermion-paired superfluidity and the associated rich phenomenology [33], though substantial challenges of stability remain [44, 60].

The bosonic counterparts have also been extensively explored and in fact in the *s*-wave FR case of ^{85}Rb [61] predate recent fermionic developments. As was recently emphasized [34, 35,

36], in contrast to their fermionic analogs, that undergo a smooth BEC-BCS crossover, resonant **bosonic** gases are predicted to exhibit magnetic field- and/or temperature-driven sharp phase transitions between distinct molecular and atomic superfluid phases. One serious impediment to a laboratory realization of this rich physics is the predicted [62, 63] and observed [64] instabilities of a resonantly attractive Bose gas sufficiently close to a Feshbach resonance. Nevertheless, a number of features of the phase diagram are expected to be exhibited away from the resonance and/or reflected in the nonequilibrium phenomenology (before the onset of the instability) of a resonant Bose gas. Furthermore, recent extension to an s -wave resonant Bose gas in an optical lattice [37, 38] demonstrated the stabilization through a quantum Zeno mechanism proposed by Rempe [65], that dates back to Bethe's [66] analysis of the triplet linewidth in hydrogen. The predictions [34, 35, 36, 37, 38] have been supported by recent density matrix renormalization group [67], exact diagonalization [68], and quantum Monte Carlo [69] studies, as well extensions to two species [68].

Along with the ubiquitous s -wave resonances, recent experiments on a ^{85}Rb - ^{87}Rb mixture have demonstrated an interspecies p -wave Feshbach resonance at $B = 257.8$ Gauss [39, 70]. Although the consequences of this two-body p -wave resonance on the degenerate many-body state of such a gas mixture has not been explored experimentally, it provided the main motivation for our recent [71] and present studies. We note that closely related studies of Bose condensation in p -(and higher) bands in optical lattices have been carried out in Refs. [72, 73, left=,right=].

The rest of the paper is organized as follows. We conclude the Introduction with a summary of our main results and their experimental implications. In Section 2.2 we introduce a microscopic two-channel p -wave FR model for a description of a two-component Bose gas, as for example realized by a ^{85}Rb - ^{87}Rb mixture. Having related the parameters of the model to two-body scattering experiments on a dilute gas, in Section 2.3 we present a general symmetry-based discussion of phases and associated phase transitions expected in such an atomic gas at finite density. In Section 2.4, by minimizing the corresponding imaginary-time coherent state action, we map out a generic mean-field phase diagram for this system. In Section 2.5, we supplement this Landau analysis with a derivation of the corresponding Goldstone mode Lagrangians and extract from them the low-energy

elementary excitations and dispersions characteristic of each phase. The true (beyond-mean-field) nature of the quantum and thermal phase transitions is discussed in Section 2.6. In Section 2.7 we study the topological defects, vortices and domain walls, in each of the phases. We make a more direct contact with cold-atoms experiments in Section 2.8 by using a local density approximation (LDA) to include the effects of the trapping potential. We close with a brief summary in Section 2.9.

2.1.2 Summary of results

Before turning to the analysis of the system, we present the main predictions of our work, a small subset of which was previously reported in a brief Letter [71]. Our key results are summarized by a Feshbach resonance detuning - temperature phase diagram, illustrated in Fig. 2.1, and by the properties of the corresponding phases and transitions.

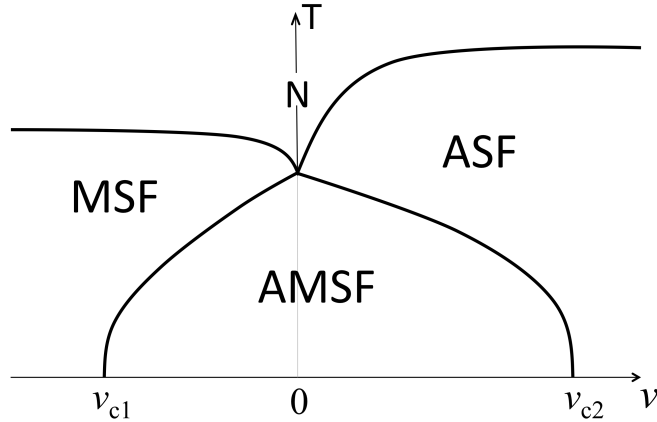


Figure 2.1: Schematic temperature-detuning phase diagram for a balanced two-species p -wave resonant Bose gas. As illustrated, it exhibits atomic (ASF), molecular (MSF), and atomic-molecular (AMSF) superfluid phases. The novel AMSF state is characterized by a p -wave, molecular and a finite-momentum Q (see Fig. 2.2) atomic superfluidity.

We find that in addition to the normal (i.e., non-superfluid) high temperature phase, the p -wave Feshbach-resonant two-component **balanced** Bose gas (e.g., equal mixture of ^{85}Rb and ^{87}Rb atoms) generically exhibits three classes of superfluid phases: atomic (ASF), molecular (MSF) and atomic-molecular (AMSF) condensates, where atoms, p -wave molecules, and both are Bose-

condensed, respectively. Our most interesting finding is that the AMSF phase, sandwiched between (large positive detuning) ASF and (large negative detuning) MSF phases is necessarily a **finite momentum** Q spinor superfluid, akin to (but distinct from) a supersolid [74, 75, 76, 77, 78]. It is characterized by a momentum $\hbar Q$, with

$$Q = \alpha m \sqrt{n_m} \sim \sqrt{\gamma_p \ell n_m} \lesssim \sqrt{\gamma_p} / \ell, \quad (2.1)$$

tunable with a magnetic field (via FR detuning, ν that primarily enters through the molecular condensate density $n_m(\nu)$), with α , m , ℓ , and γ_p , respectively, the FR coupling, atomic mass, average atom spacing, and a dimensionless measure of FR width [33].

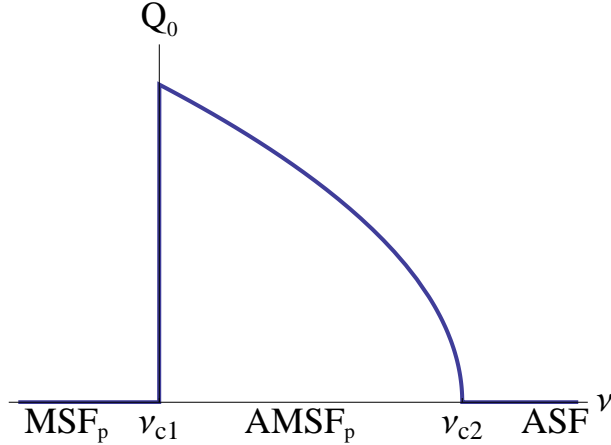


Figure 2.2: Schematic momentum $Q(\nu)$ characteristic of the AMSF (polar) state, ranging between zero and the p -wave FR width-dependent value.

As illustrated in the phase diagram, Fig. 2.1, the ASF appears at a large positive detuning (weak FR attraction) and low temperature, where one of the three combinations (ASF₁, ASF₂, ASF₁₂) of the ⁸⁵Rb and ⁸⁷Rb atoms are Bose-condensed into a conventional, uniform superfluid, and the p -wave ⁸⁵Rb-⁸⁷Rb molecules are energetically costly and therefore appear only as gapped excitations.

In the complementary regime of a large negative detuning, the attraction between two flavors of atoms is sufficiently strong so as to bind them into a tight p -wave hetero-molecules (e.g., ⁸⁵Rb-⁸⁷Rb molecule), which at low temperature condense into a p -wave superfluid, with atoms in the

species-balanced case existing only as gapped excitations. In this tight binding molecular regime the gas reduces to a well-explored system of a spinor-1 condensate [79, 80, 81, 82, 83, 84, 85, 86, 87, 88, 89, 90, 91, 92, 93, 94, 95, 96], with the spinor corresponding to the relative orbital angular momentum $\ell = 1$ of the two constituent atoms of the p -wave molecule. Thus, for negative detuning we predict the existence of a $\ell_z = 0$ “polar” (MSF_p) and $\ell_z = \pm 1$ “ferromagnetic” (MSF_{fm}) molecular p -wave superfluid phases, with their relative stability determined by the ratio a_0/a_2 of molecular spin-0 (a_0) to molecular spin-2 (a_2) scattering lengths. We find that this ratio and therefore the first-order MSF_p - MSF_{fm} transition are in turn controlled with the p -wave Feshbach resonance detuning ν , or equivalently, the atomic p -wave scattering volume $v \sim 1/\nu$, tunable with a magnetic field.

We emphasize that (in contrast to the s -wave case [34, 35, 36]) because a p -wave resonance does not couple a **uniform** atomic condensate to the molecular one, a p -wave molecular condensate is **not** automatically induced inside the ASF state.

The most distinctive signatures of these superfluids should be directly detectable via time-of-flight shadow images, with the ASF exhibiting an atomic condensate peak and MSF displaying a p -wave molecular one. At higher densities in a trap, the bulk phase diagram as a function of the chemical potential (see Fig. 2.20 and 2.21) translates into shell structure of distinct phases, that we estimated within the local density approximation (LDA) [97, 98, 99].

In addition to these fairly conventional **uniform** atomic and molecular BEC’s, for intermedi-

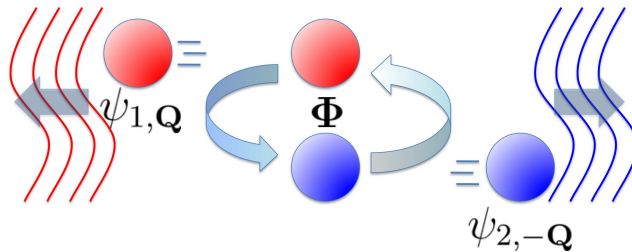


Figure 2.3: A cartoon of a p -wave molecule decaying into two oppositely moving two species of atoms, illustrating a resonant mechanism for a finite momentum \mathbf{Q} atomic superfluidity (indicated by wavy lines) in the AMSF phase.

ate detuning around unitary point we predict the existence of novel AMSF_p and AMSF_{fm} phases, characterized by a **finite** momentum Q atomic condensate [72, 71], that is a superposition of the two atomic species. Such, generically supersolid state [74, 75, 76, 77, 78] is always accompanied by a p -wave molecular condensate, concomitantly induced through the p -wave FR interaction. In addition to exhibiting an off-diagonal long-range order (ODLRO) of an ordinary superfluid the two $\text{AMSF}_{p,\text{fm}}$ states (distinguished by the polar versus ferromagnetic nature of their p -wave molecular condensates) spontaneously partially break orientational and translational symmetries, akin to polar and smectic liquid crystals [100] and the putative Fulde-Ferrell-Larkin-Ovchinnikov states of imbalanced paired fermions [8, 9, 101, 102, 103, 104, 105, 106].

As illustrated in Fig. 2.4, in the polar AMSF_p state, \mathbf{Q} aligns along the quantization axis along which the molecular condensate has a zero projection of its internal $\ell = 1$ angular momentum. For the case of the ferromagnetic AMSF_{fm} state, \mathbf{Q} lies in the otherwise isotropic plane, transverse to the p -wave molecular condensate axis, as illustrated in Fig. 2.5.

In the narrow FR approximation we find that the $\text{AMSF}_{p,\text{fm}}$ states are collinear, characterized by a single \mathbf{Q} of a Fulde-Ferrell like form [8], as opposed to a $+\mathbf{Q}$ and $-\mathbf{Q}$ Larkin-Ovchinnikov like [9] or other more complicated crystalline forms, found in imbalanced paired fermionic systems [104, 105, 106]. However, because the detailed spatial structure of the AMSF_{fm} (but not the AMSF_p state) sensitively depends on the interactions (since it spontaneously breaks symmetry transverse to the $\ell_z = 1$ axis), we do not exclude a more general lattice structure in a more generic beyond-mean-field model, that is best analyzed numerically.

The phase boundaries between this rich variety of phases can be calculated for a narrow Feshbach resonance and in a dilute Bose gas limit, but are notoriously difficult to estimate in a strongly interacting system, where they can only be qualitatively estimated within a mean-field analysis. In the former case the zero-temperature phase boundaries are given by critical detunings:

$$\nu_c^{\text{MSF}_p-\text{AMSF}_p} = -(g_1 + g_2 - 2g_{am} + \frac{m\alpha^2}{\hbar^2})n_m, \quad (2.2)$$

$$\nu_c^{\text{AMSF}_p-\text{ASF}} = (2\lambda - g_{am} + \frac{m\alpha^2}{2\hbar^2})n_a, \quad \text{for } g_2 < 0, \quad (2.3)$$

with similar expressions for transitions out of the ferromagnetic phases, that can be found in Eq. (2.80), (2.81). Here g_i 's and λ_i 's are molecular and atomic two-body interaction pseudopotentials, respectively related to the background molecular (a_0^{bg} and a_2^{bg}), and atomic scattering lengths (a_{11}^{bg} , a_{22}^{bg} , and a_{12}^{bg}).

As any neutral superfluid, ASF, MSF, and AMSF are each characterized by Bogoliubov modes, illustrated in Fig. 2.13, 2.14, 2.15, and 2.16, with long wavelength acoustic “sound” dispersions

$$E_\sigma^B(\mathbf{k}) \approx c_\sigma \hbar k, \quad (2.4)$$

where c_σ (with $\sigma = \text{ASF}_{1,2,12}$, $\text{MSF}_{\text{p,fm}}$, $\text{AMSF}_{\text{p,fm}}$) are the associated sound speeds with standard Bogoliubov form $c_\sigma \approx \sqrt{g_\sigma n_\sigma / 2m}$. In each of these SF states one Bogoliubov mode (and only one in the ASF_i states) corresponds to the overall condensate phase fluctuations. In addition, the MSF_p exhibits two degenerate “transverse” Bogoliubov orientational acoustic modes. The MSF_{fm} is also additionally characterized by one “ferromagnetic” spin-wave mode, $E_k^{\text{MSF}_{\text{fm}}} \sim k^2$ and one gapped mode, consistent with the characteristics of a conventional spinor-1 condensate [84, 85].

Because $\text{MSF}_{\text{p,fm}}$ are paired molecular superfluids, they also exhibit gapped single atom-like quasiparticles (akin to Bogoliubov excitations in a fermionic paired BCS state), that do not carry a definite atom number. These single-particle excitations are “squeezed” by the presence of the molecular condensate, offering a mechanism to realize atomic squeezed states [107], that can be measured by interference experiments, similar to those reported in Ref. [108, left=,right=]. The low-energy nature of these single-atom excitations is guaranteed by the vanishing of the gap at the MSF-AMSF transition at $\nu_c^{\text{MSF}_{\text{p,fm}}-\text{AMSF}_{\text{p,fm}}}$, with $E_{\text{MSF}}^{\text{gap}}(\nu_c) = 0$.

We also note that inside the $\text{MSF}_{\text{p,fm}}$, for $\nu > \nu_*^{\text{p,fm}} = -(g_{\text{p,fm}} + C_{\text{p,fm}} m \alpha^2 / \hbar^2) n_m$, where $C_{\text{p,fm}} = 2, 1$ for polar and ferromagnetic phases, respectively, the minimum of the single-atom excitations (that for $\nu < \nu_*$ is at $k = 0$) shifts to a finite momentum, $k \approx Q$. This is a precursor of the atomic gap-closing MSF-AMSF transition at $\nu_c^{\text{MSF}-\text{AMSF}}$, where atoms also Bose condense at finite momentum Q .

We predict that in addition to the conventional Bogoliubov superfluid mode associated with the phase common to the atomic and molecular condensates, the AMSF also exhibits a Goldstone mode corresponding to the fluctuation of a **relative** phase between the two atomic condensate components. Furthermore, a spatially periodic, collinear AMSF state, characterized by at least $\pm\mathbf{Q}$ momenta (but not just single \mathbf{Q}) further exhibits the condensate phonon mode u corresponding to the difference between phases of the $\pm\mathbf{Q}$ condensate components, akin to the Larkin-Ovchinnikov state [9, 109, 110].

For the single \mathbf{Q} AMSF states, we predict the smectic-like “phonon” spectra in the polar and ferromagnetic cases

$$\omega_{\text{AMSF}_p}(\mathbf{k}) = \sqrt{(Bk_z^2 + Kk_\perp^4)/\chi_-}, \quad (2.5)$$

$$\omega_{\text{AMSF}_{\text{fm}}}(\mathbf{k}) = \sqrt{(Bk_z^2 + k^2(K_x k_x^2 + K_y k_y^2))/\chi_-}, \quad (2.6)$$

as well as the conventional Bogoliubov modes associated with superfluid order, and an orientational mode $\omega_{\text{fm}}^\gamma$, associated with orientational symmetry breaking in AMSF_{fm}

$$\omega_{+p}(\mathbf{k}) = \sqrt{\frac{2\rho_s}{\chi_+ m} k}, \quad (2.7)$$

$$\omega_{\text{fm}}^\gamma(\mathbf{k}) = \sqrt{\frac{Jk^2 [Bk_z^2 + k^2(K_x k_x^2 + K_y k_y^2)]}{J\chi_- k^2 + \kappa^2 k_y^2}}, \quad (2.8)$$

where $B = \frac{2\hbar^2 n_a}{m}$, $K = K_x = 2K_y = \frac{\hbar^6}{2m^3 \alpha^2}$, $J = \frac{\hbar^2 n_m}{4m}$, $\kappa = \frac{\hbar^2 \sqrt{n_m}}{\alpha m}$, and $\chi_-^{-1} = \frac{1}{2}(\lambda - \lambda_{12})$.

Having summarized the results of our study, we next turn to the definition of the two-component p -wave resonant Bose gas model, followed by its detailed analysis.

2.2 Model

We study a gas mixture of two distinguishable bosonic atoms (e.g., ^{85}Rb , ^{87}Rb) [70], created by field operators $\psi_\sigma^\dagger(\mathbf{r}) = (\psi_1^\dagger(\mathbf{r}), \psi_2^\dagger(\mathbf{r}))$, and interacting through a p -wave Feshbach resonance associated with a tunable “closed”-channel bound state. The corresponding p -wave ($\ell = 1$) closed-channel hetero-molecule (e.g., ^{85}Rb - ^{87}Rb) is created by a Cartesian vector field operator $\phi^\dagger(\mathbf{r}) = (\phi_x^\dagger, \phi_y^\dagger, \phi_z^\dagger)$, related to $\phi_\pm^\dagger = (\phi_x^\dagger \pm i\phi_y^\dagger)/\sqrt{2}$, $\phi_z^\dagger = \phi_z^\dagger$ operators, that create closed-channel

molecules in the $\ell_z = \pm 1, 0$ eigenstates, respectively. This system is governed by a grand-canonical Hamiltonian density (with $\hbar = 1$ throughout)

$$\begin{aligned} \mathcal{H} = & \sum_{\sigma=1,2} \hat{\psi}_\sigma^\dagger \hat{\varepsilon}_\sigma \hat{\psi}_\sigma + \hat{\phi}^\dagger \cdot \hat{\omega} \cdot \hat{\phi} + \mathcal{H}_{bg} \\ & + \frac{\alpha}{2} \left(\hat{\phi}^\dagger \cdot \left[\hat{\psi}_1(-i\nabla) \hat{\psi}_2 - \hat{\psi}_2(-i\nabla) \hat{\psi}_1 \right] + h.c. \right), \end{aligned} \quad (2.9)$$

where single particle atomic and molecular Hamiltonians are given by

$$\hat{\varepsilon}_\sigma = -\frac{1}{2m} \nabla^2 - \mu_\sigma, \quad (2.10)$$

$$\hat{\omega} = -\frac{1}{4m} \nabla^2 - \mu_m, \quad (2.11)$$

with the effective molecular chemical potential

$$\mu_m = \mu_1 + \mu_2 - \nu, \quad (2.12)$$

adjustable by a magnetic field dependent detuning ν , latter being the rest energy of the closed-channel molecule relative to a pair of open-channel atoms. For simplicity we have taken atomic masses to be identical (a good approximation for the ^{85}Rb - ^{87}Rb mixture that we have in mind), and will focus on the balanced case of $\mu_1 = \mu_2 = \mu$, with μ fixing the total number of ^{85}Rb and ^{87}Rb atoms, whether in the (open-channel) atomic or (closed-channel) molecular form. The FR interaction encodes a coherent interconversion between a pair of open-channel atoms 1, 2 (in a singlet combination of 1, 2 labels, as required by bosonic statistics) and a closed channel p -wave molecule, with amplitude α [111].

The FR coupling α and detuning ν are fixed experimentally through measurements of the low-energy two-atom p -wave scattering amplitude [43, 44]

$$f_p(k) = \frac{k^2}{-v^{-1} + \frac{1}{2}k_0 k^2 - ik^3} \quad (2.13)$$

where v is the scattering volume (tunable via magnetic field dependent detuning ν) and k_0 (negative for the FR case) is the characteristic wavevector, [112, 33]

$$v^{-1} = -\frac{6\pi}{m\alpha^2}(\nu - c_1), \quad (2.14)$$

$$k_0 = -\frac{12\pi}{m^2\alpha^2}(1 + c_2), \quad (2.15)$$

respectively analogous to the scattering length a and the effective range r_0 in s -wave scattering case. In above, constants $c_{1,2}$ are determined by the details of the p -wave interaction at short-scales, that in a pseudo-potential model above are given by [33]

$$c_1 = \frac{m\alpha^2}{9\pi^2}\Lambda^3, \quad (2.16)$$

$$c_2 = \frac{m^2\alpha^2}{3\pi^2}\Lambda, \quad (2.17)$$

where $\Lambda = 2\pi/d$ is the inverse size of the closed-channel molecular bound state, of order of the interatomic potential range.

The p -wave resonance and bound state energy are determined by the poles of $f_p(k)$. At low energies, (where ik^3 can be neglected) the energy of the pole is given by

$$E_p = \frac{k_p^2}{2m} \approx -\frac{1}{mv|k_0|}, \quad (2.18)$$

which is real and negative and thus is a bound state energy for $v > 0$ (negative detuning) and a finite lifetime resonance for $v < 0$ (positive detuning).

In above, for simplicity we have focused on a rotationally invariant FR interaction, with $\hat{\omega}$ and α independent of the molecular component i . This is an approximation for our system of interest, ^{85}Rb - ^{87}Rb mixture, where indeed the p -wave FR around $B = 257.8$ Gauss [39, 70] is split into a doublet by approximately $\Delta B = 0.6$ Gauss, similar to the fermionic case of ^{40}K [43, 44, 57, 33]. We leave the more realistic, richer case for future studies.

The background (non-resonant) interaction density

$$\mathcal{H}_{bg} = \mathcal{H}_a + \mathcal{H}_m + \mathcal{H}_{am} \quad (2.19)$$

is given by

$$\mathcal{H}_a = \sum_{\sigma=1,2} \frac{\lambda_\sigma}{2} \hat{\psi}_\sigma^\dagger \hat{\psi}_\sigma^2 + \lambda_{12} \hat{\psi}_1^\dagger \hat{\psi}_2^\dagger \hat{\psi}_2 \hat{\psi}_1, \quad (2.20)$$

$$\mathcal{H}_m = \frac{g_1}{2} (\hat{\phi}^\dagger \cdot \hat{\phi})^2 + \frac{g_2}{2} |\hat{\phi} \cdot \hat{\phi}|^2, \quad (2.21)$$

$$\mathcal{H}_{am} = \sum_{\sigma=1,2} g_{am} \hat{\psi}_\sigma^\dagger \hat{\phi}^\dagger \cdot \hat{\phi} \hat{\psi}_\sigma, \quad (2.22)$$

where coupling constants λ_σ , λ_{12} , $g_{1,2}$, g_{am} are related to the corresponding **background** s -wave scattering lengths (a_1 , a_2 , etc.) in a standard way, and thus are fixed experimentally through measurements on the gas in a dilute limit [15]. Correspondingly, we take these background s -wave couplings to be independent of the p -wave detuning, an approximation that we expect to be quantitatively valid in the narrow resonance and/or dilute limits considered here. A miscibility of a two-component atomic gas requires [113]

$$a_1 a_2 > a_{12}^2 \tag{2.23}$$

which may be problematic for the case of ^{85}Rb - ^{87}Rb due to the negative background scattering length of ^{85}Rb .

The molecular interaction couplings g_1 , g_2 (set by the $L = 0$ and $L = 2$ channels of p -wave molecule-molecule scattering) and g_{am} can be derived from a combination of s -wave atom-atom (λ_σ) and p -wave FR (α) interactions. We present lowest order of this analysis in Sec.2.4.4.3, that shows that these parameters can in principle be tuned via a magnetic field through the p -wave FR detuning ν .

The above two-channel model, Eq. (2.9) faithfully captures the low-energy p -wave resonant and s -wave nonresonant scattering phenomenology of the ^{85}Rb - ^{87}Rb p -wave Feshbach-resonant mixture [70]. Its analysis at nonzero balanced atomic densities, that is our focus here, leads to the predictions summarized in the previous section.

2.2.0.1 Lattice model

As discussed in the Introduction, based on the experience for the s -wave case [34, 35, 36, 114], it is likely that a stable realization of above continuum p -wave resonant two-species bosonic model will require an introduction of an optical lattice [37, 38]. This leads to a two-component atomic Hubbard model, with standard tight-binding atomic and molecular lattice-hopping kinetic energies, density-density interactions and a lattice projection of the p -wave Feshbach resonant coupling that

in a single band Wannier basis is given by

$$\mathcal{H}_{\text{FR}_p}^{\text{lattice}} = \frac{\alpha}{2} \sum_{\mathbf{r}_i, \alpha} b_{\alpha \mathbf{r}_i}^\dagger (a_{1, \mathbf{r}_i} a_{2, \mathbf{r}_i - \boldsymbol{\delta}_\alpha} - a_{1, \mathbf{r}_i} a_{2, \mathbf{r}_i + \boldsymbol{\delta}_\alpha}) + h.c., \quad (2.24)$$

where, e.g., on a cubic lattice, $\boldsymbol{\delta}_\alpha$ are lattice vectors. A related finite angular-momentum FR lattice model was proposed and studied in an interesting paper by Kuklov [72], predicting a robust p -wave atomic condensate in an optical lattice. As usual[11], at low lattice filling this lattice model reproduces the phenomenology of the continuum model. As an additional qualitative feature, at commensurate lattice fillings we also expect it to admit a rich variety of zero-temperature Mott insulating phases and quantum phase transitions from them to the superfluid ground states exhibited by the continuum system studied here. We leave the detailed analysis of the lattice model to future studies.

2.2.0.2 Coherence-state formulation of thermodynamics

With the model defined by $\hat{\mathcal{H}}$, Eqs. (2.9), (2.19), and (2.2), the thermodynamics as a function of the chemical potential μ (or equivalently total atom density, n), detuning ν and temperature T can be worked out in a standard way by computing the partition function $Z = \text{Tr}[e^{-\beta \hat{H}}]$ ($\beta \equiv 1/k_B T$) and the corresponding free energy $F = -k_B T \ln Z$. The trace over quantum mechanical many-body states can be conveniently reformulated in terms of an imaginary-time ($\tau = it$) functional integral over coherent-state atomic, $\psi_\sigma(\tau, \mathbf{r})$ ($\sigma = 1, 2$) and molecular, $\phi(\tau, \mathbf{r})$ fields:

$$Z = \int D\psi_\sigma^* D\psi_\sigma D\phi^* D\phi e^{-S}, \quad (2.25)$$

where the imaginary-time action is given by [115]

$$S = \int_0^\beta d\tau \int d\mathbf{r} \left[\psi_\sigma^* \partial_\tau \psi_\sigma + \phi^* \cdot \partial_\tau \phi + \mathcal{H}(\psi_\sigma^*, \psi_\sigma, \phi^*, \phi) \right], \quad (2.26)$$

$$= \int_0^\beta d\tau \int d\mathbf{r} \mathcal{L}. \quad (2.27)$$

The Lagrangian density is given by

$$\begin{aligned}
\mathcal{L} = & \psi_\sigma^* (\partial_\tau - \frac{\nabla^2}{2m} - \mu_\sigma) \psi_\sigma + \boldsymbol{\phi}^* \cdot (\partial_\tau - \frac{\nabla^2}{4m} - \mu_m) \cdot \boldsymbol{\phi} + \frac{\lambda_\sigma}{2} |\psi_\sigma|^4 \\
& + \lambda_{12} |\psi_1|^2 |\psi_2|^2 + g_{am} (|\psi_1|^2 + |\psi_2|^2) |\boldsymbol{\phi}|^2 + \frac{g_1}{2} |\boldsymbol{\phi}^* \cdot \boldsymbol{\phi}|^2 + \frac{g_2}{2} |\boldsymbol{\phi} \cdot \boldsymbol{\phi}|^2 \\
& + \frac{\alpha}{2} (\boldsymbol{\phi}^* \cdot [\psi_1 (-i\nabla) \psi_2 - \psi_2 (-i\nabla) \psi_1] + c.c.). \tag{2.28}
\end{aligned}$$

Above (and throughout), the summation over a repeated index, as for σ in the first term, is implied.

We note that closely related models also arise in completely distinct physically contexts. These include quantum magnets that exhibit incommensurate spin liquids states [116] and bosonic atoms in the presence of spin-orbit interactions [117].

The associated coherent-state action S will be the basis of all of our analysis in subsequent sections for the computation of the phase diagram, the nature of the phases and excitations in each of the corresponding phases of a p -wave resonant Bose gas.

2.3 Phases and their symmetries

Before turning to a microscopic analysis, it is instructive to consider the nature of the expected phases, corresponding Goldstone modes and associated phase transitions based on the underlying symmetries and their spontaneous breaking.

The fully disordered symmetric state of our two-component Bose gas confined inside an isotropic and homogeneous [118] trap exhibits the $U_N(1) \otimes U_{\Delta N}(1) \otimes O(3) \otimes T_r \otimes \mathcal{T}$ symmetries. The first two $U(1)$ groups are associated with the total (whether in atomic or molecular form) atom number $N = N_1 + N_2 + 2N_m$ and the atom species number difference $\Delta N = N_1 - N_2$ conservations. The $O(3) \times T_r$ symmetries correspond to the Euclidean group of three dimensional rotations and translations (in a trap-free case), and \mathcal{T} is a symmetry of time reversal.

Since our system is composed of **bosonic** atoms and molecules confined to a large trap [119], at sufficiently low temperature we expect it to be a superfluid, that in three dimensions exhibits Bose-Einstein condensation, characterized by complex scalar atomic, Ψ_σ and/or 3-vector molecular, $\boldsymbol{\Phi}$ order parameters. Thus, in addition to the high temperature normal (non-superfluid) state,

where above order parameters all vanish and the full symmetry $U_N(1) \otimes U_{\Delta N}(1) \otimes O(3) \otimes \mathcal{T} \otimes T_r$ is manifest [120], at low temperature we expect the system to exhibit three classes of SF phases:

- (1) Atomic Superfluid (ASF), $\Psi_\sigma \neq 0$ and $\Phi = 0$
- (2) Molecular Superfluid (MSF), $\Psi_\sigma = 0$ and $\Phi \neq 0$
- (3) Atomic Molecular Superfluid (AMSF), $\Psi_\sigma \neq 0$ and $\Phi \neq 0$

that spontaneously break one or more of the above symmetries. Although these phase classes resemble the previously studied phases of *s*-wave Feshbach-resonant system [34, 35, 36], as will be clear from the following discussion, there are important qualitative differences.

2.3.1 Atomic superfluid phases, ASF

At large **positive** detuning ν it is clear that the molecules are gapped and all atoms are in the unpaired open channel. In this regime, the gapped molecules can be neglected (or integrated out) and the Hamiltonian (2.9) reduces to that of two bosonic atom species, that can exhibit Bose-condensation characterized by Ψ_1, Ψ_2 condensates. Such two-component system is characterized by two types of phase diagram topologies, and has been extensively studied in the statistical physics community [121, 122, 123].

For $a_1 a_2 > a_{12}^2$ it admits three ASF phases:

- (1) ASF₁ ($\Psi_1 \neq 0, \Psi_2 = 0$),
- (2) ASF₂ ($\Psi_1 = 0, \Psi_2 \neq 0$),
- (3) ASF₁₂ ($\Psi_1 \neq 0, \Psi_2 \neq 0$)

with ASF₁ and ASF₂ separated from ASF₁₂ and the normal phases by continuous phase transitions driven by temperature and density, or atomic polarization (or equivalently the chemical potential imbalance) as illustrated in a mean-field phase diagram, Fig. 2.6. These phases clearly break $U_1(1)$, $U_2(1)$, or both of these symmetries, respectively, and are therefore expected to exhibit conventional Bogoliubov modes corresponding to these $U(1)$ symmetries.

Alternatively, for $a_1 a_2 < a_{12}^2$, the ASF_{12} state is unstable, with ASF_1 and ASF_2 separated by a first-order transition and the associated phase separation visible in a trap.

We emphasize that in contrast to the s -wave FR bosonic system (where atomic condensation necessarily induces a molecular one, and therefore ASF phase is not qualitatively distinct from the s -wave AMSF phase, separated from it by a smooth crossover) [34, 35, 36], for a p -wave FR, above $k = 0$ atomic ASF condensates do **not** automatically induce a p -wave molecular condensate since for $k = 0$ the p -wave FR coupling vanishes. Thus the ASF class of phases is qualitatively distinct from the AMSF class that we discuss below.

2.3.2 Molecular superfluid phases, MSF

In the opposite limit of a large **negative** detuning, atoms are gapped, tightly bound into heteromolecules, that at low temperature condense into a p -wave molecular superfluid, MSF. In this regime of atomic vacuum, the gas reduces to that of interacting p -wave molecules, a system quite clearly isomorphic to that of the extensively studied $F = 1$ spinor condensate [83, 84, 85, 88, 89, 90, 91, 92, 93], with the hyperfine spin F here replaced by the orbital $\ell = 1$ angular momentum of two constituent atoms.

Like $F = 1$ spinor condensates, the p -wave molecular superfluid, MSF can exhibit two distinct phases depending on the sign of the renormalized interaction coupling g_2 in Eq. (2.21), or equivalently the sign of the difference $a_0^{(m)} - a_2^{(m)}$ of the molecular $L = 0$ and $L = 2$ channels s -wave scattering lengths [124].

2.3.2.1 Ferromagnetic molecular superfluid, MSF_{fm}

For $g_2 > 0$ the ground state is the so-called “ferromagnetic” molecular superfluid, MSF_{fm} , characterized by an order parameter $\Phi = \frac{\Phi_{fm}}{\sqrt{2}}(\hat{n} \pm i\hat{m})$, with \hat{n} , \hat{m} , $\hat{\ell} \equiv \hat{n} \times \hat{m}$ a real orthonormal triad, Φ_{fm} a real amplitude, and the state corresponds to $\ell_z = \pm 1$ projection of the internal molecular orbital angular momentum along the $\hat{\ell}$ axis. MSF_{fm} spontaneously breaks the time reversal, the $O(3)$ rotational and the global gauge symmetry $U_N(1)$, latter corresponding to a total

atom number N conservation. Inside MSF_{fm} the low-energy order parameter manifold is that of the $O(3) = SU(2)/\mathbb{Z}_2$ group, corresponding to orientations of the orthonormal triad $\hat{\mathbf{n}}, \hat{\mathbf{m}}, \hat{\mathbf{l}}$.

As its hyperfine spinor-condensate cousin, ferromagnetic MSF_{fm} , exhibits two gapless Goldstone modes, one linear ($\propto k$) Bogoliubov mode associates with the broken global gauge symmetry, and another quadratic ($\propto k^2$) corresponding to the ferromagnetic order, with associated spin-waves [84] reflecting the precessional FM dynamics.

2.3.2.2 Polar molecular superfluid, MSF_p

Alternatively, for $g_2 < 0$ the ground state is the so-called “polar” [125] molecular superfluid, MSF_p , characterized by a (collinear) order parameter $\Phi = \Phi_p e^{i\varphi} \hat{\mathbf{n}}$, with $\hat{\mathbf{n}}$ a real unit vector, φ a (real) phase, and Φ_p a (real) order-parameter amplitude, with the state corresponding to $\ell_z = 0$ projection of the internal molecular orbital angular momentum along $\hat{\mathbf{n}}$. MSF_p clearly spontaneously breaks rotational symmetry by its choice of the $\ell_z = 0$ quantization axis $\hat{\mathbf{n}}$, and the global gauge symmetry, corresponding to a total atom number conservation. The low-energy order parameter manifold that characterizes MSF_p is given by the coset space $(U(1) \otimes S_2)/\mathbb{Z}_2$, admitting half-integer “charge” vortices [93] akin to (but distinct from) the s -wave MSF [34, 36, 35].

As we demonstrate explicitly in Sec.2.5, based on symmetry we expect the polar MSF_p state to exhibit three gapless Bogoliubov-like modes. One corresponds to breaking of the global atom number conservation and two associated with breaking of rotational $O(3)$ symmetry [84].

2.3.3 Atomic-molecular superfluid phases, AMSF

As detuning is increased from large negative values of the $\text{MSF}_{p,\text{fm}}$ phases, for intermediate ν the gap to atomic excitations decreases, closing at a critical value of $\nu_c^{\text{MSF-AMSF}}$ at which, in addition an atomic Bose condensation takes place. General arguments show that this precedes the atomic condensation in the absence of FR coupling, i.e., $\nu_c^{\text{MSF-AMSF}}(\alpha) < \nu_c^{\text{MSF-AMSF}}(0)$. The novel features of this MSF-AMSF transition and the AMSF phase are derived from the fact that at these intermediate detuning, the atomic condensation necessarily takes place at a **finite** momentum

$k = Q$, set by a balance of the p -wave FR hybridization and the atomic kinetic energies.

We emphasize that in contrast to the s -wave Feshbach-resonant bosons [34, 35], for which an atomic condensate necessarily induces a molecular condensate, thereby erasing a qualitative distinction between the AMSF and ASF states, for the p -wave case, ASF and AMSF phases are qualitatively distinct [34]. The latter is ensured by the momentum dependent nature of the p -wave coupling that breaks spatial rotational invariance and vanishes for $\mathbf{Q} = 0$.

As with other crystalline states of matter [126, 8, 9], the detailed nature of the resulting AMSF states depends on the symmetry of the crystalline order, set by the reciprocal lattice vectors, \mathbf{Q}_n at which condensation takes place. Determined by a detailed nature of interactions and fluctuations, typically the nature of crystalline order is challenging to determine generically. Here we will focus on the **collinear** states, with a parallel set of $\mathbf{Q}_n = n\mathbf{Q}$, that in the present system can be generically shown to be energetically preferred in the AMSF_p state. There are two possible classes of such collinear states, that are bosonic condensate analogs of the Fulde-Ferrell (FF) [8] and Larkin-Ovchinnikov (LO) [9] states, extensively studied in fermionic paired superconductors and superfluids [104, 105, 106]. The qualitative features of these classes of finite-momentum superfluids are well-captured by two simplest representative states, one with a single \mathbf{Q} and the other with a pair of $\pm\mathbf{Q}$ condensate, that we respectively denote as “vector”, AMSF^v and “smectic”, AMSF^s atomic-molecular superfluids. With a choice of \mathbf{Q} the AMSF^{v,s} states both break spatial rotational symmetry. However, they are qualitatively distinguished by the AMSF^v also spontaneously breaking the time-reversal symmetry, while remaining homogeneous, and the AMSF^s instead also breaking the translational symmetry along \mathbf{Q} , while remaining symmetric under the time reversal. Because within a mean-field theory analysis it is the former, vector state that appears to be favored, for simplicity we focus on the single \mathbf{Q} AMSF states.

The nature and symmetries of these AMSF states furthermore qualitatively depends on the parent MSF, with the ferromagnetic AMSF_{fm} and polar AMSF_p as two possibilities depending on the sign of the renormalized interaction coupling g_2 . In addition to the symmetries already broken in its MSF parent, by virtue of atomic condensation the AMSF state breaks the remaining $U_{\Delta N}(1)$

global gauge symmetry associated with the conservation of the difference in atom species number, ΔN . Other symmetries that it breaks depend on the detailed structure of the $\text{AMSF}_{\text{fm,p}}^{v,s}$ states.

2.3.3.1 Polar atomic-molecular superfluid, AMSF_p

The polar atomic-molecular superfluid AMSF_p emerges from the polar molecular state, MSF_p . As we will see in the next section, in the AMSF_p the finite momentum atomic condensate orders with \mathbf{Q} along the molecular condensate field Φ , and therefore (as illustrated in Fig.2.4) for a single \mathbf{Q} the vector superfluid does not break any additional spatial symmetries. With the molecular quantization axis, Φ locked to the atomic condensate momentum \mathbf{Q} , on general symmetry grounds (simultaneous rotations of Φ and \mathbf{Q} is a zero-energy Goldstone mode), we expect and indeed find that (see Sec. 2.5.3) the superfluid phase will be characterized by a smectic [126] Goldstone mode Hamiltonian. The smectic AMSF_p^s superfluid, in addition breaks translational symmetry along Φ , with low-energy fluctuations about this state described by a smectic phonon u and a superfluid phase φ Goldstone modes.

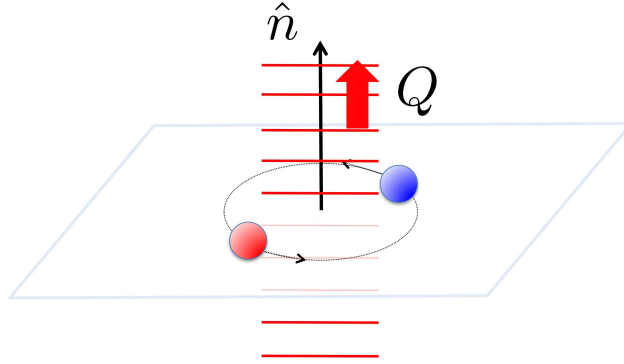


Figure 2.4: Schematic of the AMSF_p polar state. The thick arrow indicates the atomic condensate momentum \mathbf{Q} and the \hat{n} arrow denotes the quantization axis along which the projection of molecular internal orbital angular momentum vanishes.

2.3.3.2 Ferromagnetic atomic-molecular superfluid, AMSF_{fm}

In contrast, a finite-momentum atomic condensation from the MSF_{fm} leads to the ferromagnetic atomic-molecular superfluid, AMSF_{fm} . In this state, a p -wave Feshbach resonant interaction leads to the energetic preference for a transverse orientation of the atomic condensate momentum \mathbf{Q} to the molecular quantization axis, $\hat{\ell} = \hat{n} \times \hat{m}$. Consequently, as illustrated in Fig.2.5, the AMSF_{fm} state breaks additional orientational symmetry of the uniaxial molecular state in the plane transverse to the molecular quantization axis $\hat{\ell}$. That is, the AMSF_{fm} state is a biaxial nematic superfluid defined by \mathbf{Q} and $\hat{\ell}$ axes, with the superfluid phase described by a smectic[126] Goldstone mode Hamiltonian akin to that of the FF state [110]. The latter form is enforced by the symmetry associated with a simultaneous reorientation of atomic momentum \mathbf{Q} and molecular gauge transformation. The biaxial smectic AMSF_{fm}^s superfluid, in addition breaks translational symmetry along \mathbf{Q} , with low-energy fluctuations about this state described by two Goldstone modes, that are a smectic phonon u and a superfluid phase φ .

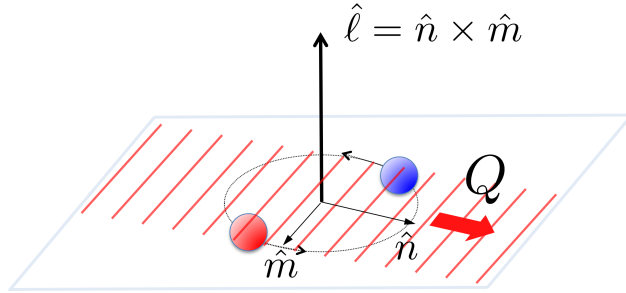


Figure 2.5: Schematic of the AMSF_{fm} ferromagnetic state. The thick arrow indicates the atomic condensate momentum \mathbf{Q} , lying in the plane transverse to the quantization axis $\hat{\ell}$, along which the projection of the molecular internal orbital angular momentum is $\ell_z = +1$.

2.4 Mean Field Theory

Our main goal in this paper is to establish the phase diagram and nature of phase transitions exhibited by the p -wave Feshbach-resonant two-component Bose gas. This requires a minimization of the free energy which, in the presence of interactions and fluctuations is a nontrivial function of a number of system's physical parameters. However, outside the critical region, inside each phase where fluctuations are small [127], we can approximate the Landau free-energy functional $F[\Psi_\sigma, \Phi]$ by replacing the atomic and molecular coherent state fields with the classical order parameters, $\Psi_\sigma(\mathbf{r})$, $\Phi(\mathbf{r})$, that minimize the action S via the saddle-point method. In the simplest approximation, the Landau free-energy functional $F[\Psi_\sigma, \Phi]$ takes the form identical to $H[\hat{\psi}_\sigma, \hat{\phi}]$,

$$F[\Psi_\sigma, \Phi] = \int d^3r \left[\sum_{\sigma=1,2} \left(\Psi_\sigma^* \tilde{\varepsilon}_\sigma \Psi_\sigma + \frac{\tilde{\lambda}_\sigma}{2} |\Psi_\sigma|^4 \right) + \tilde{\lambda}_{12} |\Psi_1|^2 |\Psi_2|^2 + \tilde{g}_{am} (|\Psi_1|^2 + |\Psi_2|^2) |\Phi|^2 \right. \\ \left. + \Phi^* \cdot \tilde{\omega} \cdot \Phi + \frac{\tilde{g}_1}{2} |\Phi^* \cdot \Phi|^2 + \frac{\tilde{g}_2}{2} |\Phi \cdot \Phi|^2 + \frac{\tilde{\alpha}}{2} (\Phi^* \cdot [\Psi_1(-i\nabla)\Psi_2 - \Psi_2(-i\nabla)\Psi_1]) + c.c. \right] \quad (2.29)$$

with the effective couplings $(\tilde{\mu}_\sigma, \tilde{\mu}_m, \tilde{\lambda}_\sigma, \dots)$, that are functions of the microscopic parameters $(\mu_\sigma, \mu_m, \lambda_\sigma, \dots)$ in Eq. (2.9), encoding all the complexity of the fluctuations and interactions on short scales. Though nontrivial, these parameters are in principle derivable from the Hamiltonian. However, we will not be concerned with this aspect of the problem. Instead our goal is to capture the qualitative form of the phase diagram, taking fluctuations into account only when they qualitatively modify the nature of the phases and phase transitions. For simplicity of notation, we will therefore neglect the distinction between the microscopic and effective couplings, dropping tildes.

2.4.1 Order parameters

We begin by introducing order parameters that in mean-field approximation completely characterize the states of the system. In contrast to a conventional (s -wave interacting) Bose gas, anticipating the energetics, we allow the atomic condensates $\Psi_1(\mathbf{r})$ and $\Psi_2(\mathbf{r})$ to be complex **periodic**

functions characterized by momenta \mathbf{Q}_n , with the simplest **single** $\mathbf{Q}_1 = \mathbf{Q}$ form given by

$$\psi_1(\mathbf{r}) \rightarrow \Psi_1(\mathbf{r}) = \Psi_{1,\mathbf{Q}} e^{i\mathbf{Q}\cdot\mathbf{r}}, \quad (2.30)$$

$$\psi_2(\mathbf{r}) \rightarrow \Psi_2(\mathbf{r}) = \Psi_{2,-\mathbf{Q}} e^{-i\mathbf{Q}\cdot\mathbf{r}}, \quad (2.31)$$

$$\phi(\mathbf{r}) \rightarrow \Phi, \quad (2.32)$$

where Φ is a complex 3-vector order parameter characteristic of the $\ell = 1$ molecular condensate and the choice of $\pm\mathbf{Q}$ momentum relation for the two atomic condensate fields is dictated by momentum conservation.

More generally, the atomic condensate order parameter is given by

$$\Psi_\sigma(\mathbf{r}) = \begin{pmatrix} \Psi_1(\mathbf{r}) \\ \Psi_2(\mathbf{r}) \end{pmatrix} = \sum_{\mathbf{Q}_n} \begin{pmatrix} \Psi_{1,\mathbf{Q}_n} e^{i\mathbf{Q}_n\cdot\mathbf{r}} \\ \Psi_{2,-\mathbf{Q}_n} e^{-i\mathbf{Q}_n\cdot\mathbf{r}} \end{pmatrix}. \quad (2.33)$$

However, as alluded to in the previous section, based on the energetics of the model, we expect that for most of the phase diagram a single $\mathbf{Q}_n = \mathbf{Q}$ and double $\mathbf{Q}_n = \pm\mathbf{Q}$ collinear forms of the atomic order parameters are sufficient to capture the ground-state atomic condensates. The latter Larkin-Ovchinnikov like form can equivalently, more simply be written as

$$\Psi_\sigma(\mathbf{r}) = \Psi_{\sigma,\mathbf{Q}} e^{i\mathbf{Q}\cdot\mathbf{r}} + \Psi_{\sigma,-\mathbf{Q}} e^{-i\mathbf{Q}\cdot\mathbf{r}}, \quad (2.34)$$

with $\Psi_{\sigma,\pm\mathbf{Q}}$, Φ , and \mathbf{Q} to be determined by the minimization of the mean-field free energy. As we demonstrate in Appendix A, it is the single \mathbf{Q} (Fulde-Ferrell like) condensate that is preferred energetically in a mean-field approximation, and will therefore be the primary focus of the analysis presented here.

The molecular condensate complex order parameter Φ can in general be decomposed in terms of orthonormal real 3-vectors \mathbf{u} and \mathbf{v} , [33]

$$\Phi = \mathbf{u} + i\mathbf{v}. \quad (2.35)$$

As we will demonstrate explicitly shortly, in this representation the two possible $\ell = 1$ molecular

superfluids, ferromagnetic and polar condensates are described by

$$\mathbf{u} \perp \mathbf{v}, \text{ “ferromagnetic”, } \ell_z = \pm 1 \text{ condensate,} \quad (2.36)$$

$$\mathbf{u} \parallel \mathbf{v}, \text{ “polar”, } \ell_z = 0 \text{ condensate,} \quad (2.37)$$

where for ferromagnetic state $u = v$ and the polar state can obviously be equivalently characterized by a vanishing of one (but not both) of \mathbf{u} and \mathbf{v} . These two molecular condensate states are the bosonic analogues of the $p_x + ip_y$ and p_x p -wave paired superfluids [57, 33].

We next consider the Landau free-energy as a function of these atomic and molecular order parameters, and by minimizing it for a range of experimentally tunable parameters, compute the mean-field phase diagram for this p -wave resonant two-component Bose gas.

2.4.2 Atomic Superfluid (ASF)

As is clear from Eqs.(2.12),(2.29) for large *positive* detuning, ν the molecular chemical potential $\mu_m < 0$ is negative, with molecules gapped and therefore the ground state is a molecular vacuum. We can thus safely integrate out the small Gaussian molecular excitations, leading to an effective atomic free-energy

$$\begin{aligned} F_a[\Psi_\sigma] &\approx F[\Psi_\sigma, 0] \\ &\approx \int d^3r \left[\sum_{\sigma=1,2} \left(\Psi_\sigma^* \hat{\varepsilon}_\sigma \Psi_\sigma + \frac{\lambda_\sigma}{2} |\Psi_\sigma|^4 \right) + \lambda_{12} |\Psi_1|^2 |\Psi_2|^2 \right] \end{aligned} \quad (2.38)$$

with coefficients that are only slightly modified from their bare values in Eq. (2.29). This functional is a special $U(1) \otimes U(1)$ form of a $O(N) \otimes O(M)$ model, first studied many years ago by M. E. Fisher *et al.* and more recently in the magnetic and many other contexts [121, 122, 123]. This free-energy is clearly minimized by a spatially uniform atomic order parameters, Ψ_σ , giving

$$f_{\text{asf}} = F[|\Psi_\sigma|, 0]/V \quad (2.39)$$

$$= \sum_{\sigma=1,2} \left[-\mu_\sigma |\Psi_\sigma|^2 + \frac{\lambda_\sigma}{2} |\Psi_\sigma|^4 \right] + \lambda_{12} |\Psi_1|^2 |\Psi_2|^2 \quad (2.40)$$

as the ASF free-energy density.

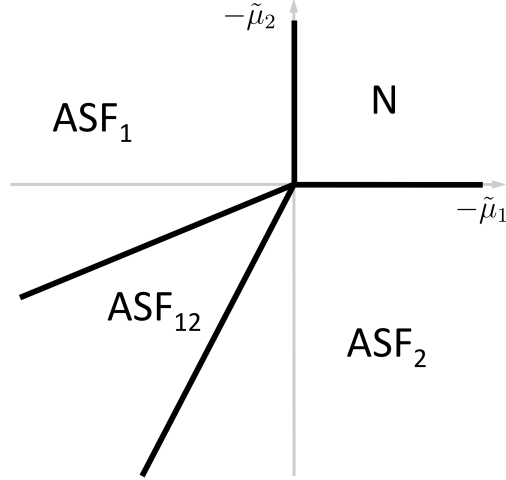


Figure 2.6: Mean-field phase diagram of a p -wave resonant two-component Bose gas for large positive detuning. Molecules are gapped, reducing the system to a conventional two-component Bose gas, for $\lambda_1\lambda_2 > \lambda_{12}^2$ displaying three types of ASF phases.

A minimization of f_{asf} , leads to 4 states corresponding to condensed and normal (nonsuperfluid) combinations of the two-component Bose gas. For both chemical potentials negative, $\mu_1 < 0$, $\mu_2 < 0$, both atoms are in the noncondensed, normal (N) phase

$$|\Psi_1| = |\Psi_2| = 0. \quad (2.41)$$

On a lattice (e.g., generated by a periodic optical potential [128]) at commensurate atom filling, this would correspond to a Mott insulating phase extending down to zero temperature. In a continuum (e.g., a trap), the normal state can only be realized by heating the gas above its degeneracy temperature.

As physical parameters are varied (e.g., a weaker periodic potential, lower temperature and higher density for one of the atomic species) for asymmetric mixture (different densities and/or masses) one of the two atomic chemical potentials, μ_1, μ_2 can turn positive, leading to a conventional normal-superfluid transition to ASF_1 or ASF_2 states, respectively. The order parameters and mean-

field phase boundaries in each of these conventional single component atomic BECs are given by

$$\text{ASF}_1: \quad \Psi_1 = \sqrt{\frac{\mu_1}{\lambda_1}}, \Psi_2 = 0, \text{ for } \mu_1 > 0, \mu_2 < \frac{\lambda_{12}}{\lambda_1} \mu_1, \quad (2.42)$$

$$\text{ASF}_2: \quad \Psi_1 = 0, \Psi_2 = \sqrt{\frac{\mu_2}{\lambda_2}}, \text{ for } \mu_2 > 0, \mu_1 < \frac{\lambda_{12}}{\lambda_2} \mu_2. \quad (2.43)$$

We note that generically for a **symmetric** two-component Bose mixture, these phases will be avoided by symmetry.

Further changes in system's parameters, so as to drive both chemical potentials positive, for $\lambda_1 \lambda_2 > \lambda_{12}^2$ leads to $\text{ASF}_1 - \text{ASF}_{12}$ or $\text{ASF}_2 - \text{ASF}_{12}$ transitions. The resulting two-component condensate, ASF_{12} is characterized by two nonzero atomic condensates and mean-field phase boundaries given by

$$\begin{aligned} \text{ASF}_{12}: \quad \Psi_1 &= \left[\frac{\lambda_2 \mu_1 - \lambda_{12} \mu_2}{\lambda_1 \lambda_2 - \lambda_{12}^2} \right]^{\frac{1}{2}}, \Psi_2 = \left[\frac{\lambda_1 \mu_2 - \lambda_{12} \mu_1}{\lambda_1 \lambda_2 - \lambda_{12}^2} \right]^{\frac{1}{2}}, \\ &\text{for } \mu_1 > 0, \mu_2 > 0, \frac{\lambda_2}{\lambda_{12}} > \frac{\mu_2}{\mu_1} > \frac{\lambda_{12}}{\lambda_1}. \end{aligned} \quad (2.44)$$

These classical phase transitions are generically continuous, in the XY universality class, breaking the associated $U(1)$ symmetries. The N- ASF_{12} transition only takes place in a fine-tuned balanced mixture $\mu_1 = \mu_2$ (that is our primary focus here) going directly through a tetracritical point, $\mu_1 = \mu_2 = 0$. Extensive studies demonstrate it to be in the *decoupled* universality class [121, 122, 123].

For $\lambda_1 \lambda_2 < \lambda_{12}^2$, the ASF_1 and ASF_2 energies cross before either becomes locally unstable. Consequently, instead of continuous transitions to the ASF_{12} state, the two-component ASF_{12} is absent and the ASF_1 and ASF_2 phases are separated by a first-order transition, located at

$$\mu_2 = \sqrt{\frac{\lambda_2}{\lambda_1}} \mu_1 \quad (2.45)$$

that terminates at a bicritical point. On this critical line the ASF_1 and ASF_2 states coexist and spatially phase separate.

2.4.3 Molecular Superfluid (MSF)

In the opposite limit of large *negative* detuning, i.e. $-\nu \gg |\mu|$, open-channel atoms are gapped and the ground state is an atomic vacuum. Hence for $\mu < 0$ the free energy $F[\Psi_\sigma, \Phi]$ is

minimized by $\Psi_\sigma = 0$ and a uniform molecular condensate Φ . The free-energy density then reduces to

$$\begin{aligned} f_{\text{msf}}[\Phi] &= F[0, \Phi]/V, \\ &= -\mu_m |\Phi|^2 + \frac{g_1}{2} |\Phi^* \cdot \Phi|^2 + \frac{g_2}{2} |\Phi \cdot \Phi|^2, \end{aligned} \quad (2.46)$$

$$= -\mu_m (u^2 + v^2) + \frac{g_1}{2} (u^2 + v^2)^2 + \frac{g_2}{2} (u^2 - v^2)^2, \quad (2.47)$$

identical to a spinor-1 bosonic condensate, corresponding to the $\ell = 1$ molecular Bose gas. Thus, the thermodynamics and low-energy excitations of the MSF are isomorphic to that of the well-studied spin-1 Bose condensate [84, 85].

The minimization of $f_{\text{msf}}[\Phi]$ then leads to two superfluid phases, the ‘‘polar’’ MSF_p for $g_2 < 0$ and the ‘‘ferromagnetic’’ MSF_{fm} for $g_2 > 0$ molecular condensates. For the polar MSF, the order parameter is given by

$$\Phi = \sqrt{\frac{\mu_m}{g_1 + g_2}} \hat{n} = \Phi_p \hat{n}, \quad \text{for } g_2 < 0, \quad (2.48)$$

spanning the $[U(1) \times S_2]/\mathbb{Z}_2$ manifold of degenerate ground states. For the ferromagnetic MSF, we instead find

$$\Phi = \sqrt{\frac{\mu_m}{2g_1}} (\hat{n} + i\hat{m}) = \frac{\Phi_{\text{fm}}}{\sqrt{2}} (\hat{n} + i\hat{m}), \quad \text{for } g_2 > 0, \quad (2.49)$$

spanning the $SO(3)$ manifold of states. In above, $\hat{n}, \hat{m}, \hat{l} \equiv \hat{n} \times \hat{m}$ is an orthonormal triad and $\Phi_{p,\text{fm}}$ are complex order-parameter amplitudes, breaking the $SO(3) \times U_N(1)$ symmetry of the disordered phase. For finite T the N-MSF transitions are in the well-studied universality class of a complex $O(3)$ model [84]. The MSF_p and MSF_{fm} are separated by a first-order transition, at $g_2 = 0$ in mean-field approximation.

2.4.4 Atomic Molecular Superfluid (AMSF)

For the intermediate detuning, we consider a condensation of both atoms and molecules, for generality allowing atoms to condense at a nonzero momentum. The latter is motivated by the discussion in the Introduction of the p -wave atom-molecule Feshbach coupling, that drives such finite momentum atom condensation [72, 71].

To analyze the phase boundaries and the behavior of the order parameters in the AMSF phase, it is convenient to approach the AMSF state from the MSF phase at negative detuning, where molecular condensate is well formed, and study the atomic condensation upon the increase of the detuning and of the atomic chemical potential.

We focus on the simpler case of a single momentum, \mathbf{Q} atomic condensate, that we will also later find to be the preferred form of the AMSF state. We relegate to Appendix A the conceptually straightforward, but technically slightly involved analysis of the more general $\pm\mathbf{Q}$ momenta state.

Using the order parameter form from Eq.(2.30),(2.31), and (2.32) inside the mean-field free-energy density $f_{\text{amsf}} = F[\Psi_\sigma, \Phi]/V = f_Q + f_{\text{msf}}$, we obtain

$$\begin{aligned} f_Q &= \varepsilon_Q (\Psi_{1,\mathbf{Q}}^* \Psi_{1,\mathbf{Q}} + \Psi_{2,-\mathbf{Q}}^* \Psi_{2,-\mathbf{Q}}) - \Delta_{\mathbf{Q}} \Psi_{1,\mathbf{Q}}^* \Psi_{2,-\mathbf{Q}} - \Delta_{\mathbf{Q}}^* \Psi_{1,\mathbf{Q}} \Psi_{2,-\mathbf{Q}} \\ &\quad + \frac{\lambda_1}{2} |\Psi_{1,\mathbf{Q}}|^4 + \frac{\lambda_2}{2} |\Psi_{2,-\mathbf{Q}}|^4 + \lambda_{12} |\Psi_{1,\mathbf{Q}}|^2 |\Psi_{2,-\mathbf{Q}}|^2 \end{aligned} \quad (2.50)$$

where $\varepsilon_Q = \frac{Q^2}{2m} - \mu + g_{am} |\Phi|^2$, $\Delta_{\mathbf{Q}} = \alpha \Phi \cdot \mathbf{Q} \equiv |\Delta_{\mathbf{Q}}| e^{i\varphi_0}$, and for simplicity we specialized to a balanced mixture set by $\mu_1 = \mu_2 = \mu$. To determine the nature of the atomic condensate in the AMSF state, we diagonalize the quadratic part of the free-energy density, f_Q^0 with a unitary transformation U_0 ,

$$U_0 = \frac{1}{\sqrt{2}} \begin{pmatrix} e^{i\varphi_0} & -e^{i\varphi_0} \\ 1 & 1 \end{pmatrix}, \quad (2.51)$$

obtaining

$$f_Q^0 = \begin{pmatrix} \Psi_{1,\mathbf{Q}}^* & \Psi_{2,-\mathbf{Q}} \end{pmatrix} \begin{pmatrix} \varepsilon_Q & -\Delta_{\mathbf{Q}} \\ -\Delta_{\mathbf{Q}}^* & \varepsilon_Q \end{pmatrix} \begin{pmatrix} \Psi_{1,\mathbf{Q}} \\ \Psi_{2,-\mathbf{Q}} \end{pmatrix}, \quad (2.52)$$

$$= \begin{pmatrix} \Psi_-^* & \Psi_+ \end{pmatrix}_{\mathbf{Q}} U_0^\dagger \begin{pmatrix} \varepsilon_Q & -\Delta_{\mathbf{Q}} \\ -\Delta_{\mathbf{Q}}^* & \varepsilon_Q \end{pmatrix} U_0 \begin{pmatrix} \Psi_- \\ \Psi_+ \end{pmatrix}_{\mathbf{Q}}, \quad (2.53)$$

$$= \epsilon_{\mathbf{Q}}^+ |\Psi_+|^2 + \epsilon_{\mathbf{Q}}^- |\Psi_-|^2, \quad (2.54)$$

where

$$\begin{pmatrix} \Psi_- \\ \Psi_+^* \end{pmatrix}_{\mathbf{Q}} = U_0^\dagger \begin{pmatrix} \Psi_{1,\mathbf{Q}} \\ \Psi_{2,-\mathbf{Q}}^* \end{pmatrix} = \frac{1}{\sqrt{2}} \begin{pmatrix} e^{-i\varphi_0} \Psi_{1,\mathbf{Q}} + \Psi_{2,-\mathbf{Q}}^* \\ -e^{-i\varphi_0} \Psi_{1,\mathbf{Q}} + \Psi_{2,-\mathbf{Q}}^* \end{pmatrix}, \quad (2.55)$$

and

$$\epsilon_{\mathbf{Q}}^+ = \epsilon_{\mathbf{Q}} + |\Delta_{\mathbf{Q}}|, \quad \epsilon_{\mathbf{Q}}^- = \epsilon_{\mathbf{Q}} - |\Delta_{\mathbf{Q}}|. \quad (2.56)$$

Expressing the quartic terms of the free-energy density in terms of the diagonalized atomic condensate fields, Ψ_{\pm} , we find

$$\begin{aligned} |\Psi_{1,\mathbf{Q}}|^4 &= \frac{1}{4} \left(|\Psi_+|^4 + |\Psi_-|^4 + 4|\Psi_+|^2|\Psi_-|^2 + (\Psi_+\Psi_-)^2 + (\Psi_+\Psi_-)^* \right. \\ &\quad \left. - 2|\Psi_+|^2(\Psi_+\Psi_- + \Psi_+\Psi_-^*) - 2|\Psi_-|^2(\Psi_+\Psi_- + \Psi_+\Psi_-^*) \right), \end{aligned} \quad (2.57)$$

$$\begin{aligned} |\Psi_{2,-\mathbf{Q}}|^4 &= \frac{1}{4} \left(|\Psi_+|^4 + |\Psi_-|^4 + 4|\Psi_+|^2|\Psi_-|^2 + (\Psi_+\Psi_-)^2 + (\Psi_+\Psi_-)^* \right. \\ &\quad \left. + 2|\Psi_+|^2(\Psi_+\Psi_- + \Psi_+\Psi_-^*) + 2|\Psi_-|^2(\Psi_+\Psi_- + \Psi_+\Psi_-^*) \right), \end{aligned} \quad (2.58)$$

$$|\Psi_{1,\mathbf{Q}}|^2|\Psi_{2,-\mathbf{Q}}|^2 = \frac{1}{4} \left(|\Psi_+|^4 + |\Psi_-|^4 - (\Psi_+\Psi_-)^2 - (\Psi_+\Psi_-)^* \right). \quad (2.59)$$

Since $\epsilon_{\mathbf{Q}}^- < \epsilon_{\mathbf{Q}}^+$, the MSF-AMSF transition takes place at $\epsilon_{\mathbf{Q}}^- = 0$, tuned to this point by the FR detuning, $\nu \rightarrow \nu_c^{\text{MSF-AMSF}}$. At higher detuning, $\nu > \nu_c^{\text{MSF-AMSF}}$, a finite momentum \mathbf{Q} atomic condensate develops, characterized by a nonzero order-parameter $\Psi_- \neq 0$, and $\Psi_+ = 0$. From the latter condition, we deduce that

$$\Psi_{2,-\mathbf{Q}}^* = e^{-i\varphi_0} \Psi_{1,\mathbf{Q}}, \quad (2.60)$$

and

$$\Psi_- = \sqrt{2} e^{-i\varphi_0} \Psi_{1,\mathbf{Q}}, \quad (2.61)$$

leading to a considerable simplification of the AMSF Landau free-energy density,

$$f_{\text{amsf}} = \epsilon_{\mathbf{Q}}^- |\Psi_-|^2 + \frac{1}{2} \lambda |\Psi_-|^4 - \mu_m |\mathbf{\Phi}|^2 + \frac{g_1}{2} |\mathbf{\Phi}^* \cdot \mathbf{\Phi}|^2 + \frac{g_2}{2} |\mathbf{\Phi} \cdot \mathbf{\Phi}|^2, \quad (2.62)$$

where $\lambda = \frac{1}{4}(\lambda_1 + \lambda_2 + 2\lambda_{12})$. The minimization of $f_{\text{amsf}}[\Psi_-, \mathbf{\Phi}]$ over the order parameters and the atomic momentum \mathbf{Q} is straightforward. The optimum $|\mathbf{Q}_0| = Q_0$ is given by,

$$\frac{\partial f_{\text{amsf}}}{\partial Q} = 0, \quad (2.63)$$

and leads to

$$Q_0 = \alpha m [(u^2 - v^2) \cos^2 \theta_{\mathbf{Q}} + v^2]^{1/2}, \quad (2.64)$$

with $\theta_{\mathbf{Q}}$ the angle between \mathbf{Q}_0 and \mathbf{u} . Without loss of generality taking $u > v$ and putting Q_0 back into the free energy shows that f_{amsf} is minimized by $\theta_{\mathbf{Q}} = 0$, i.e., by \mathbf{Q}_0 aligned along the longest of the \mathbf{u} and \mathbf{v} components, giving

$$Q_0 = \alpha m u \approx \alpha m \sqrt{n_m}. \quad (2.65)$$

Thus, as illustrated in Fig. 2.2, the momentum Q_0 is at its maximum value near the MSF-AMSF phase boundary and decreases continuously to zero with the molecular condensate n_m at the AMSF-ASF transition, tunable with a magnetic field via detuning, ν .

As in the treatment of the MSF phases, it is convenient to express the free energy in terms of the magnitudes of the real, \mathbf{u} and imaginary, \mathbf{v} vector components of $\mathbf{\Phi}$. Minimizing it over Ψ_- , we obtain

$$f_{\text{amsf}} = -\frac{1}{2\lambda} \left(\mu + \frac{m\alpha^2}{2} u^2 - g_{am}(u^2 + v^2) \right)^2 - \mu_m(u^2 + v^2) + \frac{g_1}{2}(u^2 + v^2)^2 + \frac{g_2}{2}(u^2 - v^2)^2, \quad (2.66)$$

with the atomic condensate given by

$$|\Psi_-| = \left[\left(\mu + \frac{m\alpha^2}{2} u^2 - g_{am}(u^2 + v^2) \right) / \lambda \right]^{1/2}. \quad (2.67)$$

Minimization of f_{amsf} with respect to u and v gives a number of solutions. In addition to the Normal ($\Psi_- = 0$, $\mathbf{\Phi} = u = v = 0$) and the ASF ($\Psi_- \neq 0$, $\mathbf{\Phi} = u = v = 0$) phases we find the polar, AMSF_p ($\Psi_- \neq 0$, $u \neq 0$, $v = 0$) and the ferromagnetic, AMSF_{fm} ($\Psi_- \neq 0$, $u > v \neq 0$) phases that are the descendants of the MSF_p and MSF_{fm} molecular condensates.

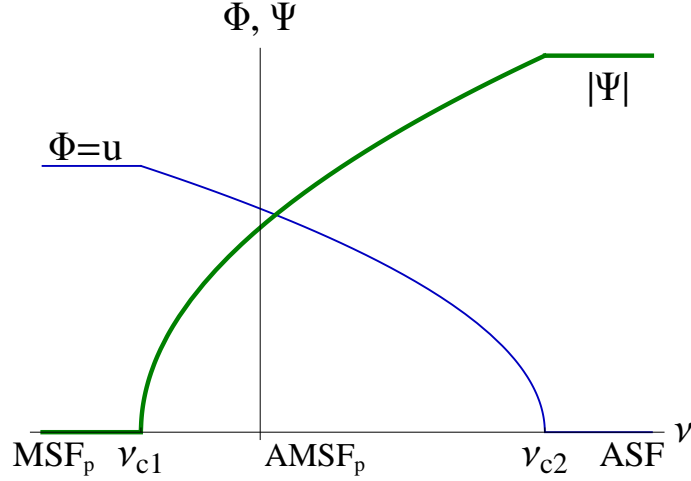


Figure 2.7: Schematic atomic (thick) and molecular (thin) order parameters versus the FR detuning ν for the polar phase, with $\nu_{c1} = \nu_c^{\text{MSF}_p\text{-AMSF}_p}$ and $\nu_{c2} = \nu_c^{\text{AMSF}_p\text{-ASF}}$.

2.4.4.1 Polar AMSF: AMSF_p

A straightforward minimization of $f_{\text{amsf}}[u, v]$, Eq.(2.66) for $g_2 < 0$ leads to the AMSF_p phase, characterized by order parameters,

$$u_p = \sqrt{\frac{\lambda\mu_m - \tilde{g}_{am}\mu}{\lambda(g_1 + g_2) - \tilde{g}_{am}^2}}, \quad v_p = 0, \quad (2.68)$$

$$|\Psi_{-,p}| = \sqrt{\frac{(g_1 + g_2)\mu - \tilde{g}_{am}\mu_m}{\lambda(g_1 + g_2) - \tilde{g}_{am}^2}}, \quad (2.69)$$

where $\tilde{g}_{am} = g_{am} - m\alpha^2/2$. The phase boundaries corresponding to the MSF_p - AMSF_p and the AMSF_p - ASF transitions are also easily worked out (set by the vanishing of the atomic and molecular condensates, respectively) and are given by

$$\nu_c^{\text{MSF}_p\text{-AMSF}_p} = -(g_1 + g_2 - 2\tilde{g}_{am}) n_m, \quad (2.70)$$

$$\approx -\frac{1}{2}(g_1 + g_2 - 2\tilde{g}_{am}) n, \quad (2.71)$$

$$\nu_c^{\text{AMSF}_p\text{-ASF}} = (2\lambda - \tilde{g}_{am}) n_a, \quad (2.72)$$

$$\approx (2\lambda - \tilde{g}_{am}) n, \quad (2.73)$$

where we used $\mu_m = 2\mu - \nu = (g_1 + g_2)n_m$ and $\mu = \lambda n_a$ to eliminate the molecular and atomic chemical potentials in favor of the molecular condensate n_m , the atomic condensate n_a and the

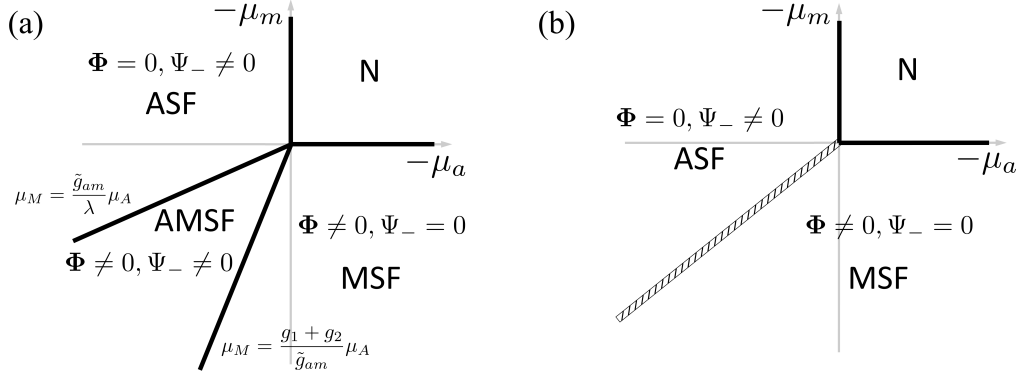


Figure 2.8: Mean field phase diagrams for polar phase as a function of atomic and molecular chemical potentials, μ_a , μ_m , respectively. Ferromagnetic phase is similar but with different parameters. (a) For $\lambda(g_1 + g_2) - \tilde{g}_{am}^2 > 0$, all three superfluid phases, ASF, AMSF, and MSF appear and are separated by continuous phase transitions (thick black lines), (b) For $\lambda(g_1 + g_2) - \tilde{g}_{am}^2 < 0$, AMSF is unstable, and the ASF and MSF are separated by a first-order transition (hatched double line).

detuning ν . We also used the fact that at low temperature and for weak interactions, $n_m \approx n/2$ and $n_a \approx n$ in the MSF and ASF, respectively.

It is clear from Fig. 2.8 (a) and Eq.(2.69) for $\Psi_{-,p}$ that the condition

$$\lambda(g_1 + g_2) - \tilde{g}_{am}^2 > 0 \quad (2.74)$$

is necessary for the stability of AMSF_p . We observe that in addition to setting the value of the finite momentum, Q_0 of the atomic condensate, the p -wave Feshbach-resonance coupling, α expands the stability of the AMSF phase. Within the mean-field approximation, the MSF_p - AMSF_p and AMSF_p -ASF transitions are of second order. This will be qualitatively modified, as we will see when we discuss fluctuation effects in Sec.2.6.

For $\lambda(g_1 + g_2) - \tilde{g}_{am}^2 < 0$ (Fig. 2.8 (b)), AMSF_p state is unstable, replaced by a direct first-order ASF- MSF_p transition. The corresponding phase boundary is given by the degeneracy condition of the ASF and MSF_p free-energies

$$f_{\text{asf}} = -\frac{\mu^2}{2\lambda} = -\frac{\mu_m^2}{2(g_1 + g_2)} = f_{\text{msf}_p}. \quad (2.75)$$

2.4.4.2 Ferromagnetic AMSF: AMSF_{fm}

A minimization of the free energy, $f_{\text{amsf}}[u, v]$ for a range of couplings shows that for intermediate detuning, the low-temperature state is the ferromagnetic AMSF_{fm}, characterized by

$$u_{fm} = \sqrt{\frac{2\lambda g_2 \mu_m - g_{am}^2 \mu_m - (g_1 + g_2) \tilde{g}_{am} \mu + (g_1 - g_2) g_{am} \mu + g_{am} \tilde{g}_{am} \mu_m}{4\lambda g_1 g_2 - 4g_2 g_{am} \tilde{g}_{am} - (g_1 + g_2)(m\alpha^2/2)^2}}, \quad (2.76)$$

$$v_{fm} = \sqrt{\frac{2\lambda g_2 \mu_m - \tilde{g}_{am}^2 \mu_m - (g_1 + g_2) g_{am} \mu + (g_1 - g_2) \tilde{g}_{am} \mu + g_{am} \tilde{g}_{am} \mu_m}{4\lambda g_1 g_2 - 4g_2 g_{am} \tilde{g}_{am} - (g_1 + g_2)(m\alpha^2/2)^2}}, \quad (2.77)$$

$$|\Psi_{fm}| = \sqrt{\frac{g_2(4g_1 \mu - 4g_{am} \mu_m + m\alpha^2 \mu_m)}{4\lambda g_1 g_2 - 4g_2 g_{am} \tilde{g}_{am} - (g_1 + g_2)(m\alpha^2/2)^2}}. \quad (2.78)$$

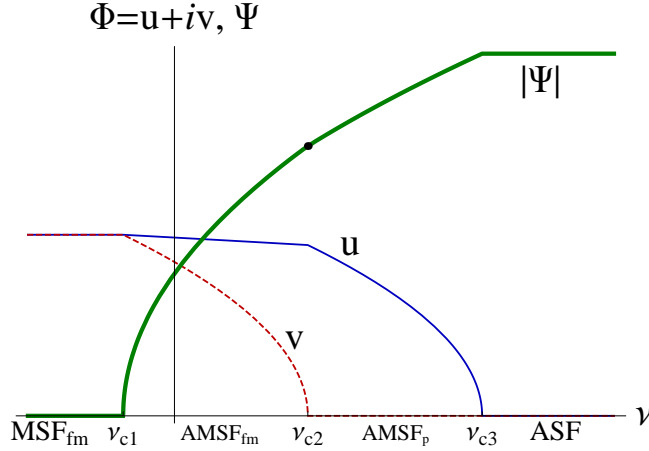


Figure 2.9: Schematic atomic (thick) and molecular (thin and dashed) order parameters versus the FR detuning ν for ferromagnetic phases. The AMSF_{fm}-AMSF_p phase transition at ν_{c2} leads to kinks (change in slope) in the molecular (u) and atomic (Ψ) order parameter, later indicated by a black dot. Without loss of generality we chose \hat{n} axis (component of u) to lie along \mathbf{Q}_0 . The critical detunings are denoted by $\nu_{c1} = \nu_c^{\text{MSF}_{\text{fm}}-\text{AMSF}_{\text{fm}}}$, $\nu_{c2} = \nu_c^{\text{AMSF}_{\text{fm}}-\text{AMSF}_{\text{p}}}$, and $\nu_{c3} = \nu_c^{\text{AMSF}_{\text{p}}-\text{ASF}}$.

The behavior of these order parameters as a function of detuning, ν is illustrated in Fig. 2.9. With increasing detuning, the component v (being smaller than u) vanishes first, signaling a transition of the ferromagnetic AMSF_{fm} to the polar AMSF_p state. Depending on the value of other parameters, upon further increase of ν the system either continuously transitions at $\nu_c^{\text{AMSF}_{\text{p}}-\text{ASF}}$ to one of the three ASF states or undergoes a first-order AMSF_{fm}-ASF transition with u discontinuously jumping to zero when v vanishes. As we will discuss in Sec.2.5, on general grounds, beyond the mean-field approximation, we expect the transitions from such smectic-like superfluid phases

(AMSF_{p,fm}) to homogeneous and isotropic ASF states to be driven first-order by fluctuations.

The detuning phase boundaries corresponding to the MSF_{fm} - AMSF_{fm} and the AMSF_{fm} - AMSF_p transitions, determined by a vanishing of the atomic and the v (transverse to \mathbf{Q}_0) component of the molecular condensates, respectively, are given by

$$\nu_c^{\text{MSF}_{\text{fm}}-\text{AMSF}_{\text{fm}}} = - (g_1 - 2g_{am} + m\alpha^2/2) n_m, \quad (2.79)$$

$$\approx -\frac{1}{2} (g_1 - 2g_{am} + m\alpha^2/2) n, \quad (2.80)$$

$$\nu_c^{\text{AMSF}_{\text{fm}}-\text{AMSF}_{\text{p}}} = \frac{8\lambda g_2 + g_{am} (2m\alpha^2 - 4g_2) - m\alpha^2 (g_1 - g_2 + m\alpha^2)}{4g_2 + 2m\alpha^2} n_a. \quad (2.81)$$

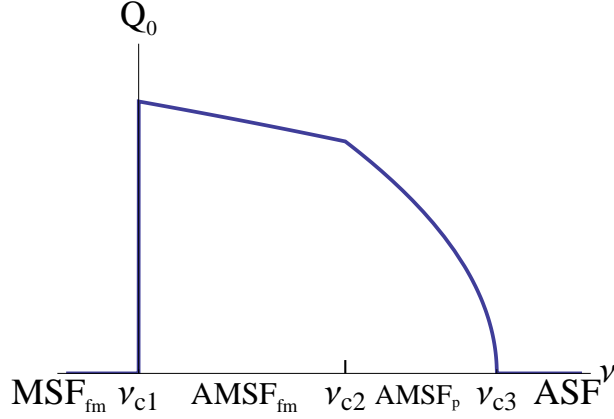


Figure 2.10: Schematic detuning dependence of the momentum \mathbf{Q}_0 of the atomic condensate starting with the ferromagnetic MSF_{fm}, with $\nu_{c1} = \nu_c^{\text{MSF}_{\text{fm}}-\text{AMSF}_{\text{fm}}}$, $\nu_{c2} = \nu_c^{\text{AMSF}_{\text{fm}}-\text{AMSF}_{\text{p}}}$, and $\nu_{c3} = \nu_c^{\text{AMSF}_{\text{p}}-\text{ASF}}$.

As with the polar state, the stability of the AMSF_{fm} is dictated by a condition on the interaction couplings, given by

$$4\lambda g_1 g_2 - 4g_2 g_{am} \tilde{g}_{am} - (g_1 + g_2)(m\alpha^2/2)^2 > 0. \quad (2.82)$$

In the opposite regime of $4\lambda g_1 g_2 - 4g_2 g_{am} \tilde{g}_{am} - (g_1 + g_2)(m\alpha^2/2)^2 < 0$ (Fig. 2.8 (b)), the AMSF_{fm} state is unstable, replaced by a direct first-order MSF_{fm}-ASF transition. The corresponding phase boundary is given by the degeneracy condition of the ASF and MSF_{fm} free-energies

$$f_{\text{asf}} = -\frac{\mu^2}{2\lambda} = -\frac{\mu_m^2}{g_1} = f_{\text{msf}_{\text{fm}}}. \quad (2.83)$$

2.4.4.3 Renormalized molecular interactions couplings

We conclude this section by noting that near a Feshbach resonance the microscopic pseudopotentials g_i, λ_i are modified by quantum fluctuations, replaced by corresponding experimentally determined scattering lengths. To lowest order (Born approximation, valid at low densities) in the FR coupling α , the diagrammatic corrections illustrated in Fig. 2.11 and Fig. 2.12 are given by

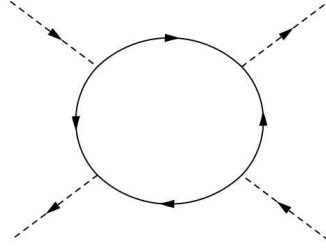


Figure 2.11: A lowest-order diagrammatic correction to molecular interaction coupling g_i .

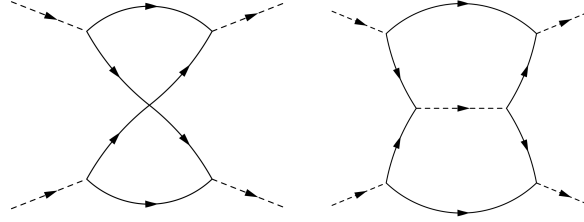


Figure 2.12: A next lowest-order diagrammatic corrections to molecular interaction couplings g_i .

$$\delta g_1^R = \frac{m^4 \alpha^4 \Lambda^2}{\pi^4} \left(-\frac{2\pi^2}{15m\Lambda} + \frac{a_{bg}}{9\pi} - \frac{m\alpha^2}{16}(0.468) \right), \quad (2.84)$$

$$\delta g_2^R = \frac{m^4 \alpha^4 \Lambda^2}{\pi^4} \left(-\frac{\pi^2}{15m\Lambda} - \frac{m\alpha^2}{16}(0.0489) \right), \quad (2.85)$$

where $a_{bg} = a_1 + a_2 + 2a_{12}$, the scattering lengths are defined by a standard relation, $\lambda_{\sigma\sigma'} = \frac{4\pi\hbar^2 a_{\sigma\sigma'}}{m}$, and $\Lambda \approx 2\pi/d$ is the ultra-violet cutoff set by the interatomic potential range. In the large Λ limit,

δg_i^R reduce to

$$\delta g_1^R \simeq \frac{m^4 \alpha^4 \Lambda^2}{\pi^4} \left(\frac{a_{bg}}{9\pi} - \frac{m\alpha^2}{16} (0.468) \right), \quad (2.86)$$

$$\delta g_2^R \simeq -\frac{m^5 \alpha^6 \Lambda^2}{(2\pi)^4} (0.0489). \quad (2.87)$$

This two-loop approximation (though valid only in the narrow Feshbach resonance limit), that finds $\delta g_2^R < 0$ suggests that in the broad-resonance limit it is the polar molecular phase, MSF_p that prevails.

More generally, the importance of these fluctuation corrections to molecular interactions, is that they provide a mechanism to tune and in principle even change the sign of the effective g_2 , thereby allowing a detuning-driven MSF_p - MSF_{fm} transition.

2.5 Elementary excitations

Having established the existence of a variety of superfluid ground states, we now turn our attention to the nature of low-energy excitations in each of these phases. As long as fluctuations remain finite for a range of system's parameters, the phases detailed in the previous section are self-consistently guaranteed to be stable in these regimes and to retain their qualitative form.

We study quantum fluctuations within each of the ASF, MSF and AMSF classes of phases established above. To this end we expand the atomic and molecular bosonic operators around their mean-field condensate values Ψ_σ, Φ ,

$$\psi_\sigma = \Psi_\sigma + \delta\psi_\sigma, \quad (2.88)$$

$$\phi_i = \Phi_i + \delta\phi_i, \quad (2.89)$$

where $\delta\psi_\sigma$ ($\sigma = 1, 2$) are fluctuation fields for atoms of flavors 1 and 2, respectively, and $\delta\phi_i$ ($i = x, y, z$) are triplet of the $\ell = 1$ molecular fluctuation fields.

For some of the analysis it is convenient to work in momentum space,

$$\delta\psi_\sigma = \frac{1}{\sqrt{V}} \sum_{\mathbf{k}} a_{\sigma,\mathbf{k}} e^{i\mathbf{k}\cdot\mathbf{r}}, \quad (2.90)$$

$$\delta\phi_i = \frac{1}{\sqrt{V}} \sum_{\mathbf{k}} b_{i,\mathbf{k}} e^{i\mathbf{k}\cdot\mathbf{r}}. \quad (2.91)$$

Using above momentum representation inside the Hamiltonian, Eq. (2.9), and expanding to second order in the fluctuations operators $a_{\sigma,\mathbf{k}}$, $b_{i,\mathbf{k}}$, we obtain $H = H_{\text{mft}}[\Psi_\sigma, \Phi] + H_f$, with

$$\begin{aligned} H_f = \sum_{\mathbf{k}} \left[\sum_{\sigma=1,2} \left(\frac{1}{2} \tilde{\varepsilon}_{\sigma,\mathbf{k}+\mathbf{Q}_\sigma} a_{\sigma,\mathbf{k}+\mathbf{Q}_\sigma}^\dagger a_{\sigma,\mathbf{k}+\mathbf{Q}_\sigma} + \tilde{\lambda}_\sigma a_{\sigma,-\mathbf{k}+\mathbf{Q}_\sigma} a_{\sigma,\mathbf{k}+\mathbf{Q}_\sigma} \right) \right. \\ + t_1 a_{1,\mathbf{k}+\mathbf{Q}}^\dagger a_{2,\mathbf{k}-\mathbf{Q}} + t_2 a_{2,\mathbf{k}+\mathbf{Q}} a_{1,\mathbf{k}+\mathbf{Q}} a_{2,-\mathbf{k}-\mathbf{Q}} \\ + \sum_{i=x,y,z} \left(\frac{1}{2} \tilde{\omega}_{i,\mathbf{k}} b_{i,\mathbf{k}}^\dagger b_{i,\mathbf{k}} + \delta_i b_{i,-\mathbf{k}} b_{i,\mathbf{k}} \right) + \frac{1}{2} \sum_{\substack{i,j=x,y,z \\ i \neq j}} \left(g_{ij} b_{j,\mathbf{k}}^\dagger b_{i,\mathbf{k}} + \gamma_{ij} b_{i,-\mathbf{k}} b_{j,\mathbf{k}} \right) \\ \left. - \sum_{\sigma} \boldsymbol{\alpha}_{\bar{\sigma},\mathbf{k}} \cdot \mathbf{b}_{\mathbf{k}}^\dagger a_{\sigma,\mathbf{k}+\mathbf{Q}_\sigma} + h.c. \right], \quad (2.92) \end{aligned}$$

$$\equiv \sum_{\mathbf{k},\alpha,\beta} c_{\alpha,\mathbf{k}}^\dagger \tilde{h}_{\mathbf{k}}^{\alpha\beta} c_{\beta,\mathbf{k}} \quad (2.93)$$

where $\tilde{h}_{\mathbf{k}}^{\alpha\beta}$ is a Bogoliubov Hamiltonian matrix defined by matrix elements

$$\tilde{\varepsilon}_{\sigma,\mathbf{k}} = \epsilon_{\mathbf{k}} - \mu_\sigma + 2\lambda_\sigma |\Psi_\sigma|^2 + \lambda_{12} |\Psi_{\bar{\sigma}}|^2 + g_{am} |\Phi|^2, \quad (2.94)$$

$$\tilde{\omega}_{i,\mathbf{k}} = \frac{1}{2} \epsilon_{\mathbf{k}} - \mu_m + g_1 |\Phi|^2 + (g_1 + 2g_2) |\Phi_i|^2 + g_{am} (|\Psi_1|^2 + |\Psi_2|^2), \quad (2.95)$$

$$\tilde{\lambda}_\sigma = \frac{1}{2} \lambda_\sigma \Psi_\sigma^{*2}, \quad (2.96)$$

$$t_1 = \lambda_{12} \Psi_1 \Psi_2^*, \quad (2.97)$$

$$t_{2,\mathbf{k}} = \lambda_{12} \Psi_1^* \Psi_2^* - \alpha \Phi^* \cdot \mathbf{k}, \quad (2.98)$$

$$\delta_i = \frac{1}{2} g_1 \Phi_i^* \Phi_i^* + \frac{1}{2} g_2 \Phi^* \cdot \Phi^*, \quad (2.99)$$

$$g_{ij} = g_1 \Phi_i^* \Phi_j + 2g_2 \Phi_i^* \Phi_j, \quad (2.100)$$

$$\gamma_{ij} = \frac{1}{2} g_1 \Phi_i^* \Phi_j^*, \quad (2.101)$$

$$\boldsymbol{\alpha}_{\sigma=(1,2),\mathbf{k}} = \pm \alpha \Psi_{\sigma,\mathbf{Q}_\sigma} (\mathbf{Q}_\sigma - \mathbf{k}/2), \quad (2.102)$$

$\epsilon_{\mathbf{k}} = \frac{k^2}{2m}$, $\bar{1} = 2, \bar{2} = 1$, and we suppressed the \mathbf{Q} subscript on the atomic condensate order

parameter, $\Psi_{\sigma, \mathbf{Q}}$. The ten-dimensional bosonic Nambu spinor $c_{\alpha, \mathbf{k}}$ is given by

$$c_{\alpha, \mathbf{k}} \equiv \left(a_{\sigma, \mathbf{k} + \mathbf{Q}_{\sigma}}, b_{i, \mathbf{k}}, a_{\sigma, -\mathbf{k} + \mathbf{Q}_{\sigma}}^{\dagger}, b_{i, -\mathbf{k}}^{\dagger} \right). \quad (2.103)$$

A diagonalization of this ten-dimensional Bogoliubov Hamiltonian, preserving bosonic commutation relations of the $c_{\alpha, \mathbf{k}}$ components gives the spectrum of the 5 modes throughout the phase diagram. This can be done numerically, but is not very enlightening. Instead, we will study the problem one phase at a time, which allows a significantly more revealing solution of the problem.

2.5.1 ASF phases

In the simplest limit of a large positive detuning, $\nu > \nu^{\text{AMSF-ASF}}$ the molecules are gapped, one or both species of the atoms are condensed at zero momentum, $\mathbf{Q} = 0$, and the system is in the ASF phases. As discussed in Sec. 2.3, these are conventional well-studied superfluids, characterized by one Bogoliubov mode for each of the atomic $U(1)$ symmetry that is broken. In the ASF phases $\Phi = 0$, the three molecular modes are gapped and can therefore be integrated out (adiabatically eliminated). Away from the transition, this leads to only a small renormalization (that we will neglect) of effective parameters in the resulting H_f . From Eq.(2.92) the atomic sector of the Bogoliubov Hamiltonian is then given by

$$H_f^{\text{ASF}\sigma} = \sum_{\mathbf{k}} \left[\sum_{\sigma=1,2} \left(\frac{1}{2} \tilde{\varepsilon}_{\sigma, \mathbf{k}} a_{\sigma, \mathbf{k}}^{\dagger} a_{\sigma, \mathbf{k}} + \tilde{\lambda}_{\sigma} a_{\sigma, -\mathbf{k}} a_{\sigma, \mathbf{k}} \right) + t_{1, \mathbf{k}} a_{\sigma, \mathbf{k}}^{\dagger} a_{\bar{\sigma}, \mathbf{k}} + t_{2, \mathbf{k}} a_{\sigma, -\mathbf{k}} a_{\bar{\sigma}, \mathbf{k}} \right] + h.c.. \quad (2.104)$$

2.5.1.1 ASF $_{\sigma}$: single atomic species BEC

In the regime where only a single atomic species of $\psi_{1,2}$ condenses (i.e., $\Psi_{\sigma} \neq 0, \Psi_{\bar{\sigma}} = 0$), the system is in an ASF $_{\sigma}$ phase. Standard analysis then leads to a conventional, gapless atomic Bogoliubov sound mode for species σ

$$E_{k\sigma}^{(a)} = \sqrt{\frac{k^2}{2m} \left(\frac{k^2}{2m} + \lambda_{\sigma} n \right)}, \quad (2.105)$$

$$\approx c_a k, \quad (2.106)$$

with $c_a \approx \sqrt{\frac{\lambda_\sigma n}{2m}}$, and a gapped atomic mode for the complementary atomic species $\bar{\sigma}$:

$$E_{k\bar{\sigma}}^{(a)} \simeq \frac{k^2}{2m_{\pm}^*} - \mu_{\bar{\sigma}} + \lambda_{12} \frac{n}{2} \quad (2.107)$$

where $\frac{n}{2} \simeq n_1 = n_2$ for a balanced case. Above, the coupling parameters are those from Eq. (2.29), with $\Phi = \Psi_{\bar{\sigma}} = 0$, and m_{\pm}^* are effective atomic masses renormalized by interaction

$$\frac{1}{m_{+}^*} = \frac{1}{m} + \frac{3n\alpha^2}{2(\nu - \lambda n + \frac{g_{am}}{2}n)}, \quad (2.108)$$

$$\frac{1}{m_{-}^*} = \frac{1}{m} - \frac{3n\alpha^2}{4(\nu - \lambda n + \frac{g_{am}}{2}n)}. \quad (2.109)$$

The remaining three molecular-like modes (corrected by coupling to atoms) are gapped and in a $k \rightarrow 0$ limit are given by

$$E_{k1}^{(m)} = E_{k2}^{(m)} = \frac{k^2}{4m} + \nu - \frac{\lambda_\sigma}{2}n + \frac{g_{am}}{2}n - \mu_{\bar{\sigma}}, \quad (2.110)$$

$$E_{k3}^{(m)} \simeq \frac{k^2}{4m_{+}^*} + \nu - \frac{\lambda_\sigma}{2}n + \frac{g_{am}}{2}n - \mu_{\bar{\sigma}}. \quad (2.111)$$

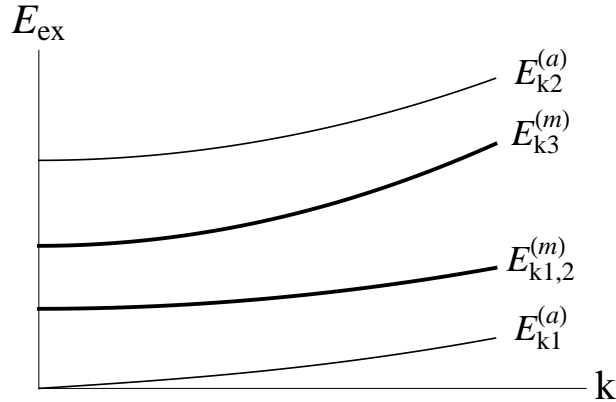


Figure 2.13: Schematic ASF single BEC (ASF_σ) excitation spectrum. The lowest curve is the atomic Bogoliubov mode and the upper curves are gapped atomic (thin) and molecular (thick) modes.

2.5.1.2 ASF_{12} : double atomic species BEC

In the regime where both atomic species of $\psi_{1,2}$ condense, i.e., $\Psi_{1,2} \neq 0$, the system is in a two-species ASF_{12} phase. Standard analysis, consistent with two $U(1)$ symmetries spontaneously

broken, then leads to two gapless atomic Bogoliubov sound modes for species 1 and 2. Together with the gapped molecular excitations this leads to spectra of the five modes:

$$E_{k1}^{(a_{12})} = \sqrt{\frac{k^2}{2m} \left(\frac{k^2}{2m} + 2\lambda n \right)}, \quad (2.112)$$

$$E_{k2}^{(a_{12})} \simeq c^{(a_{12})} k, \quad (2.113)$$

$$E_{k1}^{(m_{12})} = E_{k2}^{(m_{12})} = \frac{k^2}{4m} + \nu - 2\lambda n + g_{am} n, \quad (2.114)$$

$$E_{k3}^{(m_{12})} \simeq \frac{k^2}{4m^*} + \nu - 2\lambda n + g_{am} n, \quad (2.115)$$

where for $E_{k2}^{(a_{12})}$ and $E_{k3}^{(m_{12})}$ we took $k \rightarrow 0$ and $\alpha \rightarrow 0$ limit, and defined the sound velocity and effective atomic mass

$$c^{(a_{12})} = \sqrt{\frac{(\lambda - \lambda_{12})n}{m} - \frac{3n\alpha^2 \sqrt{(\lambda - \lambda_{12})mn}}{4(\nu - 2\lambda n + g_{am}n)}}, \quad (2.116)$$

$$\frac{1}{m^*} = \frac{1}{m} + \frac{3(\nu - (\lambda + \lambda_{12})n + g_{am}n)n\alpha^2}{(\nu - 2\lambda n + g_{am}n)^2}. \quad (2.117)$$

$E_{k1}^{(a_{12})}$ and $E_{k2}^{(a_{12})}$ are atom-like, gapless, in-phase and out-of-phase modes, respectively. $E_{k2}^{(a_{12})}$ and $E_{k3}^{(m_{12})}$ are modified by the FR interaction between atoms and molecules. The ASF-AMSF phase boundary is determined by the point where the molecular gap

$$E_{\text{gap}}^{\text{ASF}} = \nu - 2\lambda n + g_{am} n \quad (2.118)$$

closes, and is consistent with the critical detuning determined by the development of the molecular order parameter that we found in Sec. 2.4.

2.5.2 MSF phases

In the opposite limit of a large negative detuning, $\nu < \nu^{\text{MSF-AMSF}}$ both atomic species are gapped, $\Psi_\sigma = 0$, and p -wave molecules are condensed into one of the two ($\ell = 1$) $\ell_z = 0$ polar (MSF_p) and $\ell_z = \pm 1$ ferromagnetic (MSF_{fm}) molecular superfluids, isomorphic to spinor-1 condensates with well-studied properties [84, 89, 91]. To see this, we note that the atomic Bogoliubov excitations are gapped and can therefore be integrated out. Away from the transition, they lead to only a small renormalization of effective parameters. Neglecting these small effects,

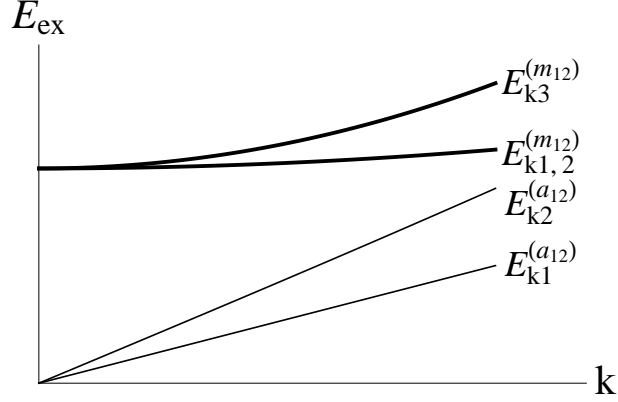


Figure 2.14: Schematic ASF double BEC (ASF_{12}) excitation spectrum. There are two gapless atomic Bogoliubov modes (thin) as well as three gapped molecular modes (thick).

the vanishing of $\alpha_{\sigma,\mathbf{k}} = \pm\alpha\Psi_{\sigma,\mathbf{Q}_\sigma}(\mathbf{Q}_\sigma - \mathbf{k}/2) = 0$ decouples the Hamiltonian, $H_f = H_a + H_m$ into atomic and molecular parts, that then are straightforwardly diagonalized.

The atomic sector, H_a is of standard Bogoliubov form, simplified to a 2×2 form by $t_1 = \tilde{\lambda}_\sigma = 0$ inside the MSF phases, leading to the atomic excitation spectrum, that for the symmetric case of $\mu_1 = \mu_2 \equiv \mu$ is given by

$$E_{a,\mathbf{k}}^{\text{MSF}} = \sqrt{(\tilde{\varepsilon}_{\mathbf{k}} + |\alpha\Phi \cdot \mathbf{k}|)(\tilde{\varepsilon}_{\mathbf{k}} - |\alpha\Phi \cdot \mathbf{k}|)}, \quad (2.119)$$

where $\tilde{\varepsilon}_{\mathbf{k}} = k^2/2m - \mu + g_{am}|\Phi|^2$.

One key observation is that already inside the MSF phases the atomic spectrum, $E_{a,\mathbf{k}}^{\text{MSF}}$ (degenerate for $\sigma = 1, 2$ species) develops a minimum at a nonzero momentum $\mathbf{k}_{\min} = \mathbf{Q}_{p,\text{fm}}$, with the corresponding atomic gap minimum, $E_{a,\text{gap}}^{\text{MSF}_{p,\text{fm}}}$ given by a value dependent on the nature of the $\text{MSF}_{p,\text{fm}}$ phase.

2.5.2.1 Polar MSF_p state : $g_2 < 0$

As analyzed in Sec. 2.4, the polar MSF_p phase is defined by a molecular condensate order parameter, that can be taken to be a three-dimensional real vector, $\Phi = \mathbf{u} = \Phi_p \hat{\mathbf{n}}$, with $n_m = |\Phi_p|^2$. In terms of the molecular condensate density $n_m \approx n/2$ the atomic chemical potential for the

symmetric case, $\mu_1 = \mu_2 = \mu$ is given by

$$\mu = \frac{1}{2}(\mu_m + \nu) = \frac{1}{2}((g_1 + g_2)n_m + \nu), \quad (2.120)$$

controlled by the FR detuning, ν .

For this symmetric case $\mu_1 = \mu_2 = \mu$ (easily generalizable for the asymmetric, imbalanced case), the atomic spectrum minimum is characterized by

$$\begin{aligned} k_{\min} &= Q_p, \\ &= \alpha m \sqrt{n_m}, \end{aligned} \quad (2.121)$$

$$E_{\text{gap}}^{(\text{MSF}_p, \text{a})} = -\mu + g_{am}n_m - \frac{m\alpha^2 n_m}{2}, \quad (2.122)$$

where in an isotropic trap the orientation of \mathbf{k}_{\min} is spontaneously chosen. The MSF_p - AMSF_p phase transition boundary is set by the closing of this atomic gap, and is given by

$$\nu_c^{\text{MSF}_p\text{-AMSF}_p} = -(g_1 + g_2 - 2g_{am} + m\alpha^2) n_m. \quad (2.123)$$

Reassuringly, this is identical to the critical detuning for this phase boundary, that we obtained in Sec. 2.4 from the value of detuning at which the finite-momentum atomic order-parameter became nonzero.

The diagonalization of molecular part H_m is also straightforward, and is identical to the case of the spinor-1 condensates [84, 89, 91], with effective parameters of our physically distinct, p -wave resonant scalar Bose gas. Substituting characteristics of the polar phase MSF_p (order parameters, μ , $\mu_m \approx (g_1 + g_2)n_m$, $g_2 < 0$, etc. from above) into H_m , we obtain

$$\begin{aligned} H_m^{\text{MSF}_p} = \sum_{\mathbf{k}} & \left[\left(\frac{1}{2}\epsilon_{\mathbf{k}} + (g_1 + g_2)n_m \right) b_{\parallel, \mathbf{k}}^\dagger b_{\parallel, \mathbf{k}} + \left(\frac{1}{2}\epsilon_{\mathbf{k}} + |g_2|n_m \right) \mathbf{b}_{\perp, \mathbf{k}}^\dagger \cdot \mathbf{b}_{\perp, \mathbf{k}} \right. \\ & \left. + \left(\frac{1}{2}(g_1 + g_2)n_m b_{\parallel, -\mathbf{k}} b_{\parallel, \mathbf{k}} + \frac{1}{2}g_2 n_m \mathbf{b}_{\perp, -\mathbf{k}} \cdot \mathbf{b}_{\perp, \mathbf{k}} + h.c. \right) \right], \end{aligned} \quad (2.124)$$

where $\mathbf{b}_{\perp, \mathbf{k}}$ are two degenerate transverse (to \mathbf{Q}_p) molecular modes. This leads to three Bogoliubov

type dispersions,

$$E_{\parallel,k}^{\text{MSF}_p} = \frac{1}{2} \sqrt{\epsilon_{\mathbf{k}}^2 + 4(g_1 + g_2)n_m \epsilon_{\mathbf{k}}}, \quad (2.125)$$

$$\simeq \sqrt{\frac{(g_1 + g_2)n_m}{2m}} k, \quad (2.126)$$

$$E_{\perp,k}^{\text{MSF}_p} = \frac{1}{2} \sqrt{\epsilon_{\mathbf{k}}^2 + 4|g_2|n_m \epsilon_{\mathbf{k}}}, \quad (2.127)$$

$$\simeq \sqrt{\frac{|g_2|n_m}{2m}} k, \quad (2.128)$$

where the longitudinal mode, $E_{\parallel,k}^{\text{MSF}_p}$ describes the conventional molecular superfluid phase fluctuations and the doubly-degenerate transverse mode, $E_{\perp,k}^{\text{MSF}_p}$ is the dispersion for the $\ell = 1$ molecular orientational spin-waves. From the second set of $k \rightarrow 0$ expressions we read off the corresponding phase and spin-wave velocities, given by

$$c_{\parallel}^{\text{MSF}_p} = \sqrt{\frac{(g_1 + g_2)n_m}{2m}}, \quad (2.129)$$

$$c_{\perp}^{\text{MSF}_p} = \sqrt{\frac{|g_2|n_m}{2m}}. \quad (2.130)$$

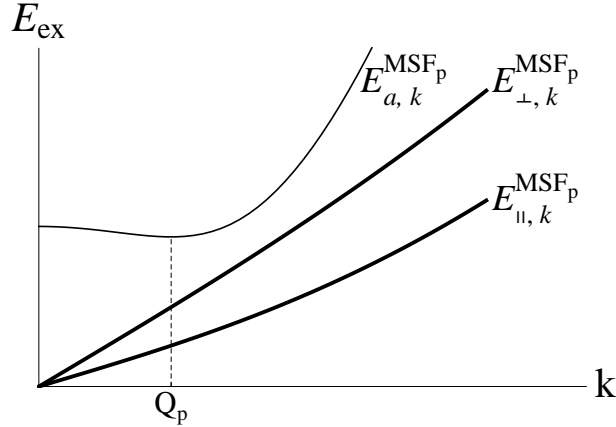


Figure 2.15: Schematic excitation spectrum for the polar molecular superfluid, MSF_p . The doubly-degenerate atomic spectrum (upper thin curve) exhibits a minimum gap at nonzero k , a precursor of finite momentum atomic condensation inside the AMSF_p . The molecular spectra (thick curves), one longitudinal (lowest) and two degenerate transverse (middle) modes are of Bogoliubov type.

2.5.2.2 Ferromagnetic MSF_{fm} state : $g_2 > 0$

Inside the ferromagnetic MSF_{fm} state, the molecular condensate order parameter is given by $\Phi = \frac{\Phi_{\text{fm}}}{\sqrt{2}}(\hat{\mathbf{n}} + i\hat{\mathbf{m}})$, expressed in terms of an orthonormal triad, $\hat{\mathbf{n}} \times \hat{\mathbf{m}} = \hat{\ell}$. From the earlier mean-field analysis, the molecular condensate density is given by $n_m = |\Phi|^2 = \mu_m/g_1$, leading for the symmetric case, $\mu_1 = \mu_2 = \mu$

$$\mu = \frac{1}{2}(g_1 n_m + \nu). \quad (2.131)$$

To lowest order, the atomic spectrum inside MSF_{fm} has identical structure as that of the MSF_p state, Eq.(2.5.2.1), but with the replacement $g_1 + g_2 \rightarrow g_1$ and $\alpha^2 \rightarrow \alpha^2/2$.

$$\begin{aligned} k_{\min} &= Q_{\text{fm}}, \\ &= \frac{1}{\sqrt{2}}\alpha m \sqrt{n_m}, \end{aligned} \quad (2.132)$$

$$E_{\text{gap}}^{(\text{MSF}_{\text{fm}}, \text{a})} = -\mu + g_{\text{am}} n_m - \frac{m\alpha^2 n_m}{4}. \quad (2.133)$$

The MSF_{fm}-AMSF_{fm} phase transition boundary is determined by the vanishing of the atomic gap, and is given by

$$\nu_c^{\text{MSF}_{\text{fm}}-\text{AMSF}_{\text{fm}}} = -\left(g_1 - 2g_{\text{am}} + \frac{1}{2}m\alpha^2\right)n_m, \quad (2.134)$$

identical to the critical detuning obtained from mean-field theory for the order parameter in Sec. 2.4.

Using above parameters characteristic of the ferromagnetic phase MSF_{fm} inside H_m , the molecular sector of the Hamiltonian reduces to

$$\begin{aligned} H_m^{\text{MSF}_{\text{fm}}} &= \sum_{\mathbf{k}} \left[\left(\frac{1}{2}\epsilon_{\mathbf{k}} + 2g_2 n_m\right) b_{+, \mathbf{k}}^\dagger b_{+, \mathbf{k}} + \left(\frac{1}{2}\epsilon_{\mathbf{k}} + g_1 n_m\right) b_{-, \mathbf{k}}^\dagger b_{-, \mathbf{k}} + \frac{1}{2}\epsilon_{\mathbf{k}} b_{z, \mathbf{k}}^\dagger b_{z, \mathbf{k}} \right. \\ &\quad \left. + \frac{1}{2}g_1 n_m b_{-, \mathbf{k}} b_{-, \mathbf{k}} + \frac{1}{2}g_1 n_m b_{-, \mathbf{k}}^\dagger b_{-, \mathbf{k}}^\dagger \right], \end{aligned} \quad (2.135)$$

where

$$b_+ = \frac{1}{\sqrt{2}}(b_n + ib_m), \quad (2.136)$$

$$b_- = \frac{1}{\sqrt{2}}(b_n - ib_m), \quad (2.137)$$

are expressed in terms of operators b_n , b_m , that are components of \mathbf{b} along $\hat{\mathbf{n}}$, $\hat{\mathbf{m}}$, respectively.

Diagonalization of above Hamiltonian then gives the following spectrum

$$E_{z,k}^{\text{MSF}_{\text{fm}}} = \frac{1}{2}\epsilon_{\mathbf{k}} = \frac{k^2}{4m}, \quad (2.138)$$

$$E_{+,k}^{\text{MSF}_{\text{fm}}} = \frac{1}{2}\epsilon_{\mathbf{k}} + 2g_2n_m, \quad (2.139)$$

$$E_{-,k}^{\text{MSF}_{\text{fm}}} = \frac{1}{2}\sqrt{\epsilon_{\mathbf{k}}^2 + 4g_1n_m\epsilon_{\mathbf{k}}}, \quad (2.140)$$

$$\simeq \sqrt{\frac{g_1n_m}{2m}}k, \quad (2.141)$$

where the Bogoliubov sound speed is given by $c_{\text{MSF}_{\text{fm}}} = \sqrt{g_1n_m/2m}$.

We note that despite a three-dimensional coset space, $SO(3)$ characterizing MSF_{fm} , only *two* modes (linear and quadratic in k) exhibit a spectrum that vanishes in $k \rightarrow 0$ limit. The spectrum $E_{-,k}^{\text{MSF}_{\text{fm}}}$, is that of a conventional Bogoliubov superfluid phase, here associated with the $U(1)$ broken gauge symmetry of the molecular condensate. The quadratic in k gapless spectrum is that of the ferromagnetic spin-waves, where the two components of the spinor are canonically conjugate and as a result combine into a single low-frequency mode.

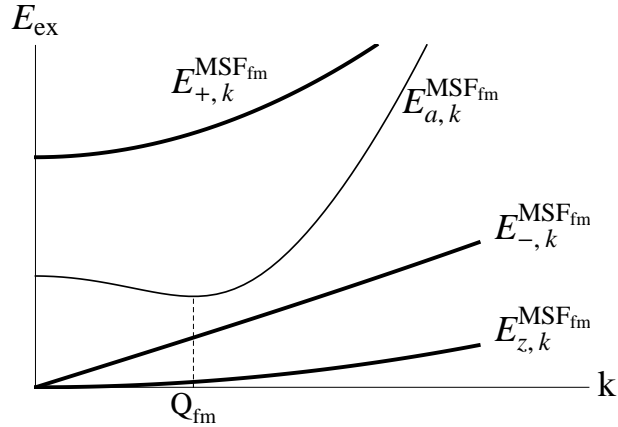


Figure 2.16: Schematic Excitation spectrum for the ferromagnetic molecular superfluid, MSF_{fm} . The doubly-degenerate atomic spectrum (thin curves) exhibits a minimum gap at nonzero k , a precursor of finite momentum atomic condensation. The molecular spectrum (thick curves), consists of a longitudinal gapless quadratic ferromagnetic spin-wave mode (lowest), a Bogoliubov sound mode and a quadratic gapped mode.

2.5.3 AMSF phases

To obtain the spectrum inside the AMSF phases requires a solution of the fully general Hamiltonian, H_f , Eq. (2.92). Because in this superfluid state all atomic and molecular modes are coupled, a direct BdG analysis generically involves a diagonalization of a 10×10 Bogoliubov matrix. This can be done numerically. However, instead, below we take a complementary coherent-state path-integral approach, that allows us to obtain the modes and dispersions analytically, leading to more insight into their structure. Using the formulation of the problem introduced in Sec. 2.2.0.2, we analyze the low-energy fluctuations in the AMSF states using the coherent-state Lagrangian density, $\mathcal{L}[\psi_\sigma, \phi] = \mathcal{L}_{\text{MFT}}[\Psi_\sigma, \Phi] + \delta\mathcal{L}$, Eq. (2.2.0.2), where $\mathcal{L}_{\text{MFT}}[\Psi_\sigma, \Phi]$ is the mean-field Lagrangian defining the AMSF phase and $\delta\mathcal{L}$ is the Lagrangian density of the quadratic fluctuations. To obtain $\delta\mathcal{L}$ we expand the atomic and molecular bosonic fields ψ_σ, ϕ about their mean-field values (for clarity of notation in this section we choose to use ρ instead of n of the previous sections, where $\rho_\sigma = n_a/2$, $\rho_m = n_m$, and $\rho_s = n$)

$$\psi_\sigma = \sqrt{\rho_\sigma} e^{i\theta_\sigma + i\mathbf{Q}_\sigma \cdot \mathbf{r}}, \quad (2.142)$$

$$\phi = \sqrt{\rho_m} \hat{\phi} e^{i\varphi}, \quad (2.143)$$

where $\mathbf{Q}_\sigma = \pm\mathbf{Q}$ for $\sigma = 1, 2$, respectively, $\rho_m = \rho_{m0} + \delta\rho_m$ and $\rho_\sigma = \rho_0 + \delta\rho_\sigma$ are the molecular and atomic densities, with the mean-field values $\rho_{m0} = |\Phi|^2$, $\rho_0 = |\Psi_\sigma|^2$, and, based on Eq. (2.60) with latter σ -independent in the AMSF phase. In addition to the density fluctuations $\delta\rho_m, \delta\rho_\sigma$, and two atomic and one molecular superfluid phases, θ_σ, φ , the molecular Goldstone modes are characterized by a unit-vector $\hat{\phi}$, whose form depends on the polar or ferromagnetic nature of the AMSF state

$$\hat{\phi} = \hat{\mathbf{n}}, \quad \text{for polar AMSF}_p, \quad (2.144)$$

$$= \frac{1}{\sqrt{2}}(\hat{\mathbf{n}} + i\hat{\mathbf{m}}), \quad \text{for ferromagnetic AMSF}_{\text{fm}}. \quad (2.145)$$

Substituting these parametrizations of the atomic and molecular fields into the Lagrangian, Eq. (2.28), we obtain $\delta\mathcal{L}$ that controls fluctuations in the AMSF phases.

2.5.3.1 polar AMSF_p

Focusing first on the polar state, with $\phi = \sqrt{\rho_m}\hat{\mathbf{n}}e^{i\varphi}$, we find

$$\begin{aligned}
\delta\mathcal{L}_p &= \rho_\sigma(i\partial_\tau\theta_\sigma - \mu_\sigma) + \frac{\rho_\sigma}{2m}(\nabla\theta_\sigma + \mathbf{Q}_\sigma)^2 + \rho_m(i\partial_\tau\varphi - \mu_m) + \frac{\rho_m}{4m}(\nabla\varphi)^2 + \frac{\rho_m}{4m}(\nabla\hat{\mathbf{n}})^2 \\
&- \alpha\sqrt{\rho_m\rho_1\rho_2}\hat{\mathbf{n}} \cdot (\nabla\theta_1 - \nabla\theta_2 + 2\mathbf{Q}) \cos(\varphi - \theta_1 - \theta_2) + \frac{1}{8m\rho_\sigma}(\nabla\rho_\sigma)^2 + \frac{1}{16m\rho_m}(\nabla\rho_m)^2 + \frac{\lambda_\sigma}{2}\rho_\sigma^2 \\
&+ \lambda_{12}\rho_1\rho_2 + g_{am}(\rho_1 + \rho_2)\rho_m + \frac{g}{2}\rho_m^2 - \mathcal{L}_{\text{MFT}}[\rho_0, \rho_{m0}, \hat{\mathbf{n}}_0, \mathbf{Q}], \tag{2.146} \\
&= i\delta\rho_+\partial_\tau\theta_+ + \frac{\rho_0}{m}(\nabla\theta_+)^2 + i\delta\rho_-\partial_\tau\theta_- + \frac{\rho_0}{m}(\nabla\theta_- + \mathbf{Q})^2 + i\delta\rho_m\partial_\tau\varphi + \frac{\rho_{m0}}{4m}(\nabla\varphi)^2 + \frac{\rho_{m0}}{4m}(\nabla\hat{\mathbf{n}})^2 \\
&- 2\alpha\rho_0\sqrt{\rho_{m0}}\hat{\mathbf{n}} \cdot (\nabla\theta_- + \mathbf{Q}) \cos(\varphi - 2\theta_+) \\
&+ \frac{1}{16m\rho_0}(\nabla\rho_+)^2 + \frac{1}{16m\rho_0}(\nabla\rho_-)^2 + \frac{1}{16m\rho_{m0}}(\nabla\rho_m)^2 + \frac{\lambda}{4}\delta\rho_+^2 + \frac{\lambda}{4}\delta\rho_-^2 + \frac{\lambda_{12}}{4}(\delta\rho_+^2 - \delta\rho_-^2) \\
&+ g_{am}\delta\rho_+\delta\rho_m + \frac{g}{2}\delta\rho_m^2, \tag{2.147}
\end{aligned}$$

where $g \equiv g_1 + g_2$, $\lambda = \lambda_1 = \lambda_2$ for simplicity, and

$$\theta_\pm = \frac{1}{2}(\theta_1 \pm \theta_2), \tag{2.148}$$

$$\delta\rho_\pm = \delta\rho_1 \pm \delta\rho_2, \tag{2.149}$$

$$\mu = \frac{1}{2}(\mu_1 + \mu_2), \tag{2.150}$$

$$h = \frac{1}{2}(\mu_1 - \mu_2), \tag{2.151}$$

$$\mathbf{Q} = \alpha m \sqrt{\rho_{m0}} \hat{\mathbf{n}}_0. \tag{2.152}$$

In the second form, Eq. (2.147), we expanded the Lagrangian about its mean-field value \mathcal{L}_{MFT} to quadratic order in fluctuations, $\theta_\sigma, \varphi, \delta\rho_\sigma, \delta\rho_m$, and neglected the constant and subdominant contributions, that are negligible at long scales and low energies. We note that as usual, the linear terms in $\delta\mathcal{L}_p$, Eq. (2.147) vanish identically, enforced by the saddle-point equations for the condensates, ρ_{-0}, ρ_{m0} , and \mathbf{Q} .

Examining the last form of $\delta\mathcal{L}_p$, it is clear that important simplifications take place at long scales. In particular, the Feshbach resonant (Josephson-like) coupling, $-\alpha \cos(\varphi - 2\theta_+)$ between the closed-channel molecules and atoms (that is always relevant in three dimensions and therefore acts like a ‘‘mass’’) locks their phases together, at low energies giving:

$$\varphi = 2\theta_+. \quad (2.153)$$

Integrating φ out and completing the square for the $\nabla\theta_- + \mathbf{Q}$ and $\hat{\mathbf{n}}$, to lowest order then gives

$$\begin{aligned} \delta\mathcal{L}_p = & i(\delta\rho_+ + 2\delta\rho_m)\partial_\tau\theta_+ + \frac{\rho_{s0}}{m}(\nabla\theta_+)^2 + i\delta\rho_-\partial_\tau\theta_- + \frac{\rho_0}{m}(\nabla\theta_- + \mathbf{Q} - \alpha m\sqrt{\rho_{m0}}\hat{\mathbf{n}})^2 + \frac{\rho_{m0}}{4m}(\nabla\hat{\mathbf{n}})^2 \\ & + \frac{1}{16m\rho_0}(\nabla\rho_+)^2 + \frac{1}{16m\rho_0}(\nabla\rho_-)^2 + \frac{1}{16m\rho_{m0}}(\nabla\rho_m)^2 + \frac{\lambda}{4}\delta\rho_+^2 + \frac{\lambda}{4}\delta\rho_-^2 + \frac{\lambda_{12}}{4}(\delta\rho_+^2 - \delta\rho_-^2) \\ & + g_{am}\delta\rho_+\delta\rho_m + \frac{g}{2}\delta\rho_m^2, \end{aligned} \quad (2.154)$$

$$\begin{aligned} = & i(\delta\rho_+ + 2\delta\rho_m)\partial_\tau\theta_+ + \frac{\rho_{s0}}{m}(\nabla\theta_+)^2 + i\delta\rho_-\partial_\tau\theta_- + \frac{\rho_0}{m}(\nabla\theta_- - \alpha m\sqrt{\rho_{m0}}\delta\hat{\mathbf{n}})^2 + \frac{\rho_{m0}}{4m}(\nabla\hat{\mathbf{n}})^2 \\ & + \frac{1}{16m\rho_0}(\nabla\rho_+)^2 + \frac{1}{16m\rho_0}(\nabla\rho_-)^2 + \frac{1}{16m\rho_{m0}}(\nabla\rho_m)^2 + \frac{\lambda}{4}\delta\rho_+^2 + \frac{\lambda}{4}\delta\rho_-^2 + \frac{\lambda_{12}}{4}(\delta\rho_+^2 - \delta\rho_-^2) \\ & + g_{am}\delta\rho_+\delta\rho_m + \frac{g}{2}\delta\rho_m^2, \end{aligned} \quad (2.155)$$

$$\begin{aligned} = & i(\delta\rho_+ + 2\delta\rho_m)\partial_\tau\theta_+ + \frac{\rho_{s0}}{m}(\nabla\theta_+)^2 + i\delta\rho_-\partial_\tau\theta_- + \frac{\rho_0}{m}(\partial_z\theta_-)^2 + \frac{1}{4m^3\alpha^2}(\nabla\nabla_\perp\theta_-)^2 \\ & + \frac{1}{16m\rho_0}(\nabla\rho_+)^2 + \frac{1}{16m\rho_0}(\nabla\rho_-)^2 + \frac{1}{16m\rho_{m0}}(\nabla\rho_m)^2 + \frac{\lambda}{4}\delta\rho_+^2 + \frac{\lambda}{4}\delta\rho_-^2 + \frac{\lambda_{12}}{4}(\delta\rho_+^2 - \delta\rho_-^2) \\ & + g_{am}\delta\rho_+\delta\rho_m + \frac{g}{2}\delta\rho_m^2, \end{aligned} \quad (2.156)$$

where

$$\rho_{s0} = \rho_0 + \rho_{m0}, \quad (2.157)$$

$$\hat{\mathbf{z}} = \hat{\mathbf{Q}}, \quad (2.158)$$

and in the second form, Eq. (2.155) we used the minimum value of \mathbf{Q} , Eq. (2.152) characterizing the AMSF_p phase, that leads to a minimal-like coupling between $\nabla\theta_-$ and $\delta\hat{\mathbf{n}}$, latter transverse (\perp) to $\hat{\mathbf{n}}_0$ and \mathbf{Q} . Subsequently, to obtain our final expression, we integrated out $\delta\hat{\mathbf{n}}$, that to lowest

order via a Higgs-like mechanism introduced a low-energy constraint

$$\delta\hat{\mathbf{n}} = \frac{1}{\alpha m \sqrt{\rho_{m0}}} \nabla_{\perp} \theta_{-}, \quad (2.159)$$

$$= \frac{1}{Q} \nabla_{\perp} \theta_{-}. \quad (2.160)$$

Using it inside the $(\nabla\hat{\mathbf{n}})^2$ term, then leads to a quantum smectic-like “elasticity” for the θ_{-} Goldstone mode, with $\hat{\mathbf{z}}$ chosen to lie along \mathbf{Q} , i.e., $\hat{\mathbf{z}} = \hat{\mathbf{Q}}$. This smectic dispersion is expected based on the underlying rotational symmetry, that is spontaneously broken by the periodic AMSF_p state. It is closely related to other periodic superfluids, such as, for example the Fulde-Ferrell-Larkin-Ovchinnikov pair-density wave states [8, 9, 109, 110].

As a final step we now integrate out the densities $\delta\rho_{\pm}$ fluctuations, obtaining at long scales (where $\nabla\rho_{\pm}$ can be neglected) our final form for the Goldstone mode Lagrangian in the AMSF_p state:

$$\delta\mathcal{L}_p = \frac{1}{2}\chi_{+}(\partial_{\tau}\theta_{+})^2 + \frac{\rho_{s0}}{m}(\nabla\theta_{+})^2 + \frac{1}{2}\chi_{-}(\partial_{\tau}\theta_{-})^2 + \frac{\rho_0}{m}(\partial_z\theta_{-})^2 + \frac{1}{4m^3\alpha^2}(\nabla_{\perp}^2\theta_{-})^2, \quad (2.161)$$

where the compressibilities are given by

$$\chi_{-} = \frac{2}{\lambda - \lambda_{12}}, \quad (2.162)$$

$$\chi_{+} = \frac{g + 4g_{+} - 4g_{am}}{g_{+}g - g_{am}^2}, \quad (2.163)$$

with $g_{+} = \frac{1}{2}(\lambda + \lambda_{12})$.

Thus, the in-phase and out-of-phase Goldstone modes are characterized by dispersions:

$$\omega_{+p}(\mathbf{k}) = c_{+}k, \quad (2.164)$$

$$\omega_{-p}(\mathbf{k}) = \sqrt{(Bk_z^2 + Kk_{\perp}^4)/\chi_{-}}, \quad (2.165)$$

with defined parameters

$$c_{+} = \sqrt{\frac{2\rho_{s0}}{\chi_{+}m}}, \quad (2.166)$$

$$B = \frac{2\rho_0}{m}, \quad (2.167)$$

$$K = \frac{1}{2m^3\alpha^2}. \quad (2.168)$$

The linear $\omega_+(k)$ dispersion of the superfluid phase θ_+ is the expected Bogoliubov mode corresponding to the superfluid order. The anisotropic smectic-like dispersion of the “phonon” θ_- is a reflection of the uniaxial finite-momentum order in the AMSF_p state, akin to the Fulde-Ferrell superconductor[8, 110].

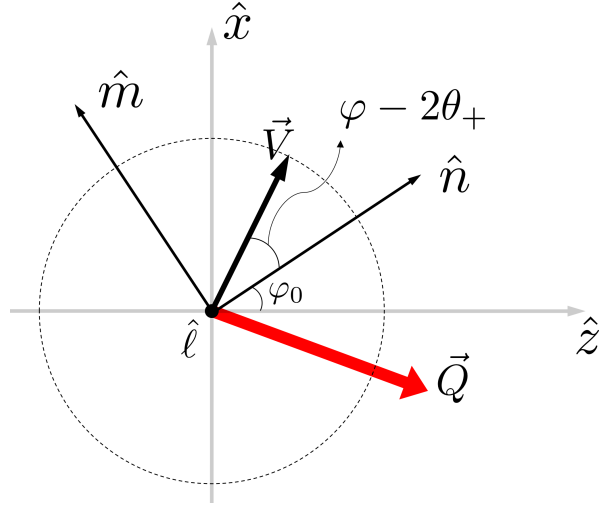


Figure 2.17: The diagram defining various vectors appearing in Eq. (2.169). $\vec{V} = \hat{n} \cos(\varphi - 2\theta_+) - \hat{m} \sin(\varphi - 2\theta_+)$, while $\varphi - 2\theta_+$ is measured relative to \hat{n} axis and φ_0 is measured relative to \hat{z} .

2.5.3.2 ferromagnetic AMSF_{fm}

The analysis for the ferromagnetic AMSF_{fm} phase is very similar, with only a single modification of the MSF_{fm} order parameter, given instead by $\hat{\phi}$ in Eq. (2.145). The corresponding

fluctuations Lagrangian density is given by:

$$\begin{aligned}
\delta\mathcal{L}_{\text{fm}} \approx & i\delta\rho_+\partial_\tau\theta_+ + \frac{\rho_0}{m}(\nabla\theta_+)^2 + i\delta\rho_-\partial_\tau\theta_- + \frac{\rho_0}{m}(\nabla\theta_- + \mathbf{Q})^2 + i\delta\rho_m\partial_\tau(\varphi - \varphi_0) + i\rho_{m0}\hat{\mathbf{n}} \cdot \partial_\tau\hat{\mathbf{m}} \\
& + \frac{\rho_{m0}}{4m}(\nabla\varphi)^2 + \frac{\rho_{m0}}{8m}(\nabla\hat{\mathbf{n}})^2 + \frac{\rho_{m0}}{8m}(\nabla\hat{\mathbf{m}})^2 + \frac{1}{16m\rho_{m0}}(\nabla\rho_m)^2 \\
& - \sqrt{2}\alpha\rho_0\sqrt{\rho_{m0}}(\nabla\theta_- + \mathbf{Q}) \cdot [\hat{\mathbf{n}}\cos(\varphi - 2\theta_+) - \hat{\mathbf{m}}\sin(\varphi - 2\theta_+)] \\
& + \frac{1}{16m\rho_0}(\nabla\rho_+)^2 + \frac{1}{16m\rho_0}(\nabla\rho_-)^2 + \frac{\lambda}{4}\delta\rho_+^2 + \frac{\lambda}{4}\delta\rho_-^2 + \frac{\lambda_{12}}{4}(\delta\rho_+^2 - \delta\rho_-^2) \\
& + g_{am}\delta\rho_+\delta\rho_m + \frac{g_1}{2}\delta\rho_m^2, \tag{2.169}
\end{aligned}$$

$$\begin{aligned}
\approx & i(\delta\rho_+ + 2\delta\rho_m)\partial_\tau\theta_+ + \frac{\rho_{s0}}{m}(\nabla\theta_+)^2 + i\delta\rho_-\partial_\tau\theta_- + \frac{\rho_0}{m}\left(\nabla\theta_- - \frac{1}{\sqrt{2}}\alpha m\sqrt{\rho_{m0}}\delta\hat{\mathbf{n}}\right)^2 \\
& + i\rho_{m0}\delta\hat{\mathbf{n}} \cdot \partial_\tau\hat{\mathbf{m}} + \frac{\rho_{m0}}{8m}(\nabla\hat{\mathbf{n}})^2 + \frac{\rho_{m0}}{8m}(\nabla\hat{\mathbf{m}})^2 + \frac{1}{16m\rho_0}(\nabla\rho_+)^2 + \frac{1}{16m\rho_0}(\nabla\rho_-)^2 \\
& + \frac{1}{16m\rho_{m0}}(\nabla\rho_m)^2 + \frac{\lambda}{4}\delta\rho_+^2 + \frac{\lambda}{4}\delta\rho_-^2 + \frac{\lambda_{12}}{4}(\delta\rho_+^2 - \delta\rho_-^2) + g_{am}\delta\rho_+\delta\rho_m + \frac{g_1}{2}\delta\rho_m^2, \tag{2.170}
\end{aligned}$$

where to get the second form we performed a gauge transformation to absorb the $\hat{\mathbf{n}} - \hat{\mathbf{m}}$ planar rotations angle $\hat{\mathbf{m}} \cdot \partial_\tau\hat{\mathbf{n}} \equiv \partial_\tau\varphi_0$ into $\partial_\tau\varphi$ and to simplify the Feshbach resonance term, as well as subsequently integrated out φ , completed the square into a minimal-like coupling for $\nabla\theta_-$, and chose $\mathbf{Q} = \alpha m\sqrt{\frac{\rho_{m0}}{2}}\hat{\mathbf{n}}_0$, similar to the polar state analysis of the previous subsection.

Integrating out $\delta\hat{\mathbf{n}}$, with the effective minimal-coupling constraint, Eq. (2.160) and the constraint on the in-plane ($\hat{\mathbf{n}} - \hat{\mathbf{m}}$) component of $\delta\hat{\mathbf{m}}$

$$\hat{\mathbf{n}} \cdot \delta\hat{\mathbf{m}} = -\hat{\mathbf{m}} \cdot \delta\hat{\mathbf{n}}, \tag{2.171}$$

at long scales we find

$$\begin{aligned}
\delta\mathcal{L}_{\text{fm}} \approx & i(\delta\rho_+ + 2\delta\rho_m)\partial_\tau\theta_+ + \frac{\rho_{s0}}{m}(\nabla\theta_+)^2 + i\delta\rho_-\partial_\tau\theta_- + \frac{\rho_0}{m}(\partial_z\theta_-)^2 + \frac{1}{4m^3\alpha^2}(\nabla\nabla_\perp\theta_-)^2 \\
& + \frac{1}{4m^3\alpha^2}(\nabla\partial_x\theta_-)^2 + i\frac{\sqrt{2}\rho_{m0}}{\alpha m}\partial_y\theta_-\partial_\tau\gamma + \frac{\rho_{m0}}{8m}(\nabla\gamma)^2 + \frac{1}{16m\rho_0}(\nabla\rho_+)^2 + \frac{1}{16m\rho_0}(\nabla\rho_-)^2 \\
& + \frac{1}{16m\rho_{m0}}(\nabla\rho_m)^2 + \frac{\lambda}{4}\delta\rho_+^2 + \frac{\lambda}{4}\delta\rho_-^2 + \frac{\lambda_{12}}{4}(\delta\rho_+^2 - \delta\rho_-^2) + g_{am}\delta\rho_+\delta\rho_m + \frac{g_1}{2}\delta\rho_m^2, \tag{2.172}
\end{aligned}$$

$$\begin{aligned}
= & \frac{1}{2}\chi_+(\partial_\tau\theta_+)^2 + \frac{\rho_{s0}}{m}(\nabla\theta_+)^2 + \frac{1}{2}\chi_-(\partial_\tau\theta_-)^2 + \frac{1}{2}B(\partial_z\theta_-)^2 + \frac{1}{2}K_x(\nabla\partial_x\theta_-)^2 + \frac{1}{2}K_y(\nabla\partial_y\theta_-)^2 \\
& + i\kappa\partial_y\theta_-\partial_\tau\gamma + \frac{1}{2}J(\nabla\gamma)^2, \tag{2.173}
\end{aligned}$$

where we used $[\nabla(\delta\hat{\mathbf{m}})]^2 = [\nabla(\hat{\mathbf{n}} \cdot \delta\hat{\mathbf{m}})]^2 + [\nabla(\hat{\ell} \cdot \delta\hat{\mathbf{m}})]^2$, introduced couplings

$$\kappa = \frac{\sqrt{2\rho_{m0}}}{\alpha m}, \quad (2.174)$$

$$K_x = \frac{1}{m^3\alpha^2} = K, \quad (2.175)$$

$$K_y = \frac{1}{2m^3\alpha^2}, \quad (2.176)$$

$$J = \frac{\rho_{m0}}{4m} = K_y Q^2, \quad (2.177)$$

defined a real scalar field

$$\gamma \equiv \hat{\ell} \cdot \delta\hat{\mathbf{m}}, \quad (2.178)$$

for fluctuations of $\hat{\mathbf{m}}$ outside of the $\hat{\mathbf{n}} - \hat{\mathbf{m}}$ plane, and chose axes

$$\hat{\mathbf{x}} = \hat{\mathbf{m}}, \quad (2.179)$$

$$\hat{\mathbf{y}} = \hat{\ell}. \quad (2.180)$$

We note that the Goldstone-modes action, Eq. (2.5.3.2), exhibits a **biaxial** smectic energetics in the smectic phonon, θ_- , in addition to the xy -model energetics of the superfluid phase, θ_+ . The biaxiality is expected and arises due to a smectic in-plane polar (p -wave) order, characterized by a spinor ϕ_{fm} , with the quantization axis, $\hat{\ell}$. The finite angular momentum, $\ell_z = \pm 1$ along $\hat{\ell}$ distinguishes AMSF_{fm} from AMSF_p and leads to an additional Goldstone mode γ .

A straightforward diagonalization of the above Lagrangian leads to dispersions for three Goldstone modes inside the AMSF_{fm} state:

$$\omega_{fm}^+(\mathbf{k}) = c_+ k, \quad (2.181)$$

$$\omega_{fm}^-(\mathbf{k}) = \sqrt{[Bk_z^2 + k^2(K_x k_x^2 + K_y k_y^2)]/\chi_-}, \quad (2.182)$$

$$\omega_{fm}^\gamma(\mathbf{k}) = \sqrt{\frac{Jk^2[Bk_z^2 + k^2(K_x k_x^2 + K_y k_y^2)]}{J\chi_- k^2 + \kappa^2 k_y^2}}. \quad (2.183)$$

The anisotropic $\omega_{fm}^\gamma(\mathbf{k})$ dispersion corresponds to the ferromagnetic spin-waves in the plane of atomic condensate phase-fronts (“smectic layers”) of the p -wave atomic-molecular condensate, AMSF_{fm} , reducing to the dispersion of MSF_{fm} in Eq. (2.5.2.2) for a vanishing smectic order, with $B = 0$.

2.6 Phase Transitions

In this section, we study the quantum MSF - AMSF phase transitions beyond earlier mean-field approximation, demonstrating that they are described by a $d+1$ dimensional quantum de Gennes (Abelian Higg's) model[100] akin to that for a normal-to-superconductor and nematic-to-smectic-A transitions. Based on the extensive work for these systems [129, 130], in three (spatial) dimensions ($d = 3$) we predict that the effective gauge-field fluctuations drive this transition first-order. The derivation is most transparent via a coherent-state Lagrangian, Eq. (2.2.0.2),

$$\begin{aligned}
\mathcal{L} = & \psi_\sigma^* (\partial_\tau - \frac{\nabla^2}{2m} - \mu_\sigma) \psi_\sigma + \phi^* \cdot (\partial_\tau - \frac{\nabla^2}{4m} - \mu_m) \cdot \phi + \frac{\lambda_\sigma}{2} |\psi_\sigma|^4 \\
& + \lambda_{12} |\psi_1|^2 |\psi_2|^2 + g_{am} (|\psi_1|^2 + |\psi_2|^2) |\phi|^2 + \frac{g_1}{2} |\phi^* \cdot \phi|^2 + \frac{g_2}{2} |\phi \cdot \phi|^2 \\
& + \frac{\alpha}{2} (\phi^* \cdot [\psi_1(-i\nabla)\psi_2 - \psi_2(-i\nabla)\psi_1] + c.c.), \tag{2.184}
\end{aligned}$$

working in polar representation similar to that of the previous subsection.

2.6.1 MSF_p-AMSF_p polar transition

It is convenient to analyze the transition from the MSF side, where the atomic and molecular order parameters are given by,

$$\psi_\sigma = \psi_{\sigma, \mathbf{Q}_\sigma} e^{i\mathbf{Q}_\sigma \cdot \mathbf{r}}, \quad \mathbf{Q}_\sigma = \pm \mathbf{Q}, \quad \text{for } \sigma = 1, 2 \tag{2.185}$$

$$\phi = \sqrt{\rho_{m0}} e^{i\varphi(\mathbf{r})} \hat{\mathbf{n}}. \tag{2.186}$$

Using these forms inside \mathcal{L} , Eq. (2.184) and for simplicity focusing on the balanced case with $\tilde{\mu} = \tilde{\mu}_\sigma = \mu_\sigma - g_{am}\rho_{m0}$, we obtain

$$\begin{aligned}
\mathcal{L}_p = & \psi_{1,\mathbf{Q}}^* \partial_\tau \psi_{1,\mathbf{Q}} + \psi_{2,-\mathbf{Q}}^* \partial_\tau \psi_{2,-\mathbf{Q}} + \left(\frac{Q^2}{2m} - \tilde{\mu} \right) (|\psi_{1,\mathbf{Q}}|^2 + |\psi_{2,-\mathbf{Q}}|^2) + \frac{1}{2m} |\nabla \psi_{\sigma,\mathbf{Q}}|^2 \\
& + \left(\frac{1}{2m} \mathbf{Q}_\sigma \cdot \psi_{\sigma,\mathbf{Q}}^* (-i\nabla) \psi_{\sigma,\mathbf{Q}} \right. \\
& \left. - \alpha \sqrt{\rho_{m0}} e^{-i\varphi} \hat{\mathbf{n}} \cdot \left(\mathbf{Q} \psi_{1,\mathbf{Q}} \psi_{2,-\mathbf{Q}} + \frac{1}{2} [\psi_{1,\mathbf{Q}} (-i\nabla) \psi_{2,-\mathbf{Q}} - \psi_{2,-\mathbf{Q}} (-i\nabla) \psi_{1,\mathbf{Q}}] \right) + c.c. \right) \\
& + i\delta\rho_m \partial_\tau \varphi + i\rho_{m0} \delta\mathbf{m} \cdot \partial_\tau \hat{\mathbf{n}} + \frac{\rho_{m0}}{4m} (\nabla\varphi)^2 + \frac{\rho_{m0}}{4m} (\nabla\hat{\mathbf{n}})^2 + \frac{g}{2} \delta\rho_m^2 + \frac{g^2}{2} \rho_{m0}^2 |\delta\mathbf{m}|^2 + \mathcal{L}_{\text{int}} + \mathcal{L}_{\text{msf}},
\end{aligned} \tag{2.187}$$

where terms linear in fields vanish by virtue of the saddle point equations. The contribution \mathcal{L}_{msf} is the mean-field part analyzed in Sec. 2.4 and \mathcal{L}_{int} is the higher order terms. Defining

$$\varepsilon_Q = \frac{Q^2}{2m} - \tilde{\mu}, \tag{2.188}$$

$$\Delta_{\mathbf{Q}} = \alpha \sqrt{\rho_{m0}} \hat{\mathbf{n}} \cdot \mathbf{Q}, \tag{2.189}$$

and introducing atomic eigenfields ψ_\pm

$$\psi_+ = \frac{1}{\sqrt{2}} (-\psi_{1,\mathbf{Q}} + \psi_{2,-\mathbf{Q}}^*), \tag{2.190}$$

$$\psi_- = \frac{1}{\sqrt{2}} (\psi_{1,\mathbf{Q}} + \psi_{2,-\mathbf{Q}}^*), \tag{2.191}$$

mean-field version of which was obtained in Sec. 2.4, the Lagrangian simplifies considerably to,

$$\begin{aligned}
\mathcal{L}_p = & -\psi_+^* \partial_\tau \psi_- + \psi_+ \partial_\tau \psi_-^* \\
& + \frac{1}{2m} |(-i\nabla + \mathbf{Q} + \alpha m \sqrt{\rho_{m0}} \hat{\mathbf{n}} \cos \varphi) \psi_+|^2 + \frac{1}{2m} |(-i\nabla + \mathbf{Q} - \alpha m \sqrt{\rho_{m0}} \hat{\mathbf{n}} \cos \varphi) \psi_-|^2 \\
& + \left[\epsilon_+ - \frac{1}{2m} (\mathbf{Q} + \alpha m \sqrt{\rho_{m0}} \hat{\mathbf{n}} \cos \varphi)^2 \right] |\psi_+|^2 + \left[\epsilon_- - \frac{1}{2m} (\mathbf{Q} - \alpha m \sqrt{\rho_{m0}} \hat{\mathbf{n}} \cos \varphi)^2 \right] |\psi_-|^2 \\
& + i\alpha \sqrt{\rho_{m0}} \hat{\mathbf{n}} \cdot (\psi_+ (-i\nabla) \psi_-^* - \psi_-^* (-i\nabla) \psi_+) \sin \varphi \\
& + \frac{1}{2g} (\partial_\tau \varphi)^2 + \frac{\rho_{m0}}{4m} (\nabla\varphi)^2 + \frac{1}{2g_2} (\partial_\tau \hat{\mathbf{n}})^2 + \frac{\rho_{m0}}{4m} (\nabla\hat{\mathbf{n}})^2 \\
& + \mathcal{L}_{\text{int}} + \mathcal{L}_{\text{msf}},
\end{aligned} \tag{2.192}$$

where

$$\epsilon_{\pm} = \epsilon_Q \pm |\Delta_{\mathbf{Q}}| \quad (2.193)$$

and we completed the square in \mathcal{L}_p . It can be shown that near a critical point the $\sin \varphi$ contribution leads to an irrelevant quartic correction to $|\psi_-|^4$ and renormalization of $(\partial_{\parallel} \psi_-)^2$ stiffness. Furthermore, it is clear that the canonically conjugate field ψ_+ (it appears as a canonical momentum for the critical field ψ_-) remains massive at the MSF-AMSF transition, defined by the vanishing of the coefficient of $|\psi_-|^2$ term, consistent with Sec. 2.4. Therefore, safely integrating out ψ_+ and making a choice $\mathbf{Q} = \alpha m \sqrt{\rho_{m0}} \hat{\mathbf{n}}_0$ that minimizes the energy, leads to

$$\begin{aligned} \mathcal{L}_p = & \epsilon_+^{-1} |\partial_{\tau} \psi_-|^2 + \frac{1}{2m} |(-i\nabla - \alpha m \sqrt{\rho_{m0}} \delta \hat{\mathbf{n}}) \psi_-|^2 + \epsilon_- |\psi_-|^2 + \frac{\lambda}{2} |\psi_-|^4 + \frac{1}{2g_2} (\partial_{\tau} \hat{\mathbf{n}})^2 + \frac{\rho_{m0}}{4m} (\nabla \hat{\mathbf{n}})^2 \\ & + \frac{1}{2g} (\partial_{\tau} \varphi)^2 + \frac{\rho_{m0}}{4m} (\nabla \varphi)^2, \end{aligned} \quad (2.194)$$

with $\lambda = \frac{1}{4}(\lambda_1 + \lambda_2 + 2\lambda_{12})$, and we dropped the mean-field part and irrelevant interactions.

Thus, as anticipated on symmetry grounds, the zero-temperature MSF_p-AMSF_p transition is indeed described by a quantum ($(d+1)$ -dimensional) de Gennes model (or equivalently the Ginzburg-Landau) Lagrangian [100], where the role of the nematic director (gauge-field) is played by the $\ell_z = 0$ quantization axis of the p -wave molecular condensate.

2.6.2 MSF_{fm}-AMSF_{fm} ferromagnetic transition

Using the fields form appropriate for the ferromagnetic case

$$\psi_{\sigma} = \psi_{\sigma \mathbf{Q}_{\sigma}} e^{i\mathbf{Q}_{\sigma} \cdot \mathbf{r}}, \quad \mathbf{Q}_{\sigma} = \pm \mathbf{Q}, \quad \text{for } \sigma = 1, 2 \quad (2.195)$$

$$\phi = \sqrt{\frac{\rho_{m0}}{2}} (\hat{\mathbf{n}} + i\hat{\mathbf{m}}), \quad (2.196)$$

a very similar analysis leads to

$$\begin{aligned}
\mathcal{L}_{\text{fm}} &= \epsilon_+ |\psi_+|^2 + \epsilon_- |\psi_-|^2 + \frac{1}{2m} |\nabla \psi_+|^2 + \frac{1}{2m} |\nabla \psi_-|^2 + i\rho_m \hat{\mathbf{n}} \cdot \partial_\tau \hat{\mathbf{m}} + \frac{\rho_{m0}}{8m} (\nabla \hat{\mathbf{n}})^2 + \frac{\rho_{m0}}{8m} (\nabla \hat{\mathbf{m}})^2 \\
&\quad + \alpha \frac{\sqrt{\rho_{m0}}}{\sqrt{2}} (\hat{\mathbf{n}} - i\hat{\mathbf{m}}) \cdot (\psi_+^* (-i\nabla) \psi_+ - \psi_-^* (-i\nabla) \psi_-) \\
&\quad + \frac{\mathbf{Q}}{m} \cdot (\psi_+^* (-i\nabla) \psi_+ + \psi_-^* (-i\nabla) \psi_-) - \psi_+^* \partial_\tau \psi_- + \psi_+ \partial_\tau \psi_-^* + \frac{g}{2} \delta \rho_m^2 + \mathcal{L}_{\text{int}} + \mathcal{L}_{\text{msf}}, \quad (2.197) \\
&= -\psi_+^* \partial_\tau \psi_- + \psi_+ \partial_\tau \psi_-^* \\
&\quad + \frac{1}{2m} \left| \left(-i\nabla + \mathbf{Q} + \frac{1}{\sqrt{2}} \alpha m \sqrt{\rho_{m0}} \hat{\mathbf{n}} \right) \psi_+ \right|^2 + \frac{1}{2m} \left| \left(-i\nabla + \mathbf{Q} - \frac{1}{\sqrt{2}} \alpha m \sqrt{\rho_{m0}} \hat{\mathbf{n}} \right) \psi_- \right|^2 \\
&\quad + \left[\epsilon_+ - \frac{1}{2m} \left(\mathbf{Q} + \frac{1}{\sqrt{2}} \alpha m \sqrt{\rho_{m0}} \hat{\mathbf{n}} \right)^2 \right] |\psi_+|^2 + \left[\epsilon_- - \frac{1}{2m} \left(\mathbf{Q} - \frac{1}{\sqrt{2}} \alpha m \sqrt{\rho_{m0}} \hat{\mathbf{n}} \right)^2 \right] |\psi_-|^2 \\
&\quad + i\rho_m \hat{\mathbf{n}} \cdot \partial_\tau \hat{\mathbf{m}} + \frac{\rho_{m0}}{8m} (\nabla \hat{\mathbf{n}})^2 + \frac{\rho_{m0}}{8m} (\nabla \hat{\mathbf{m}})^2 + \alpha \frac{\sqrt{\rho_{m0}}}{\sqrt{2}} (-i\hat{\mathbf{m}}) \cdot (\psi_+^* (-i\nabla) \psi_- - \psi_+ (+i\nabla) \psi_-^*) \\
&\quad + \frac{g}{2} \delta \rho_m^2 + \mathcal{L}_{\text{int}} + \mathcal{L}_{\text{msf}}, \quad (2.198)
\end{aligned}$$

where to obtain the final form we rotated $\hat{\mathbf{n}}$ and $\hat{\mathbf{m}}$ by $-\varphi$ and completed the square. Similarly to the treatment of the polar case in the previous subsection, here it can be shown that the linear $(-i\hat{\mathbf{m}})$ term only leads to irrelevant quartic coupling and can therefore be neglected. Integrating out the noncritical conjugate field ψ_+ , gives the final Lagrangian form

$$\begin{aligned}
\mathcal{L}_{\text{fm}} &= \epsilon_+^{-1} |\partial_\tau \psi_-|^2 + \frac{1}{2m} \left| \left(-i\nabla - \frac{\alpha m \sqrt{\rho_{m0}}}{\sqrt{2}} \delta \hat{\mathbf{n}} \right) \psi_- \right|^2 \\
&\quad + \epsilon_- |\psi_-|^2 + \frac{\lambda}{2} |\psi_-|^4 + \frac{\rho_{m0}}{8m} (\nabla \hat{\mathbf{n}})^2 + \frac{\rho_{m0}}{8m} (\nabla \hat{\mathbf{m}})^2 + i\rho_m \hat{\mathbf{n}} \cdot \partial_\tau \hat{\mathbf{m}} \quad (2.199)
\end{aligned}$$

of the quantum de Gennes-Ginzburg-Landau form that controls the $\text{MSF}_{\text{fm}}\text{-AMSF}_{\text{fm}}$ transition. In above we dropped the mean-field part and irrelevant interactions. As anticipated by symmetry, it is distinguished from the polar case by the additional biaxial order whose fluctuations are characterized by $\hat{\mathbf{m}}$.

2.7 Topological Defects

Having established the nature of the ordered states, characterized by Landau order parameters, and the associated Goldstone modes, we now turn to a brief discussion of the corresponding

topological defects. As usual, these singular excitations are crucial to a complete characterization of the states and their disordering, particularly in the case of non-meanfield (e.g., partially disordered) states that are not uniquely characterized by a Landau order parameter.

2.7.1 Defects in ASF

As discussed in Sec.2.4, the ASF_{*i*} states (with $i = 1, 2, 12$) are characterized by two atomic condensate order parameters, $\psi_\sigma = \sqrt{\rho_\sigma} e^{i\theta_\sigma}$. Correspondingly, as in an ordinary superfluid, because θ_σ are **compact** phase fields (θ_σ and $\theta_\sigma + 2\pi$ are physically identified), in addition to their smooth Goldstone mode configurations, there are vortex topological excitations, corresponding to nonsingle-valued configurations of $\theta_\sigma(\mathbf{r})$. These are defined by two corresponding integer-valued closed line integral, enclosing a vortex line

$$\oint d\vec{\ell} \cdot \vec{\nabla} \theta_\sigma = 2\pi p_\sigma. \quad (2.200)$$

In a differential form, the line defects are equivalently encoded as

$$\nabla \times \nabla \theta_\sigma = \mathbf{m}_\sigma, \quad (2.201)$$

with vortex line topological “charge” density given by

$$\mathbf{m}_\sigma(\mathbf{r}) = 2\pi \sum_i \int p_\sigma^i \hat{\mathbf{t}}_i(s_i) \delta^3(\mathbf{r} - \mathbf{r}_i(s_i)) ds_i, \quad (2.202)$$

where s_i parametrizes the i 'th vortex line (or loop), $\mathbf{r}_i(s_i)$ gives its positional conformation, $\hat{\mathbf{t}}_i(s_i)$ is the local unit tangent, and vortex “charges” p_σ^i are independent of s_i , since the charge of a given line is constant along the defect. Furthermore,

$$\nabla \cdot \mathbf{m}(\mathbf{r}) = 0 \quad (2.203)$$

enforces the condition that vortex lines cannot end in the bulk of the sample; they must either form closed loops or extend entirely through the system.

Thus, vortices in the single-component ASF _{σ} states are characterized by a n_σ integer, and in the two-component ASF₁₂ the defects are specified by a pair of integers (p_1, p_2) . These are

associated with the fundamental group π_1 of the torus $U(1) \otimes U(1)$, that characterizes the low-energy manifold of Goldstone modes of the ASF_{12} state. It is therefore closely related to other $U(1) \otimes U(1)$ systems, such as easy-plane spinor-1 condensates [131] and two-gap superconductors, e.g., MgB_2 [132].

As in conventional superfluids vortices appear in response to imposed rotation and proliferate with enhanced quantum and thermal fluctuations, providing a complementary description of phase transitions out of the ASF_i states.

2.7.2 Defects in MSF

Because of its finite angular momentum, $\ell = 1$ structure the defects in the MSF states are somewhat more complicated. However, relying on the aforementioned relation of the MSF to the well-explored spinor-1 condensates [79, 93, 84, 85, 90, 91], we inherit a clear characterization of defects in the two MSF phases. As discussed in Sec. 2.4 the polar MSF_p and the ferromagnetic MSF_{fm} states are respectively characterized by $[S_2 \times U_N(1)]/\mathbb{Z}_2$ (the mod out by \mathbb{Z}_2 corresponds to the identification of $\hat{\mathbf{n}} \rightarrow -\hat{\mathbf{n}}$ with $\varphi \rightarrow \varphi + \pi$) and $SO(3)$ order-parameter (Goldstone modes) manifolds. The defects are characterized by the homotopy group of the corresponding manifolds. In the ferromagnetic MSF_{fm} case the $SO(3)=S_3/\mathbb{Z}_2$ manifold also appears in the dipole-locked A phase of Helium-3 with topological defects well understood [133].

The nature of defects in the polar MSF_p state was a subject of some debate, until it was definitively resolved by Mukerjee, *et al.* [93]. These are characterized by elements of the homotopy groups $\pi_n(S_2 \times U_N(1)/\mathbb{Z}_2) = \mathbb{Z}$. The key new feature is the appearance of a composite defect that is a π -vortex and $\hat{\mathbf{n}}$ texture where $\hat{\mathbf{n}} \rightarrow -\hat{\mathbf{n}}$, keeping the molecular order parameter single-valued at long scales. The consequences of this were discussed and explored through Monte Carlo simulations by Mukerjee, *et al.* [93], and is quite closely related to other realizations of composite half-integer defects [34, 36, 35, 109, 110]. We expect the MSF_p to exhibit similar phenomenology, that we do not explore further here.

2.7.3 Defects in AMSF

As discussed in Sec. 2.4, in addition to the molecular condensate ϕ , the two AMSF states are characterized by a finite momentum two-component atomic condensate order parameter, with a nonzero amplitude

$$\Psi_- = e^{-i\varphi}\Psi_{1,\mathbf{Q}} + \Psi_{2,-\mathbf{Q}}^*, \quad (2.204)$$

and a vanishing amplitude $\Psi_+ = 0$, Eq. (2.55). The latter is consistent with the locking of the atomic condensate phase $\theta_+ = \frac{1}{2}(\theta_1 + \theta_2)$ to a molecular superfluid phase $\varphi/2$, imposed by the FR coupling, Eq. (2.5.3.1). It also locks the atomic condensate magnitudes to be equal, $|\Psi_{1,\mathbf{Q}}| = |\Psi_{2,-\mathbf{Q}}|$.

Using the phase representation, the atomic condensate order parameter reduces to

$$\Psi_- \sim e^{i\theta_-} e^{-i\varphi/2} \cos(\theta_+ - \varphi/2). \quad (2.205)$$

From this form it is clear that, as a conventional superfluid, the AMSF admits 2π -vortices in $\theta_- = \frac{1}{2}(\theta_1 - \theta_2)$, and $\varphi = 0$, corresponding to a 2π “spin”-vortex,

$$\theta_-(\mathbf{r}) = \theta_1(\mathbf{r}) = -\theta_2(\mathbf{r}), \quad (2.206)$$

$$= \theta, \quad 2\pi \text{ “spin”-vortex}, \quad (2.207)$$

with equal counter-propagating (atomic species 1 and 2) currents, and a vanishing “charge”-(atomic number) current. Above, θ is a polar coordinate angle.

Another type of a defect is topologically equivalent to a 2π -vortex in $\theta_+(\mathbf{r})$,

$$\theta_+(\mathbf{r}) = \theta_1(\mathbf{r}) = \theta_2(\mathbf{r}), \quad (2.208)$$

$$= \theta, \quad 2\pi \text{ “charge”-vortex}, \quad (2.209)$$

with equal co-propagating (atomic species 1 and 2) currents, and a vanishing “spin”-current. However, as is clear from the Feshbach interaction form in Eq. (2.147)

$$\delta\mathcal{L}_{FBR} \sim \cos(\varphi - 2\theta_+), \quad (2.210)$$

for vortex-free molecular order parameter (e.g. $\varphi = 0$), inside the AMSF phase the “charge”-vortex 2π winding and currents are confined to a domain wall whose thickness is set by the ratio of the superfluid stiffness and FR coupling α , on the order of $1/Q$. As a result of this current confinement the energy of such domain-wall scales linearly in 2d and as a surface in 3d. Consequently, such $\pm 2\pi$ “charge”-vortices are confined into neutral pairs inside the AMSF phase. However, in the presence of a molecular 4π -vortex, with $\varphi(\mathbf{r}) = 2\theta_+(\mathbf{r}) = 2\theta$ no domain wall appears and a conventional $\pm 2\pi$ “charge”-vortices can deconfine.

Finally, as with other analogous physical systems [109, 110], the product form of the atomic condensate order parameter, Ψ_- , Eq. (2.204) admits composite defects with half-integer topological charge. These are characterized by a bound state of a π -“spin” and $\pm\pi$ -“charge” vortices, with latter (as above) confined by FR interaction into a $\pm\pi$ domain-wall. A simplest (topologically faithful) realization of this is a vortex only in one (but not both) atomic species,

$$\theta_+(\mathbf{r}) = \theta_-(\mathbf{r}) = \frac{1}{2}\theta_1(\mathbf{r}) = \frac{1}{2}\theta, \quad \theta_2(\mathbf{r}) = 0,$$

$$(+\pi) - (+\pi) \text{ vortex domain-wall}, \tag{2.211}$$

$$\theta_+(\mathbf{r}) = -\theta_-(\mathbf{r}) = \frac{1}{2}\theta_2(\mathbf{r}) = \frac{1}{2}\theta, \quad \theta_1(\mathbf{r}) = 0,$$

$$(-\pi) - (+\pi) \text{ vortex domain-wall}. \tag{2.212}$$

Again, in the presence of a $\pm 2\pi$ molecular vortex, $\varphi(\mathbf{r}) = \pm\theta$, the π -“spin”, π -“charge” composite vortex, $\theta_-(\mathbf{r}) = \pm\theta_+(\mathbf{r}) = \frac{\theta}{2}$ no longer exhibits a domain wall, since $\varphi - 2\theta_+ = 2\pi p$. It is therefore not confined inside the AMSF state.

Clearly, out of above six types of defects, the 2π -“spin” vortex is least energetically costly, because it does not involve a “charge” domain-wall in θ_+ , nor requires an additional molecular vortex. On the other hand it is the two half-integer vortex domain-wall defects that are the elementary ones. This therefore opens up a possibility of unconventional nonsuperfluid states in the two-species p -wave resonant Bose systems, driven by unbinding of composite topological defects, like the 2π -“spin” vortex. We leave the discussion of the resulting states to future work.

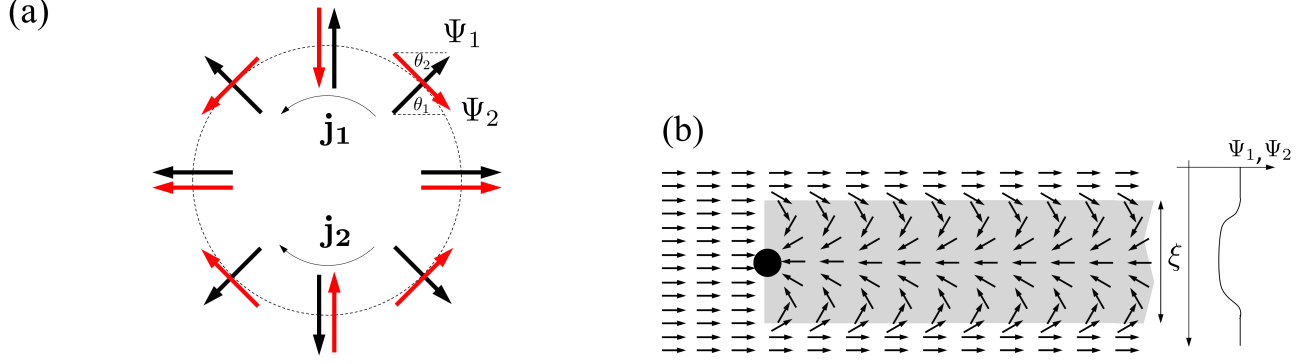


Figure 2.18: (a) 2π “spin” vortex with equal counter-propagating atomic currents, \mathbf{j}_1 , \mathbf{j}_2 . (b) 2π “charge” vortex with equal co-propagating currents, confined to a domain wall (grey area), of width $\xi \sim 1/Q$, with atomic order parameter suppressed. In the presence of a molecular 4π -vortex domain wall is no longer required, and the “charge” vortex is deconfined.

2.8 Local Density Approximation

Because the primary experimental application of our predictions is to degenerate atomic gases it is important to extend our analysis to include the trapping potential $V_t(\mathbf{r})$, that in a typical experiment is well-approximated by a harmonic potential. A full analysis of the effect of the trap is beyond the scope of this manuscript, and here we will limit our treatment to a local density approximation (LDA).

Closely related to the WKB approximation [112], LDA amounts to the bulk system predictions, but with the chemical potential replaced by an effective local chemical potential $\mu(r) = \mu - V_t(r)$. The validity of the LDA relies on the smoothness of the trap potential, with the criterion that $V_t(r)$ varies slowly on the scale of the *longest* physical length λ in the problem, i.e., $(\lambda/V_t(r))dV_t(r)/dr \ll 1$. Its accuracy can be equivalently controlled by a ratio of the single-particle trap level spacing δE to the smallest characteristic energy E_c of the studied phenomenon (e.g, the chemical potential, condensation energy, etc.), by requiring $\delta E/E_c \ll 1$. For our system the longest natural length scale is the period $2\pi/Q$, Eq. (2.1) of the finite-momentum atomic condensate inside the AMSF state. Thus, away from the AMSF-ASF phase boundary, where Q vanishes (see Fig. 2.2), we expect an LDA treatment of the effects of the trap to be trustworthy.

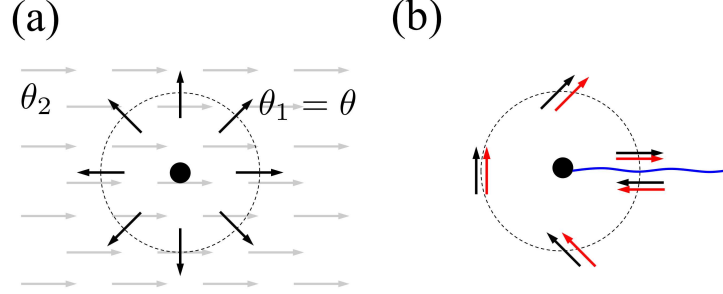


Figure 2.19: $\pi - \pi$ vortex in $\alpha = 0$ limit. (a) In $\theta_1 - \theta_2$ representation; black (grey) arrows indicate θ_1 (θ_2). (b) In $\theta_+ - \theta_-$ representation, the pair of arrows indicate θ_+ and θ_- , while wavy line indicates a domain wall. For $\alpha \neq 0$, the Feshbach resonance coupling “squeezes” the θ_+ π -vortex textures into a domain wall of width $\xi \sim 1/Q$. In the presence of an additional molecular 2π vortex, the domain wall is absent and the composite defect is deconfined.

A generalization of a resonant Bose gas model, Eq. (2.9) to include a trap is straightforward, accounted for by the additional Hamiltonian density

$$\mathcal{H}_{\text{trap}} = \sum_{\sigma=1,2} V_i(\mathbf{r}) \hat{\psi}_\sigma^\dagger \hat{\psi}_\sigma + 2V_i(\mathbf{r}) \hat{\phi}^\dagger \cdot \hat{\phi}, \quad (2.213)$$

with $\mathcal{H} \rightarrow \mathcal{H} + \mathcal{H}_{\text{trap}}$. In above, for simplicity we specialized to an atomic species-independent trapping potential, and approximated the closed-channel molecular trapping potential by twice the atomic one, valid for the interaction range r_0 (typically less than 50\AA) much smaller than the cloud size R (typically larger than a micron).

Henceforth, to be concrete, we shall focus on an isotropic harmonic trap (although this simplification can easily be relaxed) with

$$V_i(\mathbf{r}) = \frac{1}{2} m \omega_i^2 r^2, \quad (2.214)$$

$$\equiv \mu \frac{r^2}{R^2}, \quad (2.215)$$

latter expression defining the cloud size R . Within LDA, locally the system is taken to be well-approximated as *uniform*, but with a local chemical potential given by

$$\mu(r) \equiv \mu - \frac{1}{2} m \omega_i^2 r^2, \quad (2.216)$$

$$= \mu \left(1 - \frac{r^2}{R^2} \right), \quad (2.217)$$

where μ is the true chemical potential (a Lagrange multiplier) enforcing the total atom number N . The spatially-varying species 1 and 2 chemical potentials are then given by:

$$\mu_1(r) = \mu(r) + h, \quad (2.218)$$

$$\mu_2(r) = \mu(r) - h, \quad (2.219)$$

with a *uniform* chemical potential difference h set by the atomic species imbalance [104, 105, 110].

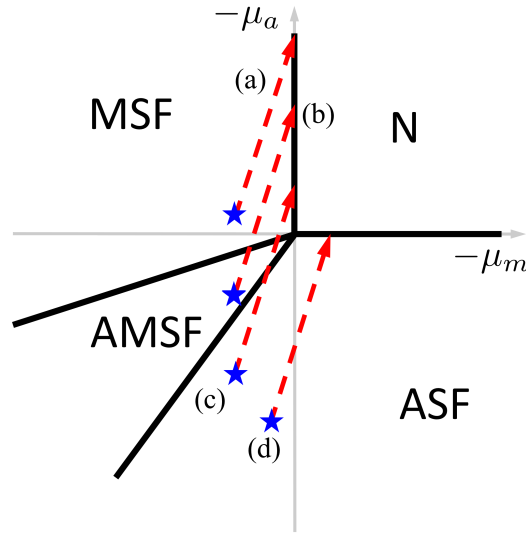


Figure 2.20: N, ν, T dependent cuts through the bulk phase diagram with increasing radial position r through the atomic cloud. Stars indicate system's parameters (local chemical potentials μ_a, μ_m) at the trap center.

Consequently, within LDA the system's energy density is approximated by that of a uniform bulk system, Eq. (2.29), with the spatial dependence entering only through $\mu(r)$. The ground state energy is then simply a volume integral of this energy density. Thus, the phase behavior of a uniform system as a function of the chemical potential, μ , translates into a spatial cloud profile through $\mu(r)$, with the critical phase boundaries μ_c corresponding to critical radii defined by $\mu_c = \mu(r_c, h)$ [104, 105]. As predicted [134, 104] and observed [10, 135, 136, 137, 138] in other systems this leads to a shell-like cloud structure “imaging” of the bulk phase diagram as illustrated in Fig. 2.20.

Applying this LDA analysis to our system leads to a prediction of rich, magnetic field, atom number, and temperature tunable shell structures in a p -wave resonant Bose gas, schematically illustrated in Fig. 2.21. For a range of atom number, detuning, and temperature admitting the AMSF phase, we expect a cloud shell with an r -dependent atomic condensate wavevector $q(r)$, given by

$$q(r) = \alpha m \sqrt{n_m(r)}, \quad (2.220)$$

$$\approx q_0 \sqrt{1 - \frac{r^2}{R^2}}, \quad \text{for } r_{\text{MSF}} < r < r_{\text{ASF}}, \quad (2.221)$$

where $r_{\text{MSF}}(T, N, \nu)$ and $r_{\text{ASF}}(T, N, \nu)$ are the boundaries of the AMSF shell.

2.9 Summary and Conclusions

To summarize, we studied a degenerate gas of two-species bosonic atoms interacting through a p -wave Feshbach resonance, as realized for example in a ^{85}Rb - ^{87}Rb mixture. We mapped out the corresponding phase diagram and thermodynamic properties of the phases as a function of temperature, atom number and Feshbach-resonance detuning, and analyzed the nature of corresponding phase transitions. We showed that at intermediate detuning such atomic quantum gas generically exhibits an atomic-molecular superfluid (AMSF) state with atoms condensed at a finite tunable momentum $\mathbf{Q}(\nu)$ along a direction set by the angular momentum axis of the molecular condensate. This AMSF state undergoes quantum phase transitions described by a quantum de Gennes model into a molecular p -wave (orbital spinor-1) superfluid (MSF) and into an s -wave atomic superfluid (ASF) at large negative and positive detunings, respectively. A magnetic field can be used to tune the modulation wavevector of the AMSF between zero and a value set by interactions as well as to drive quantum phase transitions in this rich system.

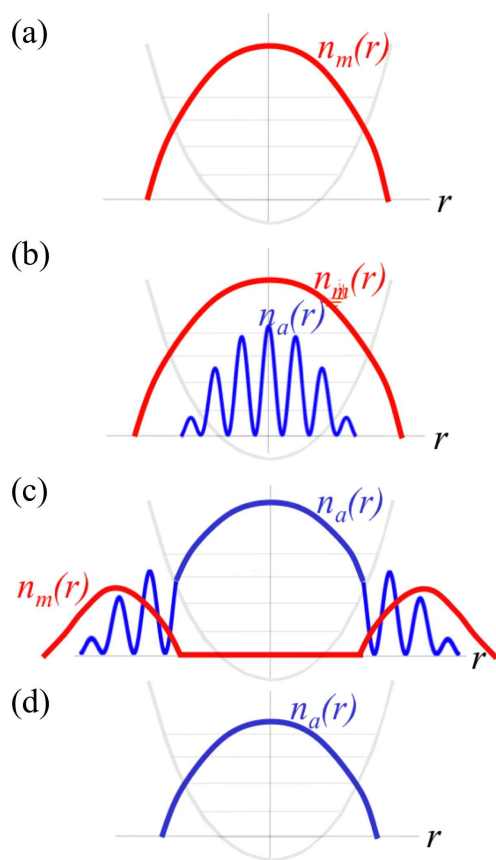


Figure 2.21: Schematic illustration of the shell structure expected in the p -wave resonant atomic cloud, corresponding to the phase diagram cuts in Fig. 2.20.

Chapter 3

Finite momentum phase of Fe_{1+y}Te

3.1 Introduction

3.1.1 Iron-based superconductors and magnetism

Initiated by Hosono and co-worker's discovery of iron-based high-temperature superconductivity in fluorine-doped LaOFeAs [6], there have been tremendous research activity and developments in the area of iron-based superconductors. While searching for higher transition temperature and its mechanism, many classes of materials were discovered and analyzed extensively, theoretically and experimentally [7]. The most well-known materials are the 1111 (such as LaOFeAs) and 122 (such as BaFe_2As_2) compounds, conventionally referred to as FeAs materials.

These iron pnictides exhibit many interesting features that have attracted considerable attention [7]. Their phase diagram exhibits similarities to that of cuprate superconductors, with the pairing mechanism that is believed to be unconventional (i.e., non-phonon mediated). Concomitant with this is the superconducting order parameter that is predicted to be (with some experimental evidence [40, 41, 42]). of an unconventional, extended (s_{++} and s_{\pm} , alternating sign around the Brillouin zone but fully gapped on the Fermi pockets) s -wave type. Angle resolved photoemission spectroscopy (ARPES) and inelastic neutron scattering (INS) studies suggest that the nesting along $(\pi, 0)$ axis¹ accompanied by the spin density wave (SDW) plays a central role for mediating

¹ We use a 2d convention for the reciprocal lattice vector $q = (q_a, q_b)$ with the coordinate system in terms X, Y coordinates (diagonals a, b of the original square lattice), and the $q_z = \pi/2$ component implied. For the bi-collinear state, it is given by $(\pi, 0)$, that is equivalent to the $q' = (\pi/2, \pi/2)$ in the original xy square lattice coordinate system. In terms of reciprocal lattice unit notations used by experimentalists, this is given by $q = [1/2, 0, 1/2]$.

superconducting mechanism.

More recently discovered, the so-called 11 materials (e.g. FeSe and FeTe based compounds) also show superconductivity with doping of sulfur or selenium. Their simpler structures, with no atoms at the interplanar layer is hoped to be present a simpler challenge of uncovering the nature of the pairing mechanism, but still to shed light more generally on iron-based and other strongly correlated superconductors.

With magnetism believed to be central to high temperature superconductivity and interesting in its own right, much attention has also recently turned to magnetic parent compounds, such as the self-doped Fe_{1+y}Te [45, 46, 47, 48, 49, 50]. It is observed to exhibit a number of novel characteristics. The most interesting of these is an unconventional bi-collinear planar magnetic state, with a commensurate, planar spin-spiral order characterized by $(\pi/2, \pi/2)$ wavevector in the orthorhombic ab -plane [45]. A first-order magnetic transition to this state at 67.5K is accompanied by a structural transition to an orthorhombic (with slight monoclinicity) state [46]. At low temperature the magnetic order also undergoes a commensurate to incommensurate (CI) spiral transition with iron doping at $y \simeq 0.12$, with low doping corresponding to the commensurate phase [139].

Measurement of the Curie-Weiss susceptibility with a large magnetic moment of order $2\mu_B$ [46] and no Fermi surface nesting observed in DFT [47] and ARPES [48] suggest that (despite its metallic nature) a local moment description may be sufficient to capture magnetism in Fe_{1+y}Te compounds. This is supported by first-principles electron structure calculations that observe the formation of the iron local moments [52, 53]. There have also been a few analytical and first-principle studies based on the local moment description [49, 50, 51, 52, 53]. Turner *et al.* [49] assumed that the electrons are localized and the structural transition is driven by an orbital ordering resulting from Jahn-Teller coupling. Their model consists of super-exchange and double exchange interactions, which together favor an incommensurate (nearly bi-collinear) state, as well as a spin-lattice interaction driven biquadratic exchange which favors the commensurate bi-collinear state. Fang *et al.* [50] also developed a local spin model with a relatively complicated exchange interaction. They obtained a rich phase diagram which includes, the two relevant phases observed in Fe_{1+y}Te . Yin *et al.* [51]

unified the two pictures based on itinerant electrons and localized spin in Fe_{1+y}Te in analogy with manganites [140]. They pointed out the sensitive competition between the superexchange and orbital-degenerate double-exchange ferromagnetism, finding several collinear states including the bi-collinear spin state. Although these models are successful in capturing the bi-collinear and incommensurate spin-spiral states observed in FeTe , their underlying spin-rotational invariance predicts gapless spinwaves, at odds with experimental observations [141, 142] of gapped spectrum in the commensurate bi-collinear state that appears for $y < 0.12$.

The main motivation for our study is the recent inelastic neutron scattering experiments by Parshall *et al.* [143] on a $y = 0.08$ Fe_{1+y}Te sample. These experiments have observed an *incommensurate* inelastic peak (at $q_1 = [0.45, 0, 0.5]$) in the dynamic structure function that precipitously shifts to a commensurate position (at $q_0 = [1/2, 0, 1/2]$) below the transition at $T_N = 67.5\text{K}$ to the bi-collinear magnetic state.

We also aim to understand and model the aforementioned earlier finding of a transition as a function of increasing Fe doping from the commensurate bi-collinear to the incommensurate spin-spiral state at $y_c = 0.12$.

The rest of the paper is organized as follows. We conclude the Introduction with the summary of our main results and their experimental implications. In Section II, we introduce a microscopic model that is an extension of that in Ref. [49], incorporating a key new ingredient of single-ion anisotropy and omitting the superfluous biquadratic exchange. We use it to compute the low-energy magnetic excitation spectrum and to derive the hydrodynamic theory in Section III. We use the latter to map out the temperature-doping phase diagram in Section IV, and to compute the static and dynamic structure functions in the context of recent experiments in the paramagnetic and magnetically ordered phases in Section V. We conclude the paper in Section VI with a summary and discussion of our predictions.

3.1.2 Summary of results

Before turning to the detailed analysis of the system, we outline the main results of our work.

Motivated by experimental observations [45, 46, 139, 143], we introduce an exchange model for Fe_{1+y}Te that primarily builds on studies by Turner *et al.*'s [49], supplementing their model with single-ion easy-plane orthorhombic anisotropy

$$\mathcal{H}_{\text{ani}} = \sum_i D_{ab} \left[(S_i^a)^2 - (S_i^b)^2 \right], \quad (3.1)$$

and omitting their biquadratic exchange that we believe is unnecessary to capture FeTe phenomenology. Here $S_i^{a,b}$ are the spin component along a and b axes at i th site and D_{ab} is the orthorhombic anisotropy coefficient arising below the structural transition.

To model the single-ion anisotropy in Eq. (3.1), we also study a magneto-elastic Landau model, where magnetic order and orthorhombic strain are coupled. Through the analysis of this model we predict a generic phase diagram, illustrated in Fig. 3.6, that exhibits a variety of phases, such as: (1) tetragonal paramagnet, (2) orthorhombic paramagnet, (3) orthorhombic commensurate (bi-collinear), and (4) orthorhombic incommensurate planar spiral states.

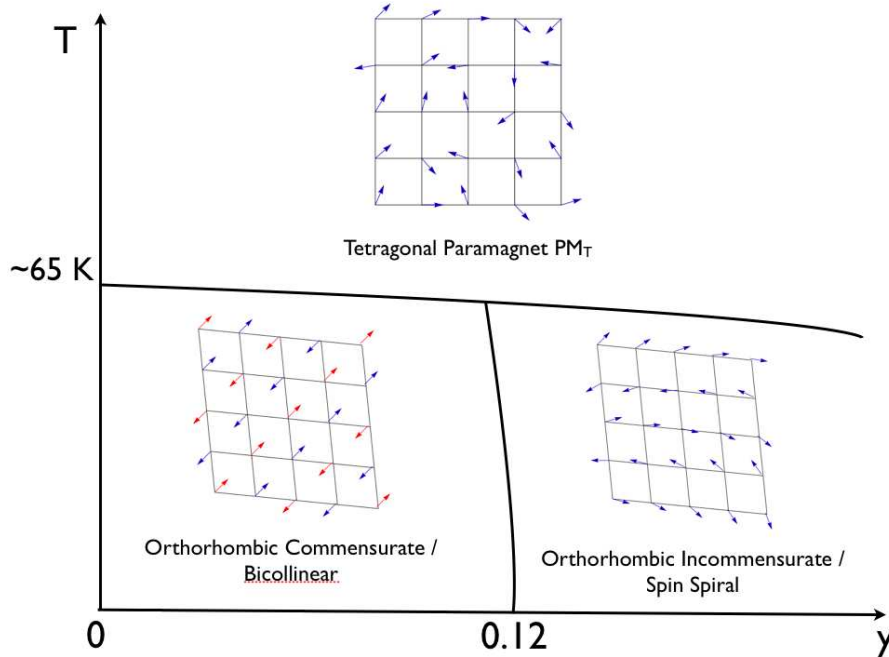


Figure 3.1: The schematic global phase diagram of Fe_{1+y}Te in T and y (doping) space.

\mathcal{H}_{ani} explicitly breaks the spin rotational symmetry (present in Ref. [49, 50, 51]) and leads to

a gapped spin-wave excitation spectrum in the bi-collinear (commensurate) state and gapless one in the incommensurate spiral state,

$$\epsilon_k^c = \sqrt{c_a k_a^2 + c_b k_b^2 + c_z k_z^2 + D_{ab}^2}, \quad (3.2a)$$

$$\epsilon_k^{ic} = \sqrt{c_a k_a^2 + c_b k_b^2 + c_z k_z^2}, \quad (3.2b)$$

that we derive within the Holstein-Primakoff analysis. These are consistent with experimental observations [139, 141, 142, 143]. The parameters appearing in the above spectra are given in Eq. (3.27).

We use this microscopic model to derive a hydrodynamic theory, from which we compute the corresponding dynamic structure function. Utilizing hydrodynamic description, we also compute static and dynamic structure functions on the approach to the magnetically ordered states, respectively given by Eq. (3.85), (3.98) illustrated in Figs. 3.11, 3.12. The pole of the later in the ordered state (calculated in Sec. 3.5) also gives the spectrum Eq. 3.2. Consistent with experimental finding by Parshall *et al.* [143], upon lowering of temperature it displays an inelastic peak shift from incommensurate q_1 to commensurate q_0 value (see Fig. 3.11, 3.12).

For a range of parameters the model admits a direct first-order transition from a tetrahedral paramagnet to orthorhombic commensurate bi-collinear spiral, as observed in Fe_{1+y}Te . However, it also allows a more generic range of possibilities of continuous transitions through intermediate phases as seen in FeAs materials [144].

Finally, at low T in the ordered state, we show that the system exhibits a commensurate-to-incommensurate spin-spiral transition controlled by the Pokrovsky-Talapov model [145]. We compute the corresponding static structure function, whose peak shifts from commensurate to incommensurate value as domain-walls proliferate at $y_c = 0.12$. As illustrated in Fig 3.7, just above the transition, the dilute gas of domain-walls also induces higher harmonic peaks given by

$$I_{ic}(k) = \sum_p \frac{4}{2p+1} \delta(k - \frac{1}{2}q_0 - q - 2\pi p/d) \quad (3.3)$$

with the amplitude peaks at low T given universally a sequence $4/(2p+1)$, where q_0 is a commensurate wavevector.

Having summarized the results of our study, we next turn to the detailed description of our model.

3.2 Model of FeTe

3.2.1 Microscopic model

3.2.1.1 Orbitals, exchange interaction, and single-ion anisotropy

Our microscopic model for Fe_{1+y}Te is based on the local $S = 1$ exchange model introduced by Turner *et al.* [49]. Although FeTe compounds are metallic, we assume that the magnetism in Fe_{1+y}Te is described by localized electrons with spin $S = 1$ due to the local moment features of iron telluride alluded to in the Introduction. The main difference between our model and that of Ref. [49] is our introduction of the single-ion anisotropy that explicitly breaks spin-rotational symmetry, consistent with the orthorhombic low-temperature crystal structure, spin-orbit interaction and the observed gapped spinwave spectrum in the bi-collinear (commensurate spiral) state. Microscopically, the transition to orthorhombic state can be argued to be associated with the orbital ordering via Jahn-Teller coupling [49]. However, here we capture it more simply, phenomenologically through a magnetoelastic coupling, that we analyze in Sec. 3.2.3. Also in contrast to Ref. [49], we neglect the biquadratic exchange, that furthermore we believe is not necessary to capture the FeTe phenomenology.

At low temperatures, Fe_{1+y}Te distorts from a tetragonal to a weakly monoclinic structure for small Fe doping and to an orthorhombic structure for large Fe doping. Since the monoclinic distortion is fairly weak, with $\beta \simeq 89.2$ degrees [45], we neglect it for simplicity and take the low temperature crystal structure to be orthorhombic. At low temperature, the degeneracy of d_{Yz} and d_{Xz} Fe^{2+} orbitals of the high temperature tetragonal phase (with $a = b$) is lifted as indicated in Fig. 3.2, with crystal elongated along a and compressed along b axes ($a > b$). As shown in Fig. 3.2, the lower e_g orbitals are both doubly occupied and the upper d_{xy} and d_{Xz} orbitals are singly occupied, forming a local spin moment $S = 1$.

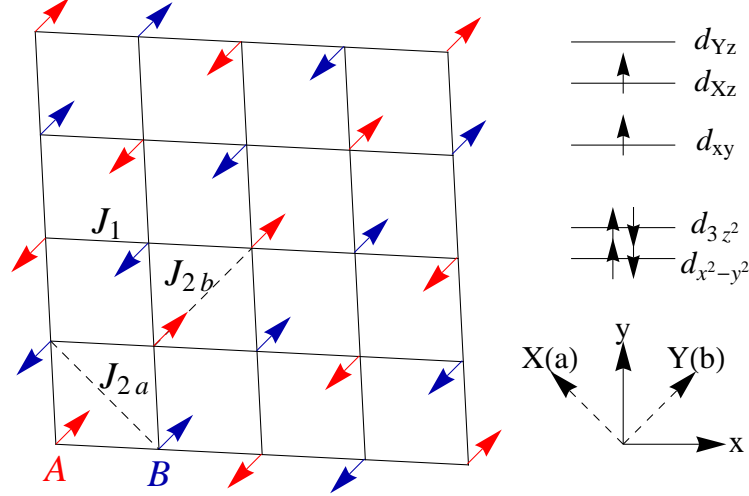


Figure 3.2: Left : Bi-collinear state with spins locked by the single-ion anisotropy to the xy -plane along the b -axis, and exchange couplings of the model Eq. (3.5) indicated; Upper right : the electron configuration of Fe^{2+} in the orthorhombic phase; Lower right : the choice of coordinates.

As discussed in Ref. [49], because of the single occupancy of d_{xy} and d_{Xz} orbitals, the exchange interaction, J_{2a} , along a (or equivalently X) axis is expected to be antiferromagnetic. On the other hand, along the b (Y) axis that is more metallic we take it to be a ferromagnetic exchange, J_{2b} , via a double exchange of the extra electron on the upper d_{YZ} orbital due to Fe (self-) doping. Such ferromagnetic exchange can also arise due to the nearly 90 degree exchange path [50]. In addition these second neighbor exchanges, J_{2a} and J_{2b} (NNN), we include an antiferromagnetic exchange J_1 between nearest neighbors (NN), that for simplicity we take to be the same along x and y . The orthorhombic single-ion anisotropy energy is allowed by symmetry and microscopically arises from the second order contribution of the spin-orbit interaction. It is given by,

$$\mathcal{H}_{\text{ani}} = - \sum_i \left[A_a (S_i^a)^2 + A_b (S_i^b)^2 \right] \quad (3.4)$$

with $S_i^a = (S_i^x - S_i^y)/\sqrt{2}$ and $S_i^b = (S_i^x + S_i^y)/\sqrt{2}$. $A_{a,b}$ are the orthorhombic anisotropy coefficients which we will provide the relation to D_{ab} later. As discussed in Sec. 3.2.3, such contribution naturally arises through a magnetoelastic interaction which leads the condition, $A_b > A_a > 0$ that favors magnetic alignment along the b axis. Thus, we take the full model Hamiltonian for Fe_{1+y}Te

to be given by

$$\mathcal{H} = J_1 \sum_{\langle ij \rangle} \mathbf{S}_i \cdot \mathbf{S}_j + J_{2a} \sum_{\langle\langle ij \rangle\rangle_a} \mathbf{S}_i \cdot \mathbf{S}_j - J_{2b} \sum_{\langle\langle ij \rangle\rangle_b} \mathbf{S}_i \cdot \mathbf{S}_j - \sum_i \left[A_a (S_i^a)^2 + A_b (S_i^b)^2 \right]. \quad (3.5)$$

We study its properties first microscopically in mean-field approximation together with spin-wave analysis appropriate at low temperature inside the ordered states. We supplement this with a hydrodynamic theory more appropriate at high temperatures, that allows us to map out the phase diagram and to compute the dynamic structure function measured via inelastic neutron scattering in Ref. [143].

3.2.1.2 Phase diagram and spin wave excitation

First we find the ground state of \mathcal{H} for vanishing single-ion anisotropy, $A_a = A_b$, treating spins classically. Straightforward calculation shows that the ground state of such \mathcal{H} is a coplanar spin spiral with an ordering wavevector $(k_1, -k_1)$, given by

$$\cos k_1 = -\frac{J_1}{2J_{2a}}. \quad (3.6)$$

Generically this spin spiral is incommensurate for $J_1/(2J_{2a}) < 1$. When $\frac{J_1}{2J_{2a}} \geq 1$, the ground state is conventional (π, π) Néel state on the square lattice.

The inclusion of single-ion anisotropy raises the competition between the exchange interaction that favors the incommensurate spin-spiral order and the commensurate spiral state with spins aligned along the b axis for $A_b > A_a$. The commensurate wavevector can be either $\pi/2$ or π , but is selected by the antiferromagnetic J_{2a} exchange to be close to $(\pi/2, -\pi/2)$. Consequently, when single-ion anisotropy dominates, it locks the spiral to the $(\pi/2, -\pi/2)$ wavevector with collinear magnetic order along b -axis, a state dubbed “bi-collinear”. With this ordering wavevector, the nearest-neighbor exchange interaction J_1 is quenched and the two sublattices of the square lattice effectively decouple.

Treating spin classically, we find the energy per site for the incommensurate spin-spiral order

$$E_{\text{ic}}(k_1, -k_1)|_{\cos k_1 = -\frac{J_1}{2J_{2a}}} = - \left(J_{2a} + J_{2b} + \frac{J_1^2}{2J_{2a}} \right) - \frac{A_a + A_b}{2}, \quad (3.7)$$

and for the commensurate bi-collinear order

$$E_c(\pi/2, -\pi/2) = -(J_{2a} + J_{2b}) - A_b. \quad (3.8)$$

Comparing these energies, we obtain a phase diagram depicted in Fig. 3.3.

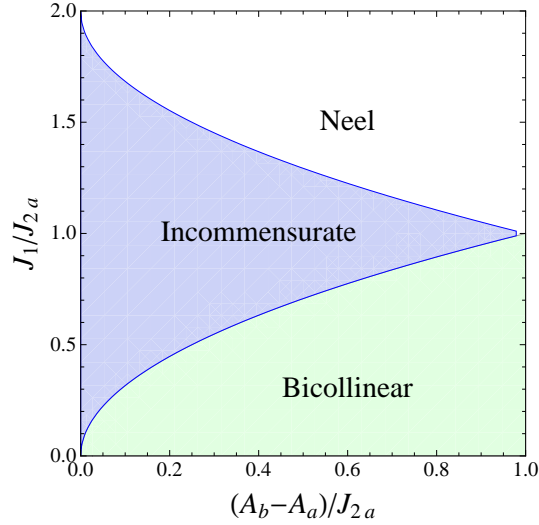


Figure 3.3: Phase diagram of our microscopic Hamiltonian. Solid lines are phase boundary determined by comparing the classical energies.

We now turn our attention to the spin wave excitations that we study using the standard Holstein-Primakoff analysis.

For the incommensurate spin spiral state, the classical (average) spin orientation at site (x_i, y_i) is given by

$$\hat{n}_i = (\cos(k_1 x_i - k_1 y_i), \sin(k_1 x_i - k_1 y_i), 0), \quad (3.9)$$

and the spin operators can be written as

$$\mathbf{S}_i \cdot \hat{n}_i = S - a_i^\dagger a_i, \quad (3.10a)$$

$$S_i^+ \equiv (\hat{z} + i\hat{n}_i \times \hat{z}) \cdot \mathbf{S}_i = \sqrt{2S} a_i, \quad (3.10b)$$

$$S_i^- \equiv (\hat{z} - i\hat{n}_i \times \hat{z}) \cdot \mathbf{S}_i = \sqrt{2S} a_i^\dagger. \quad (3.10c)$$

For the commensurate bi-collinear spin state, we label the two sublattices of the square lattice as A and B as the spin state is not a proper state [146]. The spin orientations for two sublattices

are parametrized as follows

$$\hat{n}_{A,i} = (-)^{(x_i - y_i)/2} \left(\frac{1}{\sqrt{2}}, \frac{1}{\sqrt{2}}, 0 \right), \quad (3.11a)$$

$$\hat{n}_{B,i} = (-)^{(x_i - y_i - 1)/2} \left(\frac{1}{\sqrt{2}}, \frac{1}{\sqrt{2}}, 0 \right) \quad (3.11b)$$

where $x_i - y_i$ is even (odd) for A (B) sublattice. We express the spin operators as

$$\mathbf{S}_{A,i} \cdot \hat{n}_i = S - a_i^\dagger a_i, \quad (3.12a)$$

$$S_{A,i}^+ \equiv (\hat{z} + i\hat{n}_{A,i} \times \hat{z}) \cdot \mathbf{S}_{A,i} = \sqrt{2S}a_i, \quad (3.12b)$$

$$S_{A,i}^- \equiv (\hat{z} - i\hat{n}_{A,i} \times \hat{z}) \cdot \mathbf{S}_{A,i} = \sqrt{2S}a_i^\dagger \quad (3.12c)$$

and

$$\mathbf{S}_{B,i} \cdot \hat{n}_i = S - b_i^\dagger b_i, \quad (3.13a)$$

$$S_{B,i}^+ \equiv (\hat{z} + i\hat{n}_{B,i} \times \hat{z}) \cdot \mathbf{S}_{B,i} = \sqrt{2S}b_i, \quad (3.13b)$$

$$S_{B,i}^- \equiv (\hat{z} - i\hat{n}_{B,i} \times \hat{z}) \cdot \mathbf{S}_{B,i} = \sqrt{2S}b_i^\dagger. \quad (3.13c)$$

Plugging this parametrization into the Hamiltonian (3.5) and approximating to quadratic order of the magnon operators, we obtain the spin-wave Hamiltonian for the incommensurate spin spiral state,

$$\mathcal{H}_{\text{ic}} = \sum_{\mathbf{k}} \epsilon_{\mathbf{k}}^{ic} a_{\mathbf{k}}^\dagger a_{\mathbf{k}} + \nu_{\mathbf{k}} a_{\mathbf{k}}^\dagger a_{-\mathbf{k}}^\dagger + \nu_{\mathbf{k}} a_{\mathbf{k}} a_{-\mathbf{k}} + \mathcal{N} E_{\text{ic}}(k_1, -k_1)|_{\cos k_1 = -J_1/(2J_{2a})}, \quad (3.14)$$

with \mathcal{N} the number of lattice sites and

$$\begin{aligned} \epsilon_{\mathbf{k}}^{ic} = S & \left[\frac{A_a + A_b}{2} + 2(J_{2a} + J_{2b}) + \frac{J_1^2}{J_{2a}} + J_1(\cos k_x + \cos k_y) - 2J_{2b} \cos(k_x + k_y) \right. \\ & \left. - \frac{J_1^2}{2J_{2a}} (\cos k_x - \cos(k_x - k_y) + \cos k_y) \right] \end{aligned} \quad (3.15)$$

$$\nu_{\mathbf{k}} = S \left[\frac{A_a + A_b}{4} + \left(1 - \frac{J_1^2}{4J_{2a}^2} \right) J_{2a} \cos(k_x - k_y) + \frac{J_1}{2} \left(1 + \frac{J_1}{2J_{2a}} \right) (\cos k_x + \cos k_y) \right]. \quad (3.16)$$

In above expressions we eliminated the spiral incommensurate wavevector k_1 in favor of its optimum value given by Eq. (3.6).

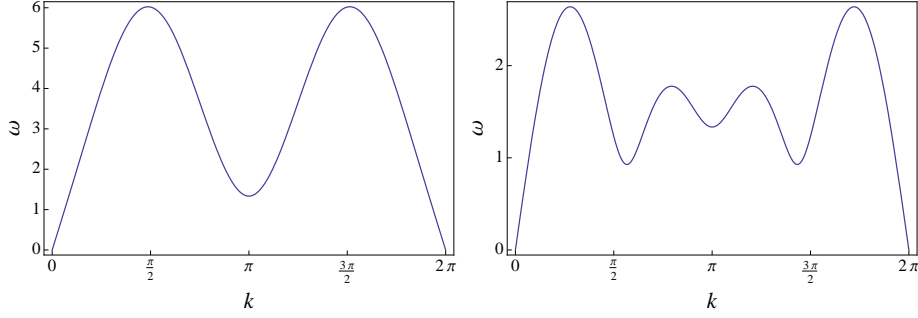


Figure 3.4: The spin wave dispersion of the incommensurate spin spiral state for $J_{2a} = J_{2b} = 1$, $J_1 = 0.4$, $A_a = 0.1$, $A_b = 0.12$. Upper : the dispersion along (k, k) . Lower : the dispersion along $(k, -k)$.

For the commensurate phase, we have

$$\mathcal{H}_c = \sum_{\mathbf{k}} (\mu_{\mathbf{k}} a_{\mathbf{k}}^\dagger b_{\mathbf{k}} + m_{\mathbf{k}} a_{\mathbf{k}}^\dagger b_{-\mathbf{k}}^\dagger + n_{\mathbf{k}} a_{\mathbf{k}}^\dagger a_{-\mathbf{k}}^\dagger + h.c.) + \epsilon_{\mathbf{k}}^c (a_{\mathbf{k}}^\dagger a_{\mathbf{k}} + b_{\mathbf{k}}^\dagger b_{\mathbf{k}}) + \mathcal{N} E_c \left(\frac{\pi}{2}, -\frac{\pi}{2} \right) \quad (3.17)$$

with

$$\epsilon_{\mathbf{k}}^c = \frac{S}{2} \left[J_{2a} + A_b - \frac{A_a}{2} + J_{2b}(1 - \cos(k_x + k_y)) \right] \quad (3.18a)$$

$$\mu_{\mathbf{k}} = J_1 S (e^{ik_x} + e^{-ik_y}) \quad (3.18b)$$

$$m_{\mathbf{k}} = J_1 S (e^{-ik_x} + e^{ik_y}) \quad (3.18c)$$

$$n_{\mathbf{k}} = S \left[\frac{A_a}{2} + J_{2a} \cos(k_x - k_y) \right] \quad (3.18d)$$

The corresponding spin-wave dispersions are readily obtained, and as illustrated in Figs. 3.4, 3.5 are gapless for the incommensurate and gapped for commensurate bi-collinear states, respectively.

3.2.2 Effective continuum model

As we can see from the previous section, the microscopic lattice model gives us the ground state and spin excitation spectrum of Fe_{1+y}Te consistent with its experimental studies [139, 141, 142, 143]. However, to study the low-energy fluctuations more universally and in more detail, particularly near the continuous phase transition and beyond mean-field theory, it is convenient to formulate the system's description using a continuum Landau-Wilson functional, that can be derived from the above microscopic model.

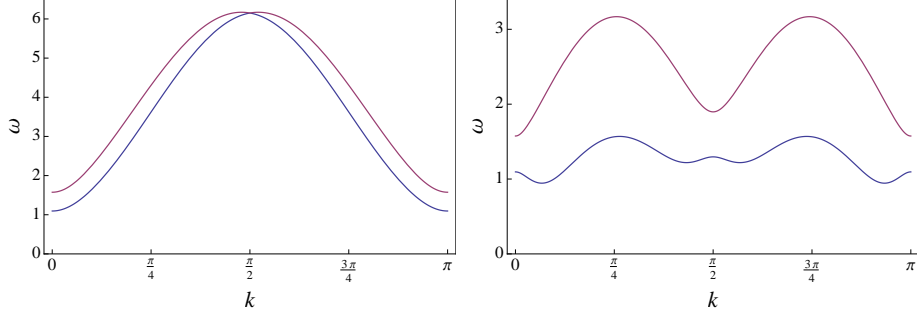


Figure 3.5: The spin wave dispersion of the bi-collinear spin state for $J_{2a} = J_{2b} = 1$, $J_1 = 0.4$, $A_a = 0.1$, $A_b = 0.3$. Upper : the dispersion along (k, k) . Lower : the dispersion along $(-k, k)$.

We start from the partition function for the microscopic model, Eq. (3.5),

$$\mathcal{Z} = \text{Tr} \exp \left[-\beta \sum_{i,j} J_{ij} \mathbf{S}_i \cdot \mathbf{S}_j - \beta \mathcal{H}_{\text{ani}} \right] \quad (3.19)$$

with the exchange-coupling matrix J_{ij} . Here, $J_{ij} = J_1$, J_{2a} or $-J_{2b}$ when ij connects first neighbor or second neighbor sites along a and b directions, respectively.

Using the Hubbard-Stratonovich transformation by introducing an auxiliary field ϕ_i to decouple the exchange interactions, we have

$$\mathcal{Z} = \int \mathcal{D}\phi e^{\frac{\beta}{4} \sum_{ij} J_{ij}^{-1} \phi_i \cdot \phi_j} \text{Tr} e^{-\beta \mathcal{H}_{\text{ani}}} e^{-\beta \sum_i \mathbf{S}_i \cdot \phi_i}. \quad (3.20)$$

Expanding around the saddle point gives

$$\mathcal{Z} = \int \mathcal{D}\phi \exp[-\mathcal{S}_{\text{eff}}] \quad (3.21)$$

where the effective action \mathcal{S}_{eff} is given by

$$\begin{aligned} \mathcal{S}_{\text{eff}} = \int_0^\beta d\tau \sum_{ij} \left[-J_{ij}^{-1} \frac{\phi_i^\alpha \phi_j^\alpha}{2} + \frac{(\partial_\tau \phi_i^a)^2}{A_b^3} + \frac{(\partial_\tau \phi_i^b)^2}{A_a^3} - \frac{(\phi_i^a)^2}{A_b} - \frac{(\phi_i^b)^2}{A_a} \right. \\ \left. + \left(\frac{(\phi_i^a)^4}{A_b^3} + \frac{(\phi_i^b)^4}{A_a^3} + \frac{(\phi_i^a)^2 (\phi_i^b)^2}{A_a A_b} \left(\frac{1}{A_a} + \frac{1}{A_b} \right) - \frac{(\phi_i^z)^2}{A_a A_b} \left(\frac{(\phi_i^a)^2}{A_b} + \frac{(\phi_i^b)^2}{A_a} \right) \right) \right]. \quad (3.22) \end{aligned}$$

In the disordered, paramagnetic state it is sufficient to only quadratic terms with the effective Hamiltonian,

$$\mathcal{H}_0 = \sum_{ij} \left[-J_{ij}^{-1} \frac{\phi_i^\alpha \phi_j^\alpha}{2} - \frac{(\phi_i^a)^2}{A_b} - \frac{(\phi_i^b)^2}{A_a} \right]. \quad (3.23)$$

Let us consider the exchange term first. J_{ij}^{-1} is a 2×2 matrix and one of the eigenvalue corresponds to the ground state energy, e_g whose minimum is at $\mathbf{k}_1 = (k, -k)$ or $(-k, k)$ with $\cos k = -\frac{J_1}{2J_{2a}}$ depending on the value of Hamiltonian couplings. Going to Fourier space, expanding the dispersion in \mathcal{H}_0 around \mathbf{k}_1 is straightforward and changing the basis from xy plane to ab plane using

$$\begin{pmatrix} k_a \\ k_b \end{pmatrix} = \begin{pmatrix} 1 & -1 \\ 1 & 1 \end{pmatrix} \begin{pmatrix} k_x \\ k_y \end{pmatrix} \quad (3.24)$$

gives

$$\mathcal{H}_0 = \frac{1}{2} \boldsymbol{\phi} \cdot \boldsymbol{\epsilon}_{\mathbf{k}}^0 \cdot \boldsymbol{\phi} + D_{ab}(\phi_a^2 - \phi_b^2), \quad (3.25)$$

where the dispersion is given by

$$\boldsymbol{\epsilon}_{\mathbf{k}}^0 = \frac{c_a}{4q_1^2} (k_a^2 - q_1^2)^2 + c_b k_b^2 + \tau \quad (3.26)$$

with

$$q_1 = 2 \cos^{-1} \left(-\frac{J_1}{2J_{2a}} \right), \quad (3.27a)$$

$$c_a = \frac{J_{2a}(4J_{2a}^2 - J_1^2)}{2(J_1^2 + 2J_{2a}(J_{2a} + J_{2b}))^2}, \quad (3.27b)$$

$$c_b = \frac{J_{2a}(J_1^2 + 4J_{2a}J_{2b})}{2(J_1^2 + 2J_{2a}(J_{2a} + J_{2b}))^2}, \quad (3.27c)$$

$$D = \frac{1}{A_a} + \frac{1}{A_b}, \quad (3.27d)$$

$$D_{ab} = \frac{1}{2} \left(\frac{1}{A_a} - \frac{1}{A_b} \right), \quad (3.27e)$$

$$\tau = \frac{2J_{2a}}{J_1^2 + 2J_{2a}(J_{2a} + J_{2b})} - D. \quad (3.27f)$$

The vanishing of τ controls the PM to AFM transition.

Taking the continuum limit of the single-ion anisotropy terms ins more subtle in the magnetically modulated spin spiral and bi-collinear states, as it oscillates and naively averages to zero. However, for a magnetic modulation wavevector k_1 close to the reciprocal lattice vector of crystal lattice, there is a tendency of the magnetically modulated state to lock to the crystal lattice.

To capture this physics, we use Poisson summation formula to convert a summation over lattice vector \vec{R}_n to integration, retaining the underlying discreteness.

$$\frac{1}{V} \sum_{\vec{G}_n} e^{i\vec{G}_n \cdot \mathbf{r}} = \sum_{\vec{R}_n} \delta^{(d)}(\mathbf{r} - \vec{R}_n) \quad (3.28)$$

where \vec{G}_n is a reciprocal vector and L is the periodicity.

Applying this to the single-ion anisotropy, we find

$$\mathcal{H}_{\text{pin}} = \sum_i D_{ab} \left((\phi_i^a)^2 - (\phi_i^b)^2 \right) \quad (3.29a)$$

$$= \frac{1}{V} \sum_m \int d\mathbf{r} D_{ab} (\phi_a^2 - \phi_b^2) e^{2\pi i m x_a / a_0} \quad (3.29b)$$

$$\simeq \frac{1}{V} \int d\mathbf{r} D_{ab} (\phi_a^2 - \phi_b^2) (1 + 2 \cos(q_0 x_a)) \quad (3.29c)$$

where wavevector $q_0 = \frac{2\pi}{a_0}$ is the lowest reciprocal lattice vector, with a_0 the lattice constant along x_a axis, V the volume of the system. We note that we only kept the lowest harmonic, with higher ones weaker and also assumed incommensurate with the k_1 modulation of the magnetic order.

Combining the above analysis, we obtain the effective Hamiltonian in continuum limit up to quadratic order,

$$\mathcal{H}_{\text{eff}} = \frac{1}{2} \sum_{\sigma=a,b} \phi_\sigma \hat{\epsilon} \phi_\sigma + D_{ab} (\phi_a^2 - \phi_b^2) \cos(q_0 a) \quad (3.30)$$

where

$$\hat{\epsilon} = \frac{c_a}{4q_1^2} (-\partial_a^2 - q_1^2)^2 - c_b \partial_b^2 - c_z \partial_z^2 + \tau \quad (3.31)$$

and we included z axis contribution from the interaction, $J_z \mathbf{S}_{i,z} \cdot \mathbf{S}_{i,z+1}$, which does not crucially contribute in the present analysis.

3.2.3 Magnetoelastic coupling for the single-ion anisotropy

We supplement our model with the magnetoelastic coupling, that provides a structural distortion mechanism for the single-ion anisotropy.

A general elastic energy density (up to quadratic terms) with 2-dimensional square symmetry is given by

$$\mathcal{H}_{\text{el}} = \frac{1}{2} [K_{11}(u_{xx}^2 + u_{yy}^2) + K_{12}u_{xx}u_{yy} + 2K_{44}u_{xy}^2] \quad (3.32)$$

where K_{11} , K_{12} , K_{44} are bulk and shear moduli and $u_{\sigma\sigma'}$ are elastic strain tensors. Anticipating the proximity to the tetragonal to orthorhombic structural transition, it is convenient to express \mathcal{H}_{el} in ab coordinates, rotated by $\pi/4$ relative to xy coordinates using matrix R ,

$$R = \frac{1}{\sqrt{2}} \begin{pmatrix} 1 & -1 \\ 1 & 1 \end{pmatrix}. \quad (3.33)$$

The transformed strain tensor is then given by

$$U^{ab} = \begin{pmatrix} u_{aa} & u_{ab} \\ u_{ab} & u_{bb} \end{pmatrix} = RU^{xy}R^T = R \begin{pmatrix} u_{xx} & u_{xy} \\ u_{xy} & u_{yy} \end{pmatrix} R^T \quad (3.34)$$

with

$$u_{xx} = \frac{1}{2}(u_{aa} + u_{bb} + 2u_{ab}) \quad (3.35a)$$

$$u_{yy} = \frac{1}{2}(u_{aa} + u_{bb} - 2u_{ab}) \quad (3.35b)$$

$$u_{xy} = \frac{1}{2}(-u_{aa} + u_{bb}). \quad (3.35c)$$

Using these relations inside Eq. (3.32) gives

$$\mathcal{H}_{\text{el}} = \frac{1}{2} \left[\left(\frac{1}{2}K_{11} + \frac{1}{4}K_{12} + \frac{1}{2}K_{44} \right) (u_{aa}^2 + u_{bb}^2) + \left(K_{11} + \frac{1}{2}K_{12} - K_{44} \right) u_{aa}u_{bb} + (2K_{11} - K_{12}) u_{ab}^2 \right] \quad (3.36a)$$

$$= \frac{1}{2} [K'_{11}(u_{aa}^2 + u_{bb}^2) + K'_{12}u_{aa}u_{bb} + K'_{44}u_{ab}^2] \quad (3.36b)$$

with transformed bulk and shear modulus K'_{11} , K'_{12} , and K'_{44} . For the tetragonal to orthorhombic transition $u_{xy} \neq 0$ and $u_{xx} = u_{yy} = 0$. Equivalently, we take $-u_{aa} = u_{bb} = u_0$ and $u_{ab} = 0$, reducing

the elastic energy to

$$\mathcal{H}_{\text{el}} = \frac{1}{2} [2K'_{11}u_0^2 - K'_{12}u_0^2] \quad (3.37\text{a})$$

$$= \left(K'_{11} - \frac{1}{2}K'_{12} \right) u_0^2 \quad (3.37\text{b})$$

$$= K_{44}u_0^2 \quad (3.37\text{c})$$

Including elastic nonlinearities the magneto-elastic Hamiltonian is given by

$$H = \frac{B}{2}u_{xy}^2 + \frac{\lambda}{4}u_{xy}^4 - \alpha S_i U_{ij} S_j + g_{12}u_{xy}^2 \mathbf{S}^2 \quad (3.38)$$

where $B = 2K_{44}$ and the elastic strain tensor U is given by

$$U = \begin{pmatrix} 0 & u_{xy} \\ u_{xy} & 0 \end{pmatrix}. \quad (3.39)$$

Or equivalently in the ab coordinates, the magnetoelastic (α) term coupling is given by

$$-\alpha \begin{pmatrix} S_a & S_b \end{pmatrix} R U R^{-1} \begin{pmatrix} S_a \\ S_b \end{pmatrix} = -\alpha u_{aa}(S_a)^2 - \alpha u_{bb}(S_b)^2 \quad (3.40)$$

with $S_{a,b} = \frac{1}{\sqrt{2}}(S_x \mp S_y)$, with the Hamiltonian reducing to Then the magnetoelastic Hamiltonian in ab coordinate becomes,

$$H = \frac{B}{2}u_0^2 + \frac{\lambda}{4}u_0^4 - \alpha u_0(S_a^2 - S_b^2) + g_{12}u_0^2 \mathbf{S}^2 \quad (3.41)$$

that after a structural transition to the orthorhombic state (characterized by $u_0 > 0$) leads to the single-ion anisotropy of the previous section.

3.3 Magnetostructural transition

We now turn to a mean-field analysis of the magnetostructural transition of FeTe based on the above Landau theory similar to Paul *et al.* [147].

In Fe_{1+y}Te , the structural transition from tetragonal to orthorhombic (for high doping) or monoclinic (for low doping) is accompanied by the magnetic transition and as a result is naturally

first order. However, in other iron pnictides the structural transition is observed to precede the magnetic transition. As we demonstrate below, our model captures both possibilities depending on the value of Landau parameters.

We begin with the Ginzburg-Landau free energy density, \mathcal{F}_{GL} ,

$$\mathcal{F}_{\text{GL}} = \mathcal{F}_{\text{M}} + \mathcal{F}_{\text{E}} + \mathcal{F}_{\text{ME}}, \quad (3.42\text{a})$$

$$\mathcal{F}_{\text{M}} = \psi^* \hat{\epsilon} \psi + r |\psi|^2 + \frac{g}{2} |\psi|^4, \quad (3.42\text{b})$$

$$\mathcal{F}_{\text{E}} = \frac{B}{2} u_{xy}^2 + \frac{\lambda}{4} u_{xy}^4, \quad (3.42\text{c})$$

$$\mathcal{F}_{\text{ME}} = -\frac{1}{2} \alpha (\psi^2 + \psi^{*2}) u_{xy} + g_{12} |\psi|^2 u_{xy}^2, \quad (3.42\text{d})$$

where anticipating an easy-plane anisotropy of FeTe (arising from the single-ion anisotropy in model (3.5)), we specialized to an xy order parameter $\psi = \psi_a + i\psi_b$ and $\hat{\epsilon}$ is given in Eq. (3.31). We take all (phenomenological) couplings to be positive except r and B which can change sign at the structural and magnetic transitions.

The corresponding saddle point equations are given by

$$0 = \frac{\partial \mathcal{F}_{\text{GL}}}{\partial \psi^*} \quad (3.43\text{a})$$

$$= r\psi + g|\psi|^2\psi - \alpha\psi^*u_{xy} + g_{12}\psi u_{xy}^2 \quad (3.43\text{b})$$

$$0 = \frac{\partial \mathcal{F}_{\text{GL}}}{\partial u_{xy}} \quad (3.43\text{c})$$

$$= Bu_{xy} - \frac{1}{2}\alpha(\psi^2 + \psi^{*2}) + 2g_{12}|\psi|^2u_{xy} + \lambda u_{xy}^3. \quad (3.43\text{d})$$

We firstly observe that this general magnetoelastic coupling requires that a nonzero magnetic order always induces a structural distortions as it is coupled linear to it. Thus, a tetragonal phase with magnetic order is generically not allowed. Then, this model generically admits the following three phases:

(1) Tetragonal paramagnet, $\text{PM}_{\text{T}} : \psi = 0, u_{xy} = 0,$

(2) Orthorhombic paramagnet, $\text{PM}_{\text{O}} : \psi = 0$ and $u_{xy} \neq 0$

(3) Orthorhombic commensurate or incommensurate AFM spiral, $\text{AFM}_O : \psi \neq 0$ and $u_{xy} \neq 0$

We now map out the corresponding phase diagram. The PM_T phase appears for $B > 0$ and $r > 0$.

For $B < 0$ and $r > 0$, the system enters PM_O state, characterized by order parameters,

$$\psi = 0 \quad (3.44a)$$

$$u_{xy} = \sqrt{-\frac{B}{\lambda}}. \quad (3.44b)$$

The PM_T - PM_O phase boundary is therefore given by $B = 0$ and $r > 0$.

On the other hand, for large $B > 0$, $u_{xy} = 0$ is minimum of \mathcal{F}_E , giving $r = 0$ as the PM_T -AFM phase boundary at large positive B . To determine the phase boundaries for smaller $B > 0$, we eliminate (or equivalently integrate out) the strain u_{xy} in favor of ψ , via

$$u_{xy} \simeq \frac{\alpha}{B} |\psi|^2 \quad (3.45)$$

thereby obtaining an effective Landau free energy density inside PM_T

$$\mathcal{F}_{\text{PM}_T} \simeq r |\psi|^2 + \frac{1}{2} \left(g - \frac{\alpha^2}{B} \right) |\psi|^4 + \frac{g_6}{3} |\psi|^6 + \dots \quad (3.46)$$

where $g_6 = 3 \frac{\alpha^2 g_{12}}{B^2}$. For sufficiently large positive B (such that the $g > \alpha^2/B$) the PM_T -AFM transition remains continuous at $r = 0$. However, for $B < B_c(r = 0) = \alpha^2/g$ such that the quartic coupling turns negative, the transition is first-order at $r_c(B)$ determined by

$$\mathcal{F}_{\text{PM}_T}(\psi_0) = 0 \quad (3.47a)$$

$$\left. \frac{\partial \mathcal{F}_{\text{PM}_T}}{\partial \psi^*} \right|_{\psi=\psi_0} = 0 \quad (3.47b)$$

These give

$$|\psi_0|^2 = \frac{4r_c}{\frac{\alpha^2}{B} - g} \quad (3.48)$$

and a first-order transition boundary

$$r_c(B) = \frac{1}{16g_{12}} \left(\alpha - \frac{gB}{\alpha} \right)^2, \quad \text{for } B > 0. \quad (3.49)$$

Although this analysis is quantitatively only valid for sufficiently large $B > 0$, such that elastic nonlinearities remain small, the qualitative behaviour (upturn in the $r_c(B)$ boundary and the first-order nature of the transition) persists, as illustrated in Fig. 3.6.

In contrast, for $B < 0$ regime, u_{xy} spontaneously develops a nonzero expectation value, u_0 . For large negative B , u_0 is determined by balance of u_{xy}^2 and u_{xy}^4 terms while other terms are small in comparisons. This gives

$$u_0 \simeq \sqrt{-\frac{B}{\lambda}} \quad (3.50)$$

as before and phase boundary is given by (from the saddle point equation),

$$r_c(B) = \alpha \sqrt{-\frac{B}{\lambda}} - g_{12} \frac{B}{\lambda}, \quad \text{for (large) } B < 0 \quad (3.51)$$

However for small negative B , the term linear in u_{xy} is more dominant than u_{xy}^2 term. Therefore $u_0 \simeq (\frac{\alpha}{\lambda} |\psi|^2)^{1/3}$ and the effective free energy density is given by

$$\mathcal{F}_{\text{PM}_0} \simeq r |\psi|^2 + \frac{1}{2} g |\psi|^4 + \frac{B}{2} \left(\frac{\alpha}{\lambda}\right)^{2/3} |\psi|^{4/3} - \frac{3\lambda}{4} \left(\frac{\alpha}{\lambda}\right)^{4/3} |\psi|^{8/3}. \quad (3.52)$$

from which we find the first order transition as in Fig. 3.6. Combining the above analysis, we obtain the phase diagram in Fig. 3.6.

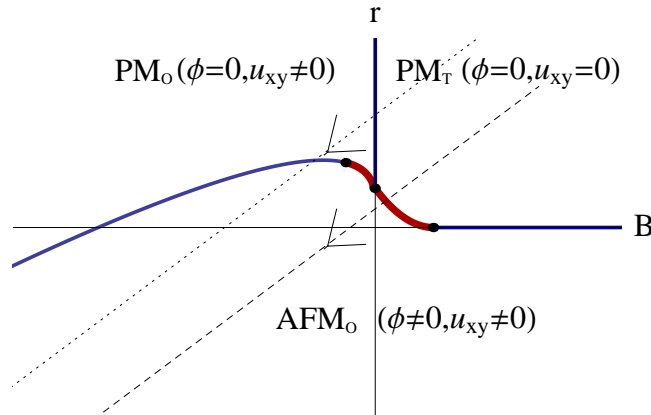


Figure 3.6: The global phase diagram in the reduced exchange, r and bulk modulus B plane. For low Fe doping, experiments [45, 46, 139] suggest that the reducing temperature takes the system across the first-order phase boundary in the positive $r - B$ quadrant, leading to a simultaneous orthorhombic distortion and development of bi-collinear magnetic order.

For low Fe doping experiments of Fe_{1+y}Te [45, 46, 139] suggest that the reducing temperature takes the system across the first-order phase boundary in the positive $r - B$ quadrant of phase diagram in Fig. 3.6. This leads to a simultaneous orthorhombic distortion and development of bi-collinear magnetic order. In contrast, FeAs compounds which exhibit distinct continuous structural and magnetic transitions, are accommodated by the phase diagram by a temperature path through continuous phase boundary.

3.4 Ordered state and commensurate-incommensurate transition

Another interesting observation in the phenomenology of Fe_{1+y}Te is the commensurate-incommensurate transition in the magnetically-ordered state which is observed to take place near $y_c \simeq 0.12$. To address this phenomenon, here we derive an effective model of the ordered state. We then use it to demonstrate the existence of a CI transition, driven by a competition between the exchange interaction (with preferred wavevector k_1) and single-ion lattice pinning (to a wavevector k_0).

To this end we utilize the Hubbard-Stratonovich derivation of Sec. 3.2, but this time introducing two basis sublattice to capture the bi-collinear state and its low-energy deformations.

We parametrize incommensurate bi-collinear state by expanding ϕ_i around a commensurate bi-collinear state, Eq. (3.11), in terms of the incommensurate (bi-collinearly) staggered magnetization ψ_i

$$\phi_\mu(\mathbf{r}_i) = e^{i\frac{\pi}{2}(x_i - y_i)} (-i)^\mu \psi_\mu(\mathbf{r}_i), \quad (3.53)$$

that varies slowly on each sublattice. We therefore characterize ψ by two-sublattice spirals fields ψ_μ , with wavevector $\mathbf{k}_0 = k_0 \hat{a} = \frac{\pi}{2}(\hat{x} - \hat{y}) = \pi \hat{a}$, where the sub-lattice index μ denotes A and B. In terms of the field ψ_μ , the quadratic part of the continuum Hamiltonian density is given by

$$\mathcal{H}_0[\psi] = \sum_{\mu=0,1} D_{ab} \left((\psi_\mu^a)^2 - (\psi_\mu^b)^2 \right) + \sum_{\mu=0,1} \frac{1}{2} \psi_\mu^\alpha (\tau - c_a \partial_a^2 - c_b \partial_b^2) \psi_\mu^\alpha + c_{ab} \psi_A^\alpha (i \partial_a) \psi_B^\alpha, \quad (3.54)$$

in which, $\mu = 0, 1$ correspond to two sublattices A and B, respectively, and, τ , c_a , c_b , and $c_{ab} = 2c_a k_0$ are given in Eq. (3.27). The new coordinates are defined as $X = (x + y)/\sqrt{2}$, $Y = (x - y)/\sqrt{2}$ (see

Fig. 3.2). The quartic field contribution is given by

$$\mathcal{H}_4[\psi] = \sum_{\mu} \left[\frac{(\psi_{\mu}^a)^4}{A_b^3} + \frac{(\psi_{\mu}^b)^4}{A_a^3} + \frac{(\psi_{\mu}^a)^2(\psi_{\mu}^b)^2}{A_a A_b} \left(\frac{1}{A_a} + \frac{1}{A_b} \right) - \frac{(\psi_{\mu}^z)^2}{A_a A_b} \left(\frac{(\psi_{\mu}^a)^2}{A_b} + \frac{(\psi_{\mu}^b)^2}{A_a} \right) \right]. \quad (3.55)$$

The structure of the ground state is determined by the lowest eigenvalue and eigenvector of the quadratic part of the Hamiltonian. As discussed in Sec. 3.2, in the absence of single-ion anisotropy (i.e., in the tetragonal symmetry phase), it is given by the incommensurate bi-collinear state that we parametrize as

$$\psi_A = \psi_0 \text{Re}[(\hat{X} - i\hat{Y})e^{i(QX + \theta x)}] \quad (3.56a)$$

$$\psi_B = \psi_0 \text{Re}[-\hat{Y} - i\hat{X})e^{i(QX + \theta x)}]. \quad (3.56b)$$

with Q determined by minimization of the lowest eigenvalue of the quadratic dispersion for $D_{ab} = 0$.

We find that it is given by

$$\frac{d}{dQ} [\epsilon_Q^2 - c_{ab}^2 Q^2] = 0 \quad (3.57)$$

which gives

$$Q = \sqrt{2k_0^2 - \tau} \quad (3.58)$$

and θ is arbitrary Goldstone mode for $D_{ab} = 0$, and ψ_0 is determined by minimization of the energy along with quartic terms.

In terms of this representation the single-ion anisotropy part of the Hamiltonian reduces to:

$$H_{\text{ani}} = -D_{ab} \psi_0^2 \cos(2Qx + 2\theta) \quad (3.59)$$

In the ordered state, the energy density reduces to

$$f = \frac{\kappa}{2} (\partial_x \theta)^2 - g \cos(2\theta + 2QX) \quad (3.60)$$

$$= \frac{\kappa}{2} (\partial_X \varphi)^2 - \kappa Q \partial_a \varphi + \frac{\kappa}{2} Q^2 - g \cos(2\varphi) \quad (3.61)$$

with $\varphi = \theta + Qx$, $\kappa = \frac{c_a}{2} \psi_0^2$, $g = \frac{\psi_0^4}{4} (A_a^{-1} + A_b^{-1})(A_a^{-1} - A_b^{-1})^2$. This is a standard sine-Gordon model.

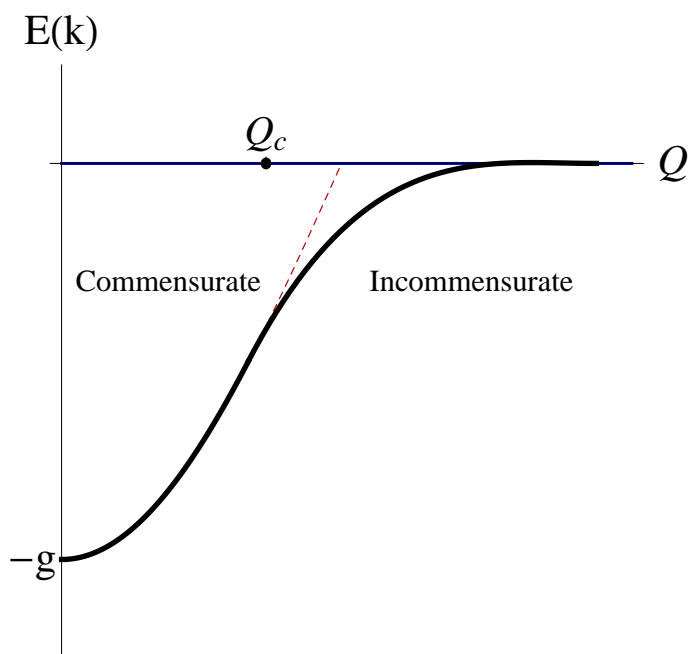


Figure 3.7: Energy ($E(k)$) as a function of momentum Q in commensurate-incommensurate transition in φ representation of Eq. (3.61). Q_c represents the CI transition point.

The sine-Gordon model with a twist Q exhibits a well-known CI transition between a phase where pinning g dominates with $\varphi_C = 0$ and an incommensurate phase where elasticity dominates leading to proliferation of domain walls at

$$Q_c = \frac{2}{\pi\xi} = \frac{4}{\pi} \sqrt{\frac{g}{\kappa}}, \quad (3.62)$$

of width $\xi = \frac{1}{2} \sqrt{\frac{\kappa}{g}}$ that corresponds to an incommensurate state that asymptotically gives $\phi_I = Qx$. For $Q < Q_c$, the system is in the bi-collinear state with $\varphi = -Qx/2$. On the other hand when $Q > Q_c$, the system becomes incommensurate state where solitons (domain-walls) proliferate with $\varphi = 0$ at large Q . We can analyze the static structure function of these two states in the following way.

3.4.1 Dynamic structure function in the soliton regime

As we have demonstrated in the previous section 3.4, the commensurate-incommensurate transition is governed by a following Hamiltonian

$$H = \int \left[\frac{1}{2} \kappa (\nabla \theta)^2 - g \cos(2\theta + 2QX) \right], \quad (3.63)$$

$$= \int \left[\frac{1}{2} \kappa ((\nabla \varphi)^2 - 2Q \partial_a \varphi) - g \cos 2\varphi \right], \quad (3.64)$$

where $Q = q_1 - q_0/2$ and κ and g are given in Section 3.4. The model exhibits CI transition at a critical value of incommensurability

$$Q_c = \frac{1}{\pi\xi} = \frac{2}{\pi} \sqrt{\frac{g}{\kappa}} \quad (3.65)$$

$$\xi = \frac{1}{2} \sqrt{\frac{\kappa}{g}} \quad (3.66)$$

between a commensurate state $\theta = 0 (\varphi = -Qa)$, corresponding to a spin density wave at $\mathbf{q} = \frac{1}{2} q_0 \hat{a}$ and an incommensurate state, where solitons (domain-walls) proliferate, at large Q asymptotically leading to $\theta_\infty = Qa (\varphi = 0)$, corresponding to a spin density wave at $\mathbf{q} = q_1 \hat{a}$. The average tilt is $\bar{\theta}(a) = qa$, where $q(Q) \simeq \pi/d = \pi n_s(Q)$, where d, n_s is soliton spacing and density, respectively. In the dilute soliton limit (close to Q_c), $\xi \ll d$ can be taken to be zero and as can be seen from

Fig. 3.9 $\delta\theta(a) = \theta(a) - qa$ becomes simply a linear function

$$\delta\theta(a) = -\frac{\pi}{d}(a - d/2), \quad \text{for } 0 < x \leq d, \quad (3.67)$$

periodically extended.

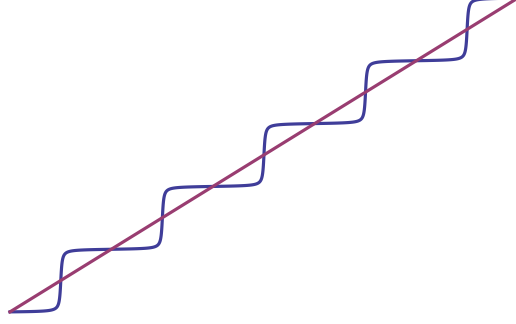


Figure 3.8: $\theta(x)$ (Elliptic integral of the second kind) displaying a train of domain walls in the incommensurate state, just above Q_c , as well as the average tilted form $\bar{\theta}(x) = qx$.

At $T = 0$, the structure function $I(k)$ can be straightforwardly computed

$$I(k) = \text{Re} \int_{-\infty}^{\infty} dx e^{-i\mathbf{k}\cdot\mathbf{x}} \langle e^{i\frac{1}{2}q_0x + i\theta(\mathbf{r}) - i\theta(0)} \rangle. \quad (3.68)$$

In the incommensurate phase, at zero temperature

$$I_I(k) \simeq \text{Re} \int_{-\infty}^{\infty} dx e^{i(\frac{1}{2}q_0 + q)x - i\mathbf{k}\cdot\mathbf{x} + i\delta\theta(\mathbf{x})} \quad (3.69)$$

We note that at large Q , $q \rightarrow Q = q_1 - \frac{1}{2}q_0$, reducing the SDW peak from the commensurate $\frac{1}{2}q_0$ to the incommensurate q_1 wavevector, and the structure function becomes a Bragg peak δ -function at q_1 .

For intermediate values of $Q > Q_c$, it is simply a Fourier transform of $e^{i\delta\theta(\mathbf{x})}$, that can be easily taken in the above linear (saw-tooth) approximation. Let us take $x = d(n + \tau/2\pi)$, we find

$$I_I(k) \simeq \frac{d}{2\pi} \text{Re} \sum_{-\infty}^{\infty} e^{i(\frac{1}{2}q_0 + q - k)dn} \int_0^{2\pi} d\tau e^{i\frac{d}{2\pi}(\frac{1}{2}q_0 + q - k)\tau - i\frac{1}{2}(\tau - \pi)}, \quad (3.70)$$

$$\simeq \sum_p \delta(k - \frac{1}{2}q_0 - q - 2\pi p/d) 2\text{Re} \int_0^\pi d\tau e^{-ip\tau - i\frac{1}{2}(\tau - \pi)}, \quad (3.71)$$

$$\simeq \sum_p \frac{4}{2p+1} \delta(k - \frac{1}{2}q_0 - q - 2\pi p/d) \quad (3.72)$$

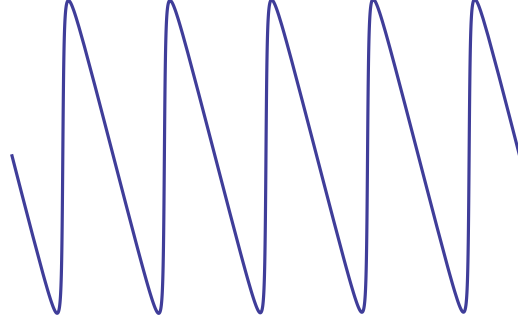


Figure 3.9: A train of domain walls in the incommensurate state, $\delta\theta = \theta(x) - \bar{\theta}(x)$, just above Q_c , after $\bar{\theta}(x) = qx$ has been subtracted.

Thus, as anticipated, just above Q_c the appearance of solitons leads to higher harmonic x-ray peaks at $q_p = 2\pi p/d$, with the amplitude $A_p = 4/(2p + 1)$.

At finite temperature, fluctuations about $\theta_s(x)$ need to be included. However, because of these fluctuations are described by an xy -model (because spatial rotational invariance is explicitly broken), we expect that in 3d these fluctuations are finite and lead to a finite Debye-Waller factor suppressing the amplitude of these Bragg peaks but leaving them sharp at the limit of the resolution (or due to disorder). Generalization of this analysis to a dynamic structure function may be of interest in comparing with inelastic neutron scattering.

We next turn our attention to the dynamic properties of Fe_{1+y}Te .

3.5 Structure function for Fe_{1+y}Te

We now study the dynamics of Fe_{1+y}Te in the ordered bi-collinear ($T < T_N$) and disordered paramagnetic ($T > T_N$) states. Our main motivation is to understand the recently measured dynamic structure function of Fe_{1+y}Te from inelastic neutron scattering (INS) experiment by Parshall *et al.* [143] focused on the regime near T_N . Studying $\text{Fe}_{1.08}\text{Te}$, which shows a commensurate bi-collinear order at lower temperature, they found that above $T_N = 67.5\text{K}$, the inelastic scattering controlled by spin-wave fluctuations is peaked at an incommensurate wavevector, $\mathbf{q}_{\text{inc}} = [0.45, 0, 0.5]$ and zero frequency (Note that we use the notation from Parshall *et al.* [143]). Furthermore, in the ordered state the excitation gap near $E = 6$ meV is also observed consistent with other experiments.

With these experiments performed in a relatively higher temperature regime, i.e. near T_N , we utilize a hydrodynamic description based on Halperin and Hohenberg's work on the planar magnet, extending it to spiral states of Fe_{1+y}Te and finding qualitative agreement with experiments [143].

3.5.1 Static structure function in paramagnetic state, PM_O

Before turning to the calculation of the dynamic structure function, it is instructive to compute the static structure function in the orthorhombic paramagnetic PM_O state just above the transition to the bi-collinear planar spiral state. We note that although in Fe_{1+y}Te this PM_O phase has not been observed (as it undergoes a direct first-order transition from PM_T to AFM_O), as discussed above and illustrated in the phase diagram of Fig. 3.6, generically it is allowed and has been observed in other materials [148, 149]. This static structure computation elucidates the competition between the incommensurate spiral state selected by the exchange interaction and the commensurate state imposed by the single-ion anisotropy.

Motivated by microscopic description in Sec. 3.2, we utilize an effective continuum model, with quadratic part of the Hamiltonian density given by

$$\mathcal{H}_0 = \sum_{\sigma=a,b,z} S_\sigma \hat{\epsilon} S_\sigma + D_{ab}(S_a^2 - S_b^2) \cos(q_0 X) \quad (3.73)$$

where the dispersion is given by

$$\hat{\epsilon} = \frac{c_a}{4q_1^2} (-\partial_a^2 - q_1^2)^2 - c_b \partial_b^2 - c_z \partial_z^2 + \tau. \quad (3.74)$$

As discussed in the above, for weak anisotropy, the ordering is into a coplanar spiral state² given by

$$\mathbf{S} = \text{Re} \left[\psi (\hat{a} - i\hat{b}) e^{iq_1 X} \right] \quad (3.75)$$

where $q_1 = 2 \cos^{-1}(-\frac{J_1}{2J_{2a}})$ minimizes the exchange dispersion. The complex spiral order parameter

² Here for simplicity we focus on single, two-sublattice spiral.

ψ encodes the dominant fluctuations near T_N . In terms of it, the \mathcal{H}_0 reduces to

$$\mathcal{H}_0 = \sum_k \epsilon_{\mathbf{k}} |\psi|^2 + \frac{1}{2} D_{ab} (\psi^2 e^{2iq_1 X} + c.c.) \cos(q_0 X) \quad (3.76)$$

$$= \frac{1}{2} \sum_k \begin{pmatrix} \psi^* & \psi \end{pmatrix} \begin{pmatrix} \epsilon_{\mathbf{k}} & D_{ab} e^{iQX} \\ D_{ab} e^{-iQX} & \epsilon_{\mathbf{k}} \end{pmatrix} \begin{pmatrix} \psi \\ \psi^* \end{pmatrix} \quad (3.77)$$

where

$$\epsilon_{\mathbf{k}} = c_a k_a^2 + c_b k_b^2 + c_z k_z^2 + \tau \quad (3.78)$$

$$Q = q_0 - 2q_1. \quad (3.79)$$

Above matrix form is easily diagonalized and, using $\psi(\mathbf{r}) = \frac{1}{\sqrt{N}} \sum_k \psi_{\mathbf{k}} e^{i\mathbf{k}\cdot\mathbf{r}}$, straightforward analysis gives,

$$\mathcal{H}_0 = \frac{1}{2} \sum_k [E_{\mathbf{k}}^+ |\psi_{\mathbf{k}}^+|^2 + E_{\mathbf{k}}^- |\psi_{\mathbf{k}}^-|^2] \quad (3.80)$$

where

$$\begin{pmatrix} \psi_{\mathbf{k}+\mathbf{q}_{\Delta}/2} \\ \psi_{-\mathbf{k}+\mathbf{q}_{\Delta}/2}^* \end{pmatrix} = \begin{pmatrix} u_{\mathbf{k}} & -v_{\mathbf{k}}^* \\ v_{\mathbf{k}} & u_{\mathbf{k}}^* \end{pmatrix} \begin{pmatrix} \psi_{\mathbf{k}}^+ \\ \psi_{\mathbf{k}}^- \end{pmatrix} = \begin{pmatrix} u_{\mathbf{k}} \psi_{\mathbf{k}}^+ - v_{\mathbf{k}}^* \psi_{\mathbf{k}}^- \\ v_{\mathbf{k}} \psi_{\mathbf{k}}^+ + u_{\mathbf{k}}^* \psi_{\mathbf{k}}^- \end{pmatrix}. \quad (3.81)$$

The coefficients, $u_{\mathbf{k}}$ and $v_{\mathbf{k}}$, are given by

$$u_{\mathbf{k}} = \sqrt{\frac{1}{2} \left(1 + \frac{\epsilon_{\mathbf{k}-}}{E_{\mathbf{k}}} \right)}, \quad v_{\mathbf{k}} = \sqrt{\frac{1}{2} \left(1 - \frac{\epsilon_{\mathbf{k}-}}{E_{\mathbf{k}}} \right)} \quad (3.82)$$

where

$$\epsilon_{\mathbf{k}\pm} = \frac{1}{2} (\epsilon_{\mathbf{k}+\frac{\mathbf{q}_{\Delta}}{2}} \pm \epsilon_{-\mathbf{k}+\frac{\mathbf{q}_{\Delta}}{2}}) \quad (3.83a)$$

$$E_{\mathbf{k}} = \sqrt{\epsilon_{\mathbf{k}-}^2 + D_{ab}^2} \quad (3.83b)$$

$$E_{\mathbf{k}}^{\pm} = \epsilon_{\mathbf{k}\pm} \pm E_{\mathbf{k}}. \quad (3.83c)$$

Expressing $S_{\mathbf{k}}$ in terms of these normal modes

$$S_{\mathbf{k}} = \frac{1}{2} (v_{\mathbf{k}+\frac{\mathbf{q}_0}{2}}^* \psi_{\mathbf{k}+\frac{\mathbf{q}_0}{2}}^{+*} + u_{\mathbf{k}+\frac{\mathbf{q}_0}{2}} \psi_{\mathbf{k}+\frac{\mathbf{q}_0}{2}}^{-*} + u_{\mathbf{k}-\frac{\mathbf{q}_0}{2}}^* \psi_{\mathbf{k}-\frac{\mathbf{q}_0}{2}}^{+*} - v_{\mathbf{k}-\frac{\mathbf{q}_0}{2}} \psi_{\mathbf{k}-\frac{\mathbf{q}_0}{2}}^{-*}). \quad (3.84)$$

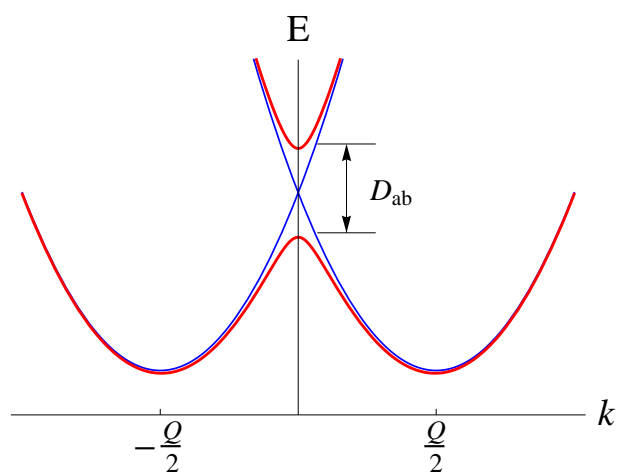


Figure 3.10: The spectra showing two shifted parabolas hybridized weakly (in proportion to D_{ab}) at their crossings.

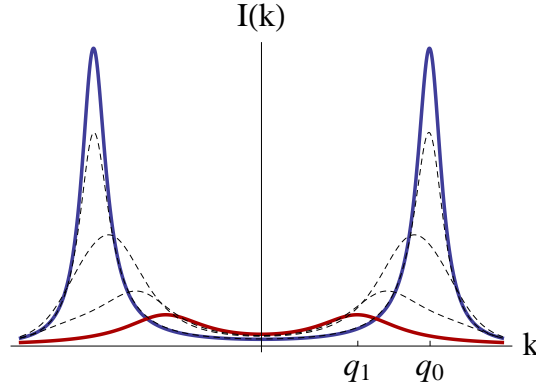


Figure 3.11: The static structure function where the shift of peaks from incommensurate wavevector q_1 (red line) to commensurate wavevector $q_0/2$ (blue line) are shown. The dashed lines are the value in between. The plot is drawn in arbitrary unit.

and using equipartition for the correlation function of the normal modes in the PM state, we obtain the static structure function for $T > T_N$

$$I_k(k) = \langle S_k^* S_k \rangle \quad (3.85a)$$

$$= \frac{k_B T}{2} \left[\frac{|v_{\mathbf{k}+\frac{\mathbf{q}_0}{2}}|^2}{E_{\mathbf{k}+\frac{\mathbf{q}_0}{2}}^+} + \frac{|u_{\mathbf{k}+\frac{\mathbf{q}_0}{2}}|^2}{E_{\mathbf{k}+\frac{\mathbf{q}_0}{2}}^-} + \frac{|u_{\mathbf{k}-\frac{\mathbf{q}_0}{2}}|^2}{E_{\mathbf{k}-\frac{\mathbf{q}_0}{2}}^+} + \frac{|v_{\mathbf{k}-\frac{\mathbf{q}_0}{2}}|^2}{E_{\mathbf{k}-\frac{\mathbf{q}_0}{2}}^-} \right] \quad (3.85b)$$

$$= \frac{k_B T}{4} \left[\frac{\epsilon_{(\mathbf{k}+\frac{\mathbf{q}_0}{2})+\frac{\mathbf{q}_\Delta}{2}}}{E_{\mathbf{k}+\frac{\mathbf{q}_0}{2}}^+ E_{\mathbf{k}+\frac{\mathbf{q}_0}{2}}^-} + \frac{\epsilon_{-(\mathbf{k}-\frac{\mathbf{q}_0}{2})+\frac{\mathbf{q}_\Delta}{2}}}{E_{\mathbf{k}-\frac{\mathbf{q}_0}{2}}^+ E_{\mathbf{k}-\frac{\mathbf{q}_0}{2}}^-} \right]. \quad (3.85c)$$

3.5.2 Dynamic structure function in paramagnetic state, PM_O

We now turn to the computation of the dynamic structure function, first focusing on the paramagnetic state. Because the primary experiments [143] of our interest is corresponding to high temperature, we utilize a classical hydrodynamic description [150]. Standard symmetry arguments, together with nontrivial spin commutation relations lead to a model E hydrodynamics, described by Langevin equation,

$$\partial_t \phi = -\gamma \frac{\delta \mathcal{H}}{\delta \phi^*} - i\Gamma \phi \frac{\delta \mathcal{H}}{\delta m} + \zeta \quad (3.86)$$

$$\partial_t m = \lambda \nabla^2 \frac{\delta \mathcal{H}}{\delta m} + \Gamma \text{Im} \left(\phi^* \frac{\delta \mathcal{H}}{\delta \phi^*} \right) + \zeta_m \quad (3.87)$$

where $\phi = S_a - iS_b$, $m = S_z$, and Γ, γ, λ are coefficients related with the dynamics of the system. $\zeta = \zeta_a - i\zeta_b$ is a thermal Gaussian noise, i.e.

$$\langle \zeta_\sigma(t) \rangle = 0 \quad (3.88)$$

$$\langle \zeta_\sigma(t) \zeta_{\sigma'}(t') \rangle = 2\gamma k_B T \delta_{\sigma\sigma'} \delta(t - t'). \quad (3.89)$$

where the structure of the variances imposed by the fluctuation-dissipation relation [150]. The equations consist of purely dissipative (relaxational) terms as well as the reactive parts that capture the spin precessional dynamics as studied extensively for numerous other magnetic systems. The new ingredient here is the spiral nature of the ordered state and the single-ion pinning anisotropy special to Fe_{1+y}Te .

In disordered paramagnetic state, we can take the harmonic approximation from which we can ignore the nonlinear precessional terms. Thus the equations of motion simplify to

$$\frac{\partial S_\sigma}{\partial t} = -\gamma \frac{\delta \mathcal{H}_0}{\delta S_\sigma} + \zeta_\sigma \quad (3.90)$$

and using Eq. (3.75) for the spin spiral state, we have

$$\frac{\partial}{\partial t} \begin{pmatrix} \psi \\ \psi^* \end{pmatrix} = -2\gamma \begin{pmatrix} \tilde{\epsilon}' & D_{ab} e^{iQX} \\ D_{ab} e^{-iQX} & \tilde{\epsilon}' \end{pmatrix} \begin{pmatrix} \psi \\ \psi^* \end{pmatrix} + \begin{pmatrix} \zeta^{q_1} \\ \zeta^{-q_1} \end{pmatrix} \quad (3.91)$$

where $\tilde{\epsilon}' = -c_a \partial_a^2 - c_b \partial_b^2 - c_z \partial_z^2 + \tau$ and $\zeta^{q_1}, \zeta^{-q_1}$ are independent Gaussian noise with

$$\langle \zeta_k(t) \zeta_{-k}(t') \rangle = 4\gamma k_B T \delta(t - t'). \quad (3.92)$$

After Fourier transformation, the susceptibility can be obtained straightforwardly,

$$\tilde{\chi} = \begin{pmatrix} -i\omega + 2\gamma \epsilon_{\mathbf{k}+\mathbf{Q}/2} & 2\gamma D_{ab} \\ 2\gamma D_{ab} & -i\omega + 2\gamma \epsilon_{-\mathbf{k}+\mathbf{Q}/2} \end{pmatrix}^{-1} \quad (3.93)$$

from which we can find

$$\psi(\mathbf{k} + \frac{\mathbf{q}_\Delta}{2}, \omega) = C \left[(-i\omega + 2\gamma \epsilon_{-\mathbf{k}+\frac{\mathbf{q}_\Delta}{2}}) \zeta_{\mathbf{k}+\frac{\mathbf{q}_\Delta}{2}} + 2\gamma D_{ab} \zeta_{\mathbf{k}-\frac{\mathbf{q}_\Delta}{2}} \right], \quad (3.94a)$$

$$\psi^*(-\mathbf{k} + \frac{\mathbf{q}_\Delta}{2}, -\omega) = C \left[2\gamma D_{ab} \zeta_{\mathbf{k}+\frac{\mathbf{q}_\Delta}{2}} + (-i\omega + 2\gamma \epsilon_{\mathbf{k}+\frac{\mathbf{q}_\Delta}{2}}) \zeta_{\mathbf{k}-\frac{\mathbf{q}_\Delta}{2}} \right] \quad (3.94b)$$

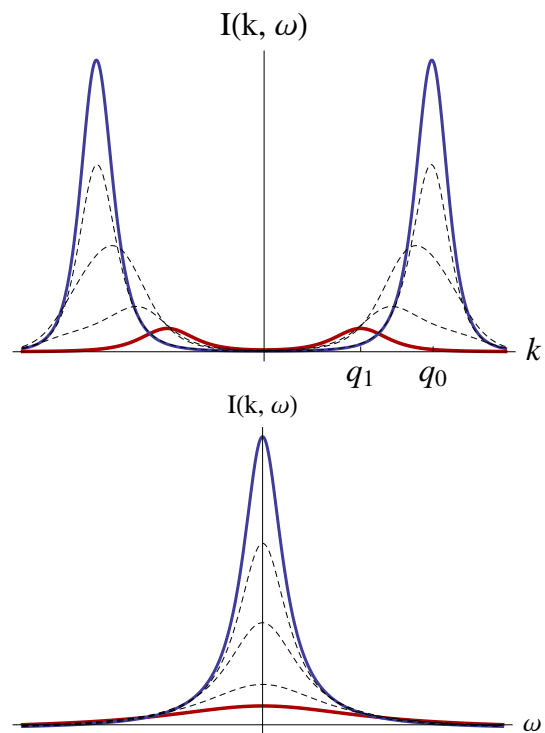


Figure 3.12: The dynamic structure function in function of k (top) and ω (bottom). We can see the shift of peaks from the incommensurate state (red) where D_{ab} is small to commensurate state (blue) where D_{ab} is large. The dashed lines are the value in between. The lorentzian peak at $\omega = 0$ represents the relaxational dynamics which is the main feature of disordered phase.

where $C = (-\omega^2 + 4\gamma^2(\varepsilon_{\mathbf{k}+}^2 - E_k^2 - i\omega\varepsilon_{\mathbf{k}+}/\gamma))^{-1}$. Now using (with $q_1 = \frac{1}{2}(q_0 - Q)$)

$$S_b(\mathbf{k}, \omega) = \frac{1}{2}(\psi_{\mathbf{k}-\mathbf{q}_1} + \psi_{-\mathbf{k}-\mathbf{q}_1}^*) \quad (3.95)$$

$$= \frac{1}{2}(\psi((\mathbf{k} - \frac{\mathbf{q}_0}{2}) + \frac{\mathbf{q}_\Delta}{2}, \omega) + \psi^*(-(\mathbf{k} + \frac{\mathbf{q}_0}{2}) + \frac{\mathbf{q}_\Delta}{2}, -\omega)) \quad (3.96)$$

the dynamic correlation function is

$$\begin{aligned} \langle S_b(\mathbf{k}, \omega) S_b(-\mathbf{k}, -\omega) \rangle &= \frac{1}{4} \langle \psi(\mathbf{k} - \frac{\mathbf{q}_0}{2} + \frac{\mathbf{q}_\Delta}{2}, \omega) \psi^*(\mathbf{k} - \frac{\mathbf{q}_0}{2} + \frac{\mathbf{q}_\Delta}{2}, \omega) \rangle \\ &\quad + \frac{1}{4} \langle \psi^*(-\mathbf{k} - \frac{\mathbf{q}_0}{2} + \frac{\mathbf{q}_\Delta}{2}, -\omega) \psi(-\mathbf{k} - \frac{\mathbf{q}_0}{2} + \frac{\mathbf{q}_\Delta}{2}, -\omega) \rangle \end{aligned} \quad (3.97)$$

$$\begin{aligned} &= \frac{\gamma k_B T (\omega^2 + 4\gamma^2(\varepsilon_{\mathbf{k}+\frac{\mathbf{q}_0}{2}+\frac{\mathbf{q}_\Delta}{2}}^2 + D_b^2))}{(-\omega^2 + 4\gamma^2(\varepsilon_{\mathbf{k}+\frac{\mathbf{q}_0}{2},+}^2 - E_{\mathbf{k}+\frac{\mathbf{q}_0}{2}}^2))^2 + (4\gamma\omega\varepsilon_{\mathbf{k}+\frac{\mathbf{q}_0}{2},+})^2} \\ &\quad + \frac{\gamma k_B T (\omega^2 + 4\gamma^2(\varepsilon_{-\mathbf{k}+\frac{\mathbf{q}_0}{2}+\frac{\mathbf{q}_\Delta}{2}}^2 + D_b^2))}{(-\omega^2 + 4\gamma^2(\varepsilon_{-\mathbf{k}+\frac{\mathbf{q}_0}{2},+}^2 - E_{-\mathbf{k}+\frac{\mathbf{q}_0}{2}}^2))^2 + (4\gamma\omega\varepsilon_{-\mathbf{k}+\frac{\mathbf{q}_0}{2},+})^2} \end{aligned} \quad (3.98)$$

We can easily obtain the static structure function by integrating over ω which verifies our calculation.

3.5.3 Dynamic structure function in planar spiral state

3.5.3.1 Order parameter structure

Before we move on to find the dynamic structure function, let us consider the order parameter structure in the ordered state first. As we discussed in Sec. 3.2, the order parameter in bi-collinear state is given by Eq. (3.11)

$$\psi_{A,i} = (-)^{(x_i - y_i)/2} \left(\frac{1}{\sqrt{2}}, \frac{1}{\sqrt{2}}, 0 \right), \quad (3.99)$$

$$\psi_{B,i} = (-)^{(x_i - y_i - 1)/2} \left(\frac{1}{\sqrt{2}}, \frac{1}{\sqrt{2}}, 0 \right) \quad (3.100)$$

and we need to consider the fluctuations from each lattice separately. When we focus on the low energy fluctuations, however, the optical modes (i.e., fluctuations out of phase between A and B components) can be ignored and ψ_A and ψ_B are simply related by $\psi \equiv \psi_A = \psi_B$, thus giving us essentially single fluctuation spiral order parameter.

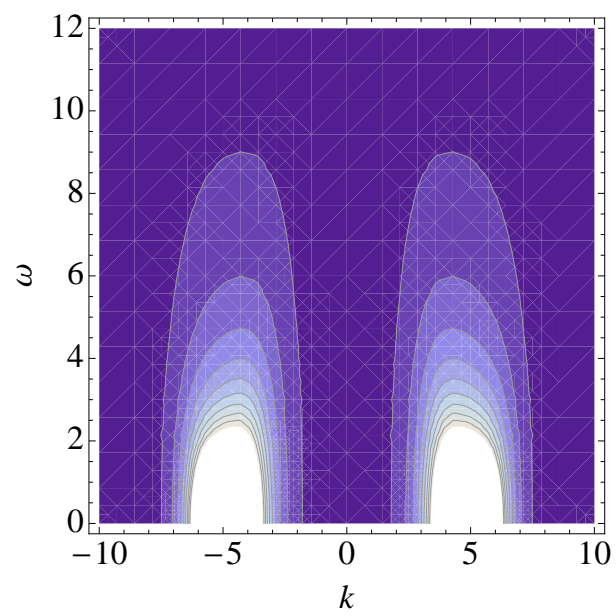


Figure 3.13: The dynamic structure function in disordered phase above the commensurate state in k and ω space.

Both commensurate or incommensurate spin-spiral state can be written as

$$\mathbf{S} = \text{Re}(\boldsymbol{\psi} e^{i\mathbf{q}\cdot\mathbf{r}}) \quad (3.101)$$

where \mathbf{q} represents commensurate or incommensurate ordering vector. For $\boldsymbol{\psi}$, there are two possible states, so called, ferromagnetic and polar states. Note that *ferromagnetic* does not literally means ferromagnetic order here.

For ferromagnetic state, $\boldsymbol{\psi}$ is written by,

$$\boldsymbol{\psi} = (\hat{n} + i\hat{m})e^{i\varphi} \quad (3.102)$$

where \hat{n} and \hat{m} are two real vectors with $\hat{n} \cdot \hat{m} = 0$. Therefore \mathbf{S} can be represented by,

$$\mathbf{S} = \hat{n} \cos(\mathbf{q} \cdot \mathbf{r} + \varphi) + \hat{m} \sin(\mathbf{q} \cdot \mathbf{r} + \varphi) \quad (3.103)$$

This describes the spin spiral in xy plane. Note that in general $\boldsymbol{\psi}$ is in $S^3 = S^2 \times U(1)$ space, with two Goldstone modes. However, we have an easy-plane in xy plane and $\hat{l} = \hat{n} \times \hat{m}$ is fixed at \hat{z} . Therefore the order parameter manifold effectively reduces from $S^3 \rightarrow SU(2)$ due to an easy-plane anisotropy. The Goldstone mode φ is the fluctuation of the spin direction (phase), which corresponds to the shift of spin spiral.

For polar state, $\boldsymbol{\psi}$ has a simpler form of

$$\boldsymbol{\psi} = \hat{n} e^{i\varphi} \quad (3.104)$$

Now there are two different Goldstone modes corresponding to the spin direction fluctuation and shift of spiral. In this case,

$$\mathbf{S} = \hat{n} \cos(\mathbf{q} \cdot \mathbf{r} + \varphi) \quad (3.105)$$

As we can see from above, the spin spiral is naturally described by ferromagnetic order parameter. Thus we expect the ferromagnetic order parameter is what we have in our system and the spin components can be represented by

$$S_a = S_0 \cos(\mathbf{q} \cdot \mathbf{r} + \varphi(\mathbf{r})) \quad (3.106a)$$

$$S_b = S_0 \sin(\mathbf{q} \cdot \mathbf{r} + \varphi(\mathbf{r})) \quad (3.106b)$$

with S_0 being constant. We also choose $\mathbf{r} = \hat{a}$ due to the crystal structural transition spontaneously chooses the direction of the order parameter.

3.5.3.2 Incommensurate phase

Now we study the dynamic structure function in ordered phase. Our Hamiltonian is given by Eq. (3.30) and we ignore the single-ion anisotropy for incommensurate phase since they are less dominant. Then the Hamiltonian becomes,

$$\mathcal{H}_{\text{eff}} = \sum_{\sigma=a,b} S_{\sigma} \hat{\epsilon} S_{\sigma} + \frac{1}{2\chi_m} m^2 \quad (3.107)$$

where we included m^2 term for z -directional response.

From model E [150], the Langevin equations are given by

$$\partial_t \phi = -\gamma \frac{\delta H}{\delta \phi^*} - i\Gamma \phi \frac{\delta H}{\delta m} + \zeta \quad (3.108)$$

$$\partial_t m = \lambda \nabla^2 \frac{\delta H}{\delta m} + \Gamma \text{Im} \left(\phi^* \frac{\delta H}{\delta \phi^*} \right) + \zeta_m \quad (3.109)$$

where $\phi = S_a - iS_b$ and Γ, γ, λ are coefficients related with the dynamics.

We can express the above equations of motion explicitly using our model in S_a and S_b ,

$$\partial_t S_a = -\gamma \hat{\epsilon} S_a - \Gamma \chi_m^{-1} S_b m + \zeta_a \quad (3.110a)$$

$$\partial_t S_b = -\gamma \hat{\epsilon} S_b + \Gamma \chi_m^{-1} S_a m + \zeta_b \quad (3.110b)$$

$$\partial_t m = \lambda \chi_m^{-1} \nabla^2 m - \Gamma S_a \hat{\epsilon} S_b + \Gamma S_b \hat{\epsilon} S_a + \zeta_m \quad (3.110c)$$

Now plugging in our order parameter, Eq. (3.106), we have

$$\partial_t \varphi = -\gamma \epsilon' \varphi + \frac{\Gamma}{\chi_m} m + \zeta_{\varphi}(k) \quad (3.111a)$$

$$\partial_t m = \frac{\lambda}{\chi_m} \nabla^2 m - \Gamma \epsilon' \varphi + \zeta_m(k). \quad (3.111b)$$

After Fourier transform we have

$$(-i\omega + \gamma \epsilon_{\mathbf{k}}) \varphi(k, \omega) = \frac{\Gamma}{\chi_m} m(k, \omega) + \zeta_{\varphi}(k, \omega) \quad (3.112a)$$

$$\left(-i\omega + \frac{\lambda}{\chi_m} k^2\right) m(k, \omega) = -\Gamma \epsilon_{\mathbf{k}} \varphi(k, \omega) + \zeta_m(k, \omega). \quad (3.112b)$$

Let us find the characteristic frequency first. It can be found from the determinant,

$$\omega^2 + i\omega(\gamma\epsilon_{\mathbf{k}} + D_m k^2) - D_m \gamma \epsilon_{\mathbf{k}} k^2 - \frac{\Gamma^2}{\chi_m} \epsilon_{\mathbf{k}} = 0 \quad (3.113)$$

which gives us

$$\omega = \frac{1}{2} \left[-i(\gamma\epsilon_k + D_m k^2) \pm \sqrt{-(\gamma\epsilon_k + D_m k^2)^2 + 4D_m \gamma \epsilon_k k^2 + 4\frac{\Gamma^2}{\chi_m} \epsilon_k} \right] \quad (3.114a)$$

$$\simeq \pm \Gamma \sqrt{\frac{\epsilon_k}{\chi_m}} - \frac{1}{2} i(\gamma\epsilon_k + D_m k^2) \quad (3.114b)$$

$$\simeq \pm \Omega(k) - \frac{i}{2} D(k) k^2 \quad (3.114c)$$

where $D_m = \frac{\lambda}{\chi_m}$, $\Omega(k) = c_0 \sqrt{\epsilon_k}$, $D(k) = (\gamma\epsilon_k + D_m k^2)/k^2$, and $c_0 = \frac{\Gamma}{\sqrt{\chi_m}}$.

Rewriting the equations of motion, we have

$$\begin{pmatrix} \varphi(k, \omega) \\ m(k, \omega) \end{pmatrix} = \frac{1}{-\omega^2 + \Omega(k)^2 - i\omega(D(k)k^2)} \times \begin{pmatrix} -i\omega + D_m k^2 & \frac{\Gamma}{\chi_m} \\ -\Gamma \epsilon_k & -i\omega + \gamma \epsilon_k \end{pmatrix} \begin{pmatrix} \zeta_\varphi(k, \omega) \\ \zeta_m(k, \omega) \end{pmatrix}. \quad (3.115)$$

Using the noise correlations,

$$I_{\zeta_\varphi \zeta_\varphi} = \langle \zeta_\varphi(k, \omega) \zeta_\varphi(-k, -\omega) \rangle = 2k_B T \gamma \quad (3.116)$$

$$I_{\zeta_m \zeta_m} = \langle \zeta_m(k, \omega) \zeta_m(-k, -\omega) \rangle = 2k_B T \lambda k^2 \quad (3.117)$$

$$(3.118)$$

we can obtain correlation functions,

$$C_{\varphi\varphi} = \frac{1}{(\omega^2 - \omega(k)^2)^2 + \omega^2 D(k)^2 k^4} \left[(\omega^2 + (D_m k^2)^2) I_{\zeta_\varphi \zeta_\varphi} + \left(\frac{\Gamma}{\chi_m} \right)^2 I_{\zeta_m \zeta_m} \right] \quad (3.119a)$$

$$= \frac{2k_B T}{(\omega^2 - \omega(k)^2)^2 + \omega^2 D(k)^2 k^4} \left[\gamma(\omega^2 + (D_m k^2)^2) + \left(\frac{\Gamma}{\chi_m} \right)^2 \lambda k^2 \right] \quad (3.119b)$$

$$\simeq \frac{2k_B T}{k^2} \frac{\gamma \omega^2 k^2 + D_m c_0^2 k^4}{(\omega^2 - \omega(k)^2)^2 + \omega^2 D(k)^2 k^4} \quad (3.119c)$$

$$C_{mm} = \frac{1}{(\omega^2 - \omega(k)^2)^2 + \omega^2 D(k)^2 k^4} \left[(\Gamma \epsilon_k)^2 I_{\zeta_\varphi \zeta_\varphi} + (\omega^2 + \gamma^2 \epsilon_k^2) I_{\zeta_m \zeta_m} \right] \quad (3.119d)$$

$$= \frac{2k_B T}{(\omega^2 - \omega(k)^2)^2 + \omega^2 D(k)^2 k^4} \left[\gamma(\Gamma \epsilon_k)^2 + \lambda k^2 (\omega^2 k^2 + \gamma^2 \epsilon_k^2) \right] \quad (3.119e)$$

$$\simeq \frac{2k_B T \chi_m (\gamma c_0^2 \epsilon_k^2 + D_m \omega^2 k^2)}{(\omega^2 - \omega(k)^2)^2 + \omega^2 D(k)^2 k^4} \quad (3.119f)$$

$$C_{\varphi m} = \frac{1}{(\omega^2 - \omega(k)^2)^2 + \omega^2 D(k)^2 k^4} \left[(-i\omega + D_m k^2)(-\Gamma \epsilon_k) I_{\zeta_\varphi \zeta_\varphi} + \frac{\Gamma}{\chi_m} (i\omega + \gamma \epsilon_k) I_{\zeta_m \zeta_m} \right] \quad (3.119g)$$

$$= \frac{2k_B T}{(\omega^2 - \omega(k)^2)^2 + \omega^2 D(k)^2 k^4} \left[-\gamma(-i\omega + D_m k^2) \Gamma \epsilon_k + \frac{\Gamma}{\chi_m} (i\omega + \gamma \epsilon_k) \lambda k^2 \right] \quad (3.119h)$$

$$= \frac{2k_B T}{(\omega^2 - \omega(k)^2)^2 + \omega^2 D(k)^2 k^4} \left[i\omega \Gamma (\gamma \epsilon_k + D_m k^2) \right] \quad (3.119i)$$

$$= i \frac{2k_B T \omega \Gamma D(k) k^2}{(\omega^2 - \omega(k)^2)^2 + \omega^2 D(k)^2 k^4} \quad (3.119j)$$

Note that the above correlation functions are similar to those of the planar magnet obtained from Ref. [150].

3.5.3.3 Commensurate phase

The main difference between commensurate and incommensurate phases are the pinning term whose origin is the orthorhombic distortion. The main consequence of the pinning term is opening up the gap at the spin wave excitation.

With strong pinning term, the equation of motion becomes,

$$\partial_t \varphi = -\gamma(\epsilon_k \varphi + 2D_{ab} \sin(2\varphi + Qa)) + \frac{\Gamma}{\chi_m} m + \zeta_\theta(k) \quad (3.120)$$

$$\partial_t m = \frac{\lambda}{\chi_m} \nabla^2 m - \Gamma(\epsilon_k \varphi + 2D_{ab} \sin(2\varphi + Qa)) + \zeta_m(k). \quad (3.121)$$

Now replacing φ with θ using $\theta = 2\varphi - Qa$,

$$\partial_t \theta = -\gamma \epsilon_k \theta - 4\gamma D_{ab} \sin \theta + 2 \frac{\Gamma}{\chi_m} m + \zeta_\theta(k) \quad (3.122)$$

$$\partial_t m = \frac{\lambda}{\chi_m} \nabla^2 m - \frac{1}{2} \Gamma \epsilon_k \theta - 2\Gamma D_{ab} \sin \theta + \zeta_m(k). \quad (3.123)$$

where we multiplied 2 for θ equation. The above equations resemble the sine-Gordon equation and in general the nonlinearity should be considered. In simple approximation, however, since θ is small in commensurate phase, we can expand sine term in θ . This gives us,

$$\partial_t \theta = -\gamma(\epsilon_k + 4D_{ab})\theta + 2 \frac{\Gamma}{\chi_m} m + \zeta_\theta(k) \quad (3.124)$$

$$\partial_t m = \frac{\lambda}{\chi_m} \nabla^2 m - \frac{1}{2} \Gamma(\epsilon_k + 4D_{ab})\theta + \zeta_m(k). \quad (3.125)$$

which are linear in θ and m . Therefore we can find the correlation functions straightforwardly as before. Again we take Fourier transform and write the above equation in matrix form.

$$\begin{pmatrix} \theta(k, \omega) \\ m(k, \omega) \end{pmatrix} = \frac{1}{-\omega^2 + \Omega_G(k)^2 - i\omega(D_g(k)k^2)} \times \begin{pmatrix} -i\omega + D_m k^2 & \frac{2\Gamma}{\chi_m} \\ -\frac{1}{2}\Gamma(\epsilon_k + 4D_{ab}) & -i\omega + \gamma(\epsilon_k + 4D_{ab}) \end{pmatrix} \begin{pmatrix} \zeta_\theta(k, \omega) \\ \zeta_m(k, \omega) \end{pmatrix} \quad (3.126)$$

where $D_g(k) = (\gamma(\epsilon_k + 4D_{ab}) + D_m k^2)/k^2$, $\Omega_g(k) = c_0 \sqrt{\epsilon_k + 4D_{ab}}$ and $c_0 = \frac{\Gamma}{\sqrt{\chi_m}}$.

Using the noise correlations,

$$I_{\zeta_\theta \zeta_\theta} = \langle \zeta_\theta(k, \omega) \zeta_\theta(-k, -\omega) \rangle = 2k_B T \gamma \quad (3.127)$$

$$I_{\zeta_m \zeta_m} = \langle \zeta_m(k, \omega) \zeta_m(-k, -\omega) \rangle = 2k_B T \lambda k^2 \quad (3.128)$$

$$(3.129)$$

the similar calculation from the previous section gives us,

$$C_{\theta\theta} \simeq \frac{2k_B T}{k^2} \frac{\gamma \omega^2 k^2 + D_m c_0^2 k^4}{(\omega^2 - \Omega_g(k)^2)^2 + \omega^2 D_g(k)^2 k^4} \quad (3.130)$$

$$C_{mm} \simeq \frac{2k_B T \chi_m (\gamma c_0^2 (\epsilon_k + g)^2 + D_m \omega^2 k^2)}{(\omega^2 - \Omega_g(k)^2)^2 + \omega^2 D_g(k)^2 k^4} \quad (3.131)$$

$$C_{\theta m} = i \frac{2k_B T \omega \Gamma D_g(k) k^2}{(\omega^2 - \Omega_g(k)^2)^2 + \omega^2 D_g(k)^2 k^4} \quad (3.132)$$

Note that the dispersion relation in incommensurate is gapless while it is gapped in commensurate. This result is consistent with the mean field result as expected. Therefore we have a good agreement between the mean-field calculation and the hydrodynamic calculation.

3.6 Summary and Conclusion

To conclude, we studied Fe_{1+y}Te , a parent material of iron based superconductor. We constructed our model based on the theory by Turner *et al.* with inclusion of the single ion anisotropy. The single ion anisotropy originated from the magnetoelastic coupling from which we mapped out the phase diagram of magneto-structural transition. We showed the existence of the first order magneto-structural transition at certain range of parameters. At low temperature, the commensurate bi-collinear state and the incommensurate spin-spiral were obtained from our model as well as the excitation spectrum which was consistent with the experimental observations. The commensurate-incommensurate transition was also analyzed. Finally, we computed dynamic structure functions at paramagnetic states and found the qualitative agreement with the recent experiments. The correlation function of Goldstone mode in magnetically ordered state is also computed.

Chapter 4

Conclusions and outlook

In this thesis, the finite momentum phases of degenerate atomic gas and FeTe, a parent material of iron superconductors are investigated.

In particular, we studied a degenerate gas of two species bosonic atoms interacting through p -wave Feshbach resonance, as realized in ^{85}Rb - ^{87}Rb mixture. We mapped out the corresponding phase diagram and thermodynamic properties of the phases as a function of temperature, atom number, and Feshbach resonance detuning. We also analyzed the nature of corresponding phase transitions.

Our main finding is that at intermediate detuning such atomic quantum gas generically exhibits an atomic-molecular superfluid (AMSF), a finite momentum state with atoms condensed at a finite tunable momentum $\mathbf{Q}(\nu)$ along a direction set by the angular momentum axis of the molecular condensate. This AMSF state undergoes quantum phase transitions described by a quantum de Gennes model into a molecular p -wave (orbital spinor-1) superfluid (MSF) and into an s -wave atomic superfluid (ASF) at large negative and positive detunings, respectively. A magnetic field can be used to tune the modulation wavevector of the AMSF between zero and a value set by interactions as well as to drive quantum phase transitions in this rich system.

On the other subject, we studied Fe_{1+y} , a self-doped parent material of iron superconductors, based on the model suggested by Turner *et al.*. We found that a single ion anisotropy which is derived from the magnetoelastic coupling plays a central role describing Fe_{1+y}Te . With single-ion anisotropy, we computed the mean-field spin-wave excitations from the Holstein-Primakoff theory

that show the correct gap structure, gapped in commensurate phase and gapless in incommensurate phase. We also study the magneto-structural transition prevalent in iron-based superconductors. We found that our model shows the first order transition from tetragonal-paramagnet to orthorhombic spin spiral phase that is observed by several experiments. Furthermore we explain the commensurate-incommensurate transition which is unique in FeTe among other iron-based superconductors. Finally we computed the dynamic structure function that qualitatively explains the recent experimental data. Our dynamic structure function showed the incommensurate-commensurate transition near T_N .

There are possible directions of extending our work. First of all, incorporating the optical lattice in the degenerate gas with p -wave Feshbach resonance is a natural direction. It is also attracting since optical lattice can enhance the chance of realizing the suggested system by suppressing the three-body loss which is the main obstacle to the experiment. Furthermore the possible spontaneous vortex lattice phase that can arise from spin-1 MSF and its effect on other phases might be interesting.

For FeTe, extending our model to the superconducting compound will be interesting. By considering the superconducting order parameter, the effect of single ion anisotropy and the commensurate-incommensurate might give a hint to the superconducting mechanism of FeTe which might be different to that of FeAs due to the lack of nesting.

Bibliography

- [1] R. E. Peierls. Quantum theory of solids. Oxford University Press, New York/London, 1955.
- [2] G. Grüner. The dynamics of charge-density waves. Reviews of Modern Physics, 60:1129–1181, October 1988.
- [3] G. Grüner. The dynamics of spin-density waves. Reviews of Modern Physics, 66:1–24, January 1994.
- [4] Eugene Demler, Subir Sachdev, and Ying Zhang. Spin-Ordering Quantum Transitions of Superconductors in a Magnetic Field. Physical Review Letters, 87:067202, July 2001.
- [5] Sudip Chakravarty, R. Laughlin, Dirk Morr, and Chetan Nayak. Hidden order in the cuprates. Physical Review B, 63(9), January 2001.
- [6] Yoichi Kamihara, Takumi Watanabe, Masahiro Hirano, and Hideo Hosono. Iron-based layered superconductor $\text{La}[\text{O}(1-x)\text{F}(x)]\text{FeAs}$ ($x = 0.05\text{--}0.12$) with $T(c) = 26$ K. Journal of the American Chemical Society, 130:3296–7, March 2008.
- [7] Johnpierre Paglione and Richard L. Greene. High-temperature superconductivity in iron-based materials. Nature Physics, 6:645–658, August 2010.
- [8] Peter Fulde and Richard A. Ferrell. Superconductivity in a Strong Spin-Exchange Field. Physical Review, 135(3A):A550–A563, August 1964.
- [9] A. I. Larkin and Yu. N. Ovchinnikov. Inhomogeneous state of superconductors. Sov. Phys. JETP, 20:762, 1965.
- [10] Markus Greiner, Olaf Mandel, Tilman Esslinger, Theodor W Hänsch, and Immanuel Bloch. Quantum phase transition from a superfluid to a Mott insulator in a gas of ultracold atoms. Nature, 415:39–44, January 2002.
- [11] Matthew P. A. Fisher, G. Grinstein, and Daniel S. Fisher. Boson localization and the superfluid-insulator transition. Physical Review B, 40:546–570, July 1989.
- [12] D. Jaksch, C. Bruder, J. Cirac, C. Gardiner, and P. Zoller. Cold Bosonic Atoms in Optical Lattices. Physical Review Letters, 81:3108–3111, October 1998.
- [13] Herman Feshbach. A unified theory of nuclear reactions. II. Annals of Physics, 19:287–313, August 1962.

- [14] S. Inouye, M. R. Andrews, J. Stenger, H.-J. Miesner, D. M. Stamper-Kurn, and W. Ketterle. Observation of Feshbach resonances in a Bose-Einstein condensate. *392:151–154*, March 1998.
- [15] C. A. Regal, M. Greiner, and D. S. Jin. Observation of Resonance Condensation of Fermionic Atom Pairs. *Physical Review Letters*, 92, January 2004.
- [16] M. Zwierlein, C. Stan, C. Schunck, S. Raupach, A. Kerman, and W. Ketterle. Condensation of Pairs of Fermionic Atoms near a Feshbach Resonance. *Physical Review Letters*, 92:120403, March 2004.
- [17] J. Kinast, S. Hemmer, M. Gehm, A. Turlapov, and J. Thomas. Evidence for Superfluidity in a Resonantly Interacting Fermi Gas. *Physical Review Letters*, 92:150402, April 2004.
- [18] C Chin, M Bartenstein, A Altmeyer, S Riedl, S Jochim, J Hecker Denschlag, and R Grimm. Observation of the pairing gap in a strongly interacting Fermi gas. *Science*, 305:1128–30, August 2004.
- [19] G. B. Partridge, K. E. Strecker, R. I. Kamar, M. W. Jack, and R. G. Hulet. Molecular Probe of Pairing in the BEC-BCS Crossover. *Physical Review Letters*, 95:020404, July 2005.
- [20] M W Zwierlein, J R Abo-Shaer, A Schirotzek, C H Schunck, and W Ketterle. Vortices and superfluidity in a strongly interacting Fermi gas. *Nature*, 435:1047–51, June 2005.
- [21] E. Timmermans, P. Tommasini, M. Hussein, and A. Kerman. Feshbach resonances in atomic Bose-Einstein condensates. *Physics Reports*, 315:199–230, 1999.
- [22] K. Dieckmann, C. A. Stan, S. Gupta, Z. Hadzibabic, C. H. Schunck, and W. Ketterle. Decay of an Ultracold Fermionic Lithium Gas near a Feshbach Resonance. *Physical Review Letters*, 89:203201, October 2002.
- [23] K M O’Hara, S L Hemmer, M E Gehm, S R Granade, and J E Thomas. Observation of a strongly interacting degenerate Fermi gas of atoms. *Science*, 298:2179–82, December 2002.
- [24] T. Bourdel, J. Cubizolles, L. Khaykovich, K. M. F. Magalhães, S. J. J. M. F. Kokkelmans, G. V. Shlyapnikov, and C. Salomon. Measurement of the Interaction Energy near a Feshbach Resonance in a ${}^6\text{Li}$ Fermi Gas. *Physical Review Letters*, 91:020402, July 2003.
- [25] Kevin E. Strecker, Guthrie B. Partridge, and Randall G. Hulet. Conversion of an Atomic Fermi Gas to a Long-Lived Molecular Bose Gas. *Physical Review Letters*, 91:080406, August 2003.
- [26] R.A. Duine and H.T.C. Stoof. Atom-molecule coherence in Bose gases. *Physics Reports*, 396:115–195, June 2004.
- [27] P. Nozieres and S. Schmitt-Rink. Bose condensation in an attractive fermion gas: From weak to strong coupling superconductivity. *Journal of Low Temperature Physics*, 59:195–211, May 1985.
- [28] C. Sá de Melo, Mohit Randeria, and Jan Engelbrecht. Crossover from BCS to Bose superconductivity: Transition temperature and time-dependent Ginzburg-Landau theory. *Physical Review Letters*, 71:3202–3205, November 1993.

- [29] M. Holland, S. Kokkelmans, M. Chiofalo, and R. Walser. Resonance Superfluidity in a Quantum Degenerate Fermi Gas. Physical Review Letters, 87:120406, August 2001.
- [30] Y. Ohashi and A. Griffin. BCS-BEC Crossover in a Gas of Fermi Atoms with a Feshbach Resonance. Physical Review Letters, 89:130402, September 2002.
- [31] A. Andreev, V. Gurarie, and L. Radzihovsky. Nonequilibrium Dynamics and Thermodynamics of a Degenerate Fermi Gas Across a Feshbach Resonance. Physical Review Letters, 93:130402, September 2004.
- [32] J. Levinsen and V. Gurarie. Properties of strongly paired fermionic condensates. Physical Review A, 73:053607, May 2006.
- [33] V. Gurarie and L. Radzihovsky. Resonantly paired fermionic superfluids. Annals of Physics, 322:2–119, January 2007.
- [34] Leo Radzihovsky, Jae Park, and Peter Weichman. Superfluid Transitions in Bosonic Atom-Molecule Mixtures near a Feshbach Resonance. Physical Review Letters, 92:160402, April 2004.
- [35] Leo Radzihovsky, Peter B. Weichman, and Jae I. Park. Superfluidity and phase transitions in a resonant Bose gas. Annals of Physics, 323:2376–2451, October 2008.
- [36] M. Romans, R. Duine, Subir Sachdev, and H. Stoof. Quantum Phase Transition in an Atomic Bose Gas with a Feshbach Resonance. Physical Review Letters, 93:020405, July 2004.
- [37] S. Diehl, M. Baranov, A. Daley, and P. Zoller. Quantum field theory for the three-body constrained lattice Bose gas. I. Formal developments. Physical Review B, 82:064509, August 2010.
- [38] S. Diehl, M. Baranov, A. Daley, and P. Zoller. Quantum field theory for the three-body constrained lattice Bose gas. II. Application to the many-body problem. Physical Review B, 82:064510, August 2010.
- [39] S. Papp. Experiments with a two-species Bose-Einstein condensate utilizing widely tunable interparticle interactions. PhD thesis, University of Colorado, 2007.
- [40] Clifford W. Hicks, Thomas M. Lippman, Martin E. Huber, Zhi-An Ren, Jie Yang, Zhong-Xian Zhao, and Kathryn A. Moler. Limits on the Superconducting Order Parameter in $\text{NdFeAsO}_{1-x}\text{F}_y$ from Scanning SQUID Microscopy. Journal of the Physical Society of Japan, 78(1):013708, December 2008.
- [41] Xiaohang Zhang, Yoon Oh, Yong Liu, Liqin Yan, Kee Kim, Richard Greene, and Ichiro Takeuchi. Observation of the Josephson Effect in $\text{Pb/Ba}_{1-x}\text{K}_x\text{Fe}_2\text{As}_2$ Single Crystal Junctions. Physical Review Letters, 102(14), April 2009.
- [42] C.-T. Chen, C. C. Tsuei, M. B. Ketchen, Z.-A. Ren, and Z. X. Zhao. Integer and half-integer flux-quantum transitions in a niobium-iron pnictide loop. Nature Physics, 6(4):260–264, February 2010.
- [43] C. A. Regal, C. Ticknor, J. L. Bohn, and D. S. Jin. Tuning p-Wave Interactions in an Ultracold Fermi Gas of Atoms. Physical Review Letters, 90:053201, February 2003.

- [44] J. P. Gaebler, J. T. Stewart, J. L. Bohn, and D. S. Jin. p-Wave Feshbach Molecules. Physical Review Letters, 98:200403, May 2007.
- [45] Wei Bao, Y. Qiu, Q. Huang, M. A. Green, P. Zajdel, M. R. Fitzsimmons, M. Zhernenkov, S. Chang, Minghu Fang, B. Qian, E. K. Vehstedt, Jinhu Yang, H. M. Pham, L. Spinu, and Z. Q. Mao. Tunable $(\delta\pi, \delta\pi)$ -Type Antiferromagnetic Order in α -Fe(Te,Se) Superconductors. Physical Review Letters, 102:247001, June 2009.
- [46] Shiliang Li, Clarina de la Cruz, Q. Huang, Y. Chen, J. W. Lynn, Jiangping Hu, Yi-Lin Huang, Fong-Chi Hsu, Kuo-Wei Yeh, Maw-Kuen Wu, and Pengcheng Dai. First-order magnetic and structural phase transitions in $\text{Fe}_{1+y}\text{Se}_x\text{Te}_{1-x}$. Physical Review B, 79:054503, February 2009.
- [47] Alaska Subedi, Lijun Zhang, D J Singh, and M H Du. Density functional study of FeS , FeSe , and FeTe : Electronic structure , magnetism , phonons , and superconductivity. pages 1–6, 2008.
- [48] Y. Xia, D. Qian, L. Wray, D. Hsieh, G. F. Chen, J. L. Luo, N. L. Wang, and M. Z. Hasan. Fermi Surface Topology and Low-Lying Quasiparticle Dynamics of Parent $\text{Fe}_{1+x}\text{Te/Se}$ Superconductor. Physical Review Letters, 103:037002, July 2009.
- [49] Ari M. Turner, Fa Wang, and Ashvin Vishwanath. Kinetic magnetism and orbital order in iron telluride. Physical Review B, 80:224504, December 2009.
- [50] Chen Fang, B. Andrei Bernevig, and Jiangping Hu. Theory of magnetic order in $\text{Fe}_{1+y}\text{Te}_{1-x}\text{Se}_x$. EPL (Europhysics Letters), 86:67005, June 2009.
- [51] Wei-Guo Yin, Chi-Cheng Lee, and Wei Ku. Unified Picture for Magnetic Correlations in Iron-Based Superconductors. Physical Review Letters, 105:107004, September 2010.
- [52] Lijun Zhang, D. Singh, and M. Du. Density functional study of excess Fe in Fe_{1+x}Te : Magnetism and doping. Physical Review B, 79:012506, January 2009.
- [53] Fengjie Ma, Wei Ji, Jiangping Hu, Zhong-Yi Lu, and Tao Xiang. First-Principles Calculations of the Electronic Structure of Tetragonal α -FeTe and α -FeSe Crystals: Evidence for a Bicollinear Antiferromagnetic Order. Physical Review Letters, 102:177003, April 2009.
- [54] M H Anderson, J R Ensher, M R Matthews, C E Wieman, and E A Cornell. Observation of bose-einstein condensation in a dilute atomic vapor. Science, 269:198–201, July 1995.
- [55] K. Davis, M. Mewes, M. Andrews, N. van Druten, D. Durfee, D. Kurn, and W. Ketterle. Bose-Einstein Condensation in a Gas of Sodium Atoms. Physical Review Letters, 75:3969–3973, November 1995.
- [56] Tin-Lun Ho and Roberto Diener. Fermion Superfluids of Nonzero Orbital Angular Momentum near Resonance. Physical Review Letters, 94:090402, March 2005.
- [57] V. Gurarie, L. Radzihovsky, and A. V. Andreev. Quantum Phase Transitions across a p-Wave Feshbach Resonance. Physical Review Letters, 94:230403, June 2005.
- [58] Chi-Ho Cheng and S.-K. Yip. Anisotropic Fermi Superfluid via p-Wave Feshbach Resonance. Physical Review Letters, 95:070404, August 2005.

- [59] J. Zhang, E. G. M. van Kempen, T. Bourdel, L. Khaykovich, J. Cubizolles, F. Chevy, M. Teichmann, L. Tarruell, S. J. J. M. F. Kokkelmans, and C. Salomon. P -wave Feshbach resonances of ultracold ^6Li . Physical Review A, 70:030702, September 2004.
- [60] J. Levinsen, N. R. Cooper, and V. Gurarie. Stability of fermionic gases close to a p -wave Feshbach resonance. Physical Review A, 78:063616, December 2008.
- [61] S. L. Cornish, N. R. Claussen, J. L. Roberts, E. A. Cornell, and C. E. Wieman. Stable ^{85}Rb Bose-Einstein Condensates with Widely Tunable Interactions. Physical Review Letters, 85:1795–1798, August 2000.
- [62] V. N. Efimov. Weakly-bound states of three resonantly-interacting particles. Sov. J. Nucl. Phys., 12:589, 1971.
- [63] Sourish Basu and Erich Mueller. Stability of bosonic atomic and molecular condensates near a Feshbach resonance. Physical Review A, 78:053603, November 2008.
- [64] J. Roberts, N. Claussen, S. Cornish, E. Donley, E. Cornell, and C. Wieman. Controlled Collapse of a Bose-Einstein Condensate. Physical Review Letters, 86:4211–4214, May 2001.
- [65] N Syassen, D M Bauer, M Lettner, T Volz, D Dietze, J J García-Ripoll, J I Cirac, G Rempe, and S Dürr. Strong dissipation inhibits losses and induces correlations in cold molecular gases. Science (New York, N.Y.), 320:1329–31, June 2008.
- [66] H. A. Bethe. Handbuch der Physik. Second edition, 1933.
- [67] S. Ejima, M. Bhaseen, M. Hohenadler, F. Essler, H. Fehske, and B. Simons. Ising Deconfinement Transition between Feshbach-Resonant Superfluids. Physical Review Letters, 106:015303, January 2011.
- [68] M. J. Bhaseen, A. O. Silver, M. Hohenadler, and B. D. Simons. Feshbach Resonance in Optical Lattices and the Quantum Ising Model. Physical Review Letters, 103:265302, December 2009.
- [69] Lars Bonnes and Stefan Wessel. Pair Superfluidity of Three-Body Constrained Bosons in Two Dimensions. Physical Review Letters, 106:185302, May 2011.
- [70] S. Papp, J. Pino, and C. Wieman. Tunable Miscibility in a Dual-Species Bose-Einstein Condensate. Physical Review Letters, 101:040402, July 2008.
- [71] Leo Radzihovsky and Sungsoo Choi. p-Wave Resonant Bose Gas: A Finite-Momentum Spinor Superfluid. Physical Review Letters, 103:095302, August 2009.
- [72] A. Kuklov. Unconventional Strongly Interacting Bose-Einstein Condensates in Optical Lattices. Physical Review Letters, 97(110405), September 2006.
- [73] W. Liu and Congjun Wu. Atomic matter of nonzero-momentum Bose-Einstein condensation and orbital current order. Physical Review A, 74:013607, July 2006.
- [74] A. F. Andreev and I. M. Lifshitz. Quantum theory of defects in crystals. Sov. Phys. JETP, 29:1107, 1969.
- [75] G. V. Chester. Speculations on Bose-Einstein Condensation and Quantum Crystals. Physical Review A, 2:256–258, July 1970.

- [76] A. J. Leggett. Can a Solid Be “Superfluid”? Physical Review Letters, 25:1543–1546, November 1970.
- [77] E Kim and M H W Chan. Probable observation of a supersolid helium phase. Nature, 427:225–7, January 2004.
- [78] E Kim and M H W Chan. Observation of superflow in solid helium. Science, 305:1941–4, September 2004.
- [79] J. Stenger, S. Inouye, D. M. Stamper-Kurn, H.-J. Miesner, A. P. Chikkatur, and W. Ketterle. Spin domains in ground-state Bose-Einstein condensates. 396:345–348, November 1998.
- [80] A. Görlitz, T. Gustavson, A. Leanhardt, R. Löw, A. Chikkatur, S. Gupta, S. Inouye, D. Pritchard, and W. Ketterle. Sodium Bose-Einstein Condensates in the $F=2$ State in a Large-Volume Optical Trap. Physical Review Letters, 90:090401, March 2003.
- [81] M.-S. Chang, C. Hamley, M. Barrett, J. Sauer, K. Fortier, W. Zhang, L. You, and M. Chapman. Observation of Spinor Dynamics in Optically Trapped Rb87 Bose-Einstein Condensates. Physical Review Letters, 92:140403, April 2004.
- [82] Ming-Shien Chang, Qishu Qin, Wenxian Zhang, Li You, and Michael S. Chapman. Coherent spinor dynamics in a spin-1 Bose condensate. Nature Physics, 1:111–116, October 2005.
- [83] M. Vengalattore, S. R. Leslie, J. Guzman, and D. M. Stamper-Kurn. Spontaneously Modulated Spin Textures in a Dipolar Spinor Bose-Einstein Condensate. Physical Review Letters, 100:170403, May 2008.
- [84] Tin-Lun Ho. Spinor Bose Condensates in Optical Traps. Physical Review Letters, 81:742–745, July 1998.
- [85] Tetsuo Ohmi and Kazushige Machida. Bose-Einstein Condensation with Internal Degrees of Freedom in Alkali Atom Gases. Journal of the Physics Society Japan, 67:1822–1825, June 1998.
- [86] D. Stamper-Kurn, M. Andrews, A. Chikkatur, S. Inouye, H.-J. Miesner, J. Stenger, and W. Ketterle. Optical Confinement of a Bose-Einstein Condensate. Physical Review Letters, 80:2027–2030, March 1998.
- [87] M. Matthews, D. Hall, D. Jin, J. Ensher, C. Wieman, E. Cornell, F. Dalfovo, C. Minniti, and S. Stringari. Dynamical Response of a Bose-Einstein Condensate to a Discontinuous Change in Internal State. Physical Review Letters, 81:243–247, July 1998.
- [88] C. Law, H. Pu, and N. Bigelow. Quantum Spins Mixing in Spinor Bose-Einstein Condensates. Physical Review Letters, 81:5257–5261, December 1998.
- [89] Tin-Lun Ho and Sung Yip. Fragmented and Single Condensate Ground States of Spin-1 Bose Gas. Physical Review Letters, 84:4031–4034, May 2000.
- [90] Fei Zhou. Spin Correlation and Discrete Symmetry in Spinor Bose-Einstein Condensates. Physical Review Letters, 87:080401, August 2001.
- [91] Eugene Demler and Fei Zhou. Spinor Bosonic Atoms in Optical Lattices: Symmetry Breaking and Fractionalization. Physical Review Letters, 88:163001, April 2002.

- [92] Ryan Barnett, Ari Turner, and Eugene Demler. Classifying Novel Phases of Spinor Atoms. Physical Review Letters, 97:180412, November 2006.
- [93] Subroto Mukerjee, Cenke Xu, and J. Moore. Topological Defects and the Superfluid Transition of the $s=1$ Spinor Condensate in Two Dimensions. Physical Review Letters, 97:120406, September 2006.
- [94] J. Mur-Petit, M. Guilleumas, A. Polls, A. Sanpera, M. Lewenstein, K. Bongs, and K. Senstock. Dynamics of $F=1$ ^{87}Rb condensates at finite temperatures. Physical Review A, 73:013629, January 2006.
- [95] Austen Lamacraft. Quantum Quenches in a Spinor Condensate. Physical Review Letters, 98:160404, April 2007.
- [96] Subroto Mukerjee, Cenke Xu, and J. Moore. Dynamical models and the phase ordering kinetics of the $s=1$ spinor condensate. Physical Review B, 76:104519, September 2007.
- [97] Simon Fölling, Artur Widera, Torben Müller, Fabrice Gerbier, and Immanuel Bloch. Formation of Spatial Shell Structure in the Superfluid to Mott Insulator Transition. Physical Review Letters, 97:060403, August 2006.
- [98] Gretchen K Campbell, Jongchul Mun, Micah Boyd, Patrick Medley, Aaron E Leanhardt, Luis G Marcassa, David E Pritchard, and Wolfgang Ketterle. Imaging the Mott insulator shells by using atomic clock shifts. Science, 313:649–52, August 2006.
- [99] R. Barankov, C. Lannert, and S. Vishveshwara. Coexistence of superfluid and Mott phases of lattice bosons. Physical Review A, 75:063622, June 2007.
- [100] P. G. de Gennes and J. Prost. The Physics of Liquid Crystals. Oxford University Press, 2nd ed. edition, 1995.
- [101] Yean-An Liao, Ann Sophie C Rittner, Tobias Paprotta, Wenhui Li, Guthrie B Partridge, Randall G Hulet, Stefan K Baur, and Erich J Mueller. Spin-imbalance in a one-dimensional Fermi gas. Nature, 467:567–9, September 2010.
- [102] A. Bianchi, R. Movshovich, C. Capan, P. G. Pagliuso, and J. L. Sarrao. Possible Fulde-Ferrell-Larkin-Ovchinnikov Superconducting State in CeCoIn_5 . Physical Review Letters, 91:187004, October 2003.
- [103] T. Mizushima, K. Machida, and M. Ichioka. Direct Imaging of Spatially Modulated Superfluid Phases in Atomic Fermion Systems. Physical Review Letters, 94:060404, February 2005.
- [104] Daniel Sheehy and Leo Radzihovsky. BEC-BCS Crossover in Magnetized Feshbach-Resonantly Paired Superfluids. Physical Review Letters, 96:060401, February 2006.
- [105] Daniel E. Sheehy and Leo Radzihovsky. BEC-BCS crossover, phase transitions and phase separation in polarized resonantly-paired superfluids. Annals of Physics, 322:1790–1924, August 2007.
- [106] Leo Radzihovsky and Daniel E Sheehy. Imbalanced Feshbach-resonant Fermi gases. Reports on Progress in Physics, 73:076501, July 2010.

- [107] H. J. Kimble. Quantum Fluctuations in quantum optics - squeezing and related phenomena, 1992.
- [108] C Orzel, A K Tuchman, M L Fenselau, M Yasuda, and M A Kasevich. Squeezed states in a Bose-Einstein condensate. Science, 291:2386–9, March 2001.
- [109] Leo Radzihovsky and Ashvin Vishwanath. Quantum Liquid Crystals in an Imbalanced Fermi Gas: Fluctuations and Fractional Vortices in Larkin-Ovchinnikov States. Physical Review Letters, 103:010404, July 2009.
- [110] Leo Radzihovsky. Fluctuations and phase transitions in Larkin-Ovchinnikov liquid-crystal states of a population-imbalanced resonant Fermi gas. Physical Review A, 84:023611, August 2011.
- [111] For unequal masses FR interaction is given by $H_{FR} = \alpha \hat{\phi}^\dagger \cdot \left[\frac{m_1}{m_1+m_2} \hat{\psi}_1(-i\nabla) \hat{\psi}_2 - \frac{m_2}{m_1+m_2} \hat{\psi}_2(-i\nabla) \hat{\psi}_1 \right]$ as required to preserve Galilean invariance.
- [112] L. D. Landau and E. M. Lifshitz. Quantum Physics. Butterworth-Heinemann, Oxford, 1980.
- [113] B. Esry, Chris Greene, Jr. Burke, and John Bohn. Hartree-Fock Theory for Double Condensates. Physical Review Letters, 78:3594–3597, May 1997.
- [114] Yu-Wen Lee and Yu-Li Lee. Quantum phase transition in an atomic Bose gas near a Feshbach resonance. Physical Review B, 70:224506, December 2004.
- [115] J. W. Negele and H. Orland. Quantum Many-Particle Systems. Addison-w-e edition, 1988.
- [116] Subir Sachdev and N. Read. Large N expansion for frustrated and doped quantum antiferromagnets. Int. J. Mod. Phys. B, 5:219, 1991.
- [117] Chao-Ming Jian and Hui Zhai. Paired superfluidity and fractionalized vortices in systems of spin-orbit coupled bosons. Physical Review B, 84:060508, August 2011.
- [118] For simplicity it is convenient to first consider a homogeneous bulk system or a box trap, and take into account the trap-induced local inhomogeneity using LDA, valid for large condensates and smooth trapping potential.
- [119] In the absence of an optical potential or quenched disorder that can localize atom number and induce Mott-or Bose-glass insulating phases, only Bose-condensed, superfluid ground states are expected at zero temperature.
- [120] $U_N(1)$ and $U_{\Delta N}(1)$ symmetries are associated with the total atom number $N = N_1 + N_2 + 2N_m$ and difference $\Delta N = N_1 - N_2$ conservations, respectively.
- [121] Kao-Shien Liu and Michael E. Fisher. Quantum lattice gas and the existence of a supersolid. Journal of Low Temperature Physics, 10:655–683, March 1973.
- [122] J. Kosterlitz, David Nelson, and Michael Fisher. Bicritical and tetracritical points in anisotropic antiferromagnetic systems. Physical Review B, 13:412–432, January 1976.
- [123] Pasquale Calabrese, Andrea Pelissetto, and Ettore Vicari. Multicritical phenomena in $O(n_1) \times O(n_2)$ -symmetric theories. Physical Review B, 67:054505, February 2003.

- [124] More accurately, it is not g_2 but T -matrix, i.e., scattering length a 's that matter.
- [125] In the context of conventional spinor condensate, the polar state is also termed nematic or antiferromagnetic superfluid.
- [126] P. M. Chaikin and T. C. Lubensky. Principles of Condensed Matter Physics. Cambridge University Press, 1995.
- [127] To keep the form of the Landau free energy simple, one needs to be sufficiently close to the transition boundaries (but staying outside the critical region, where local Landau mean-field expansion fails) to allow a local expansion in the order parameters.
- [128] Immanuel Bloch, Jean Dalibard, and Wilhelm Zwerger. Many-body physics with ultracold gases. Reviews of Modern Physics, 80:885–964, July 2008.
- [129] B. Halperin, T. Lubensky, and Shang-keng Ma. First-Order Phase Transitions in Superconductors and Smectic-A Liquid Crystals. Physical Review Letters, 32:292–295, February 1974.
- [130] Sidney Coleman and Erick Weinberg. Radiative Corrections as the Origin of Spontaneous Symmetry Breaking. Physical Review D, 7:1888–1910, March 1973.
- [131] Daniel Podolsky, Shailesh Chandrasekharan, and Ashvin Vishwanath. Phase transitions of $S=1$ spinor condensates in an optical lattice. Physical Review B, 80:214513, December 2009.
- [132] Egor Babaev. Vortices with Fractional Flux in Two-Gap Superconductors and in Extended Faddeev Model. Physical Review Letters, 89:067001, July 2002.
- [133] N. Mermin. The topological theory of defects in ordered media. Reviews of Modern Physics, 51:591–648, July 1979.
- [134] B. DeMarco, C. Lannert, S. Vishveshwara, and T.-C. Wei. Structure and stability of Mott-insulator shells of bosons trapped in an optical lattice. Physical Review A, 71:063601, June 2005.
- [135] Martin W Zwierlein, André Schirotzek, Christian H Schunck, and Wolfgang Ketterle. Fermionic superfluidity with imbalanced spin populations. Science, 311:492–6, January 2006.
- [136] Guthrie B Partridge, Wenhui Li, Ramsey I Kamar, Yean-An Liao, and Randall G Hulet. Pairing and phase separation in a polarized Fermi gas. Science, 311:503–5, January 2006.
- [137] Y. Shin, M. Zwierlein, C. Schunck, A. Schirotzek, and W. Ketterle. Observation of Phase Separation in a Strongly Interacting Imbalanced Fermi Gas. Physical Review Letters, 97:030401, July 2006.
- [138] S. Nascimbène, N. Navon, K. J. Jiang, L. Tarruell, M. Teichmann, J. McKeever, F. Chevy, and C. Salomon. Collective Oscillations of an Imbalanced Fermi Gas: Axial Compression Modes and Polaron Effective Mass. Physical Review Letters, 103:170402, October 2009.
- [139] E. E. Rodriguez, C. Stock, P. Zajdel, K. L. Krycka, C. F. Majkrzak, P. Zavalij, and M. A. Green. Magnetic-crystallographic phase diagram of the superconducting parent compound Fe_{1+x}Te . Physical Review B, 84:064403, August 2011.

- [140] Cengiz Åden, Gonzalo Alvarez, and Elbio Dagotto. Competing Ferromagnetic and Charge-Ordered States in Models for Manganites: The Origin of the Colossal Magnetoresistance Effect. Physical Review Letters, 98(12), March 2007.
- [141] C. Stock, E. E. Rodriguez, P. Zavalij, M. A. Green, and J. A. Rodriguez-Rivera. Interstitial iron tuning of the spin fluctuations in Fe_{1+x}Te . arXiv : 1103.1811, March 2011.
- [142] O. Lipscombe, G. Chen, Chen Fang, T. Perring, D. Abernathy, A. Christianson, Takeshi Egami, Nanlin Wang, Jiangping Hu, and Pengcheng Dai. Spin Waves in the $(\pi,0)$ Magnetically Ordered Iron Chalcogenide $\text{Fe}_{1.05}\text{Te}$. Physical Review Letters, 106:057004, February 2011.
- [143] D. Parshall, G. Chen, L. Pintschovius, D. Lamago, Th. Wolf, L. Radzihovsky, and D. Reznik. Competition between commensurate and incommensurate magnetic ordering in Fe_{1+y}Te . arXiv:1111.4236, November 2011.
- [144] R. Fernandes, A. Chubukov, J. Knolle, I. Eremin, and J. Schmalian. Preemptive nematic order, pseudogap, and orbital order in the iron pnictides. Physical Review B, 85:024534, January 2012.
- [145] V. Pokrovsky *et al.*
- [146] L. Messio, C. Lhuillier, and G. Misguich. Lattice symmetries and regular magnetic orders in classical frustrated antiferromagnets. Physical Review B, 83(18), May 2011.
- [147] I. Paul, A. Cano, and K. Sengupta. Magnetoelastic effects in iron telluride. Physical Review B, 83:115109, March 2011.
- [148] M. Kim, R. Fernandes, A. Kreyssig, J. Kim, A. Thaler, S. BudãĀĹko, P. Canfield, R. McQueeney, J. Schmalian, and A. Goldman. Character of the structural and magnetic phase transitions in the parent and electron-doped BaFe_2As_2 compounds. Physical Review B, 83:134522, April 2011.
- [149] K. Prokeř, S. MataĀĹař, L. Harnagea, S. Singh, S. Wurmehl, D. Argyriou, and B. Bũchner. Effect of Co substitution on the magnetic order in $\text{Ca}(\text{Fe}_{1-x}\text{Co}_x)_2\text{As}_2$ single crystals studied by neutron diffraction. Physical Review B, 83(10), March 2011.
- [150] B. HALPERIN and P. HOHENBERG. Hydrodynamic Theory of Spin Waves. Physical Review, 188:898–918, December 1969.
- [151] Meera M. Parish, Stefan K. Baur, Erich J. Mueller, and David A. Huse. Quasi-One-Dimensional Polarized Fermi Superfluids. Physical Review Letters, 99(25), December 2007.
- [152] C Becker, P Soltan-Panahi, J Kronjãger, S Dũrscher, K Bongs, and K Sengstock. Ultracold quantum gases in triangular optical lattices. New Journal of Physics, 12:065025, June 2010.
- [153] Leticia Tarruell, Daniel Greif, Thomas Uehlinger, Gregor Jotzu, and Tilman Esslinger. Creating, moving and merging Dirac points with a Fermi gas in a tunable honeycomb lattice. Nature, 483:302–305, March 2012.
- [154] H.-J. Grafe, D. Paar, G. Lang, N. J. Curro, G. Behr, J. Werner, J. Hamann-Borrero, C. Hess, N. Leps, R. Klingeler, and B. Bũchner. ^{75}As NMR Studies of Superconducting $\text{LaFeAsO}_{0.9}\text{F}_{0.1}$. Physical Review Letters, 101:047003, July 2008.

- [155] P. Hohenberg and B. Halperin. Theory of dynamic critical phenomena. Reviews of Modern Physics, 49:435–479, July 1977.

Appendix A

Order parameter structure of AMSF phase

As discussed in the main text, the detailed nature of the AMSF states depends on the structure (the set of reciprocal lattice vectors, \mathbf{Q}_n) of the finite-momentum atomic order parameter. However, because $\Psi_{\mathbf{Q}_n}$ depends on the details of the inter-atomic interactions and fluctuations, to determine its form in general is a nontrivial problem, as exemplified by the FFLO problem and the conventional crystallization. However, as seen in Sec.2.4, for the case of the polar AMSF_p state, the problem simplifies considerably as the energy is clearly minimized by a collinear state, with \mathbf{Q}_n parallel to Φ . Such collinear states fall into two universality classes[110], represented by the Fulde-Ferrell-like[8] and the Larkin-Ovchinnikov-like[9] single harmonic forms

$$\Psi_{\sigma}^{\text{FF}} = \Psi_{\sigma, \mathbf{Q}_{\sigma}} e^{i\mathbf{Q}_{\sigma} \cdot \mathbf{r}}, \quad (\text{A.1})$$

$$\Psi_{\sigma}^{\text{LO}} = \Psi_{\sigma, \mathbf{Q}} e^{i\mathbf{Q} \cdot \mathbf{r}} + \Psi_{\sigma, -\mathbf{Q}} e^{-i\mathbf{Q} \cdot \mathbf{r}}. \quad (\text{A.2})$$

In the FF-like (LO-like) state each species is characterized by a single \mathbf{Q} (double $\pm\mathbf{Q}$) momentum, exhibiting a uniform (periodic) atomic density.

Focusing on these two collinear (FF and LO) states, in this appendix we demonstrate that, generically (at least within the mean-field theory), it is the FF state that is energetically selected by the interactions.

To this end, we re-express the mean-field energy densities for FF and LO in terms of the

corresponding eigenmodes, $\Psi_{\pm}^{\pm Q}$, latter involving two ($\pm Q$) critical modes

$$\mathcal{E}_{\text{FF}} = (\varepsilon_{\mathbf{Q}} - |\Delta_{\mathbf{Q}}|)|\Psi_{-}^Q|^2 + \frac{1}{2}\lambda|\Psi_{-}^Q|^4, \quad (\text{A.3})$$

$$\begin{aligned} \mathcal{E}_{\text{LO}} &= (\varepsilon_{\mathbf{Q}} - |\Delta_{\mathbf{Q}}|)(|\Psi_{-}^Q|^2 + |\Psi_{-}^{-Q}|^2) \\ &+ \frac{1}{2}\lambda(|\Psi_{-}^Q|^2 + |\Psi_{-}^{-Q}|^2)^2 + \lambda'|\Psi_{-}^Q|^2|\Psi_{-}^{-Q}|^2, \end{aligned} \quad (\text{A.4})$$

where $\lambda = \frac{1}{4}(\lambda_1 + \lambda_2 + 2\lambda_{12})$ and $\lambda' = \frac{1}{4}(\lambda_1 + \lambda_2 - 2\lambda_{12})$.

These free energies thus show that the energetically preferred form of the AMSF state is determined by the coefficient λ' of last term in Eq. (A.4). For $\lambda' > 0$, i.e., $\lambda_1 + \lambda_2 > 2\lambda_{12}$, the single Q FF-like state is selected. On the other hand, for $\lambda' < 0$, i.e., $\lambda_1 + \lambda_2 < 2\lambda_{12}$, it is the LO-like state that has the lowest energy.

Combining above requirement on λ' for the stability of the LO-like state with the condition for two-species miscibility, $\lambda_1\lambda_2 > \lambda_{12}^2$, we find an inequality

$$\frac{\lambda_1 + \lambda_2}{2} < \lambda_{12} < \sqrt{\lambda_1\lambda_2} \quad (\text{A.5})$$

which for positive couplings λ_i can be shown to have a zero-range of stability. Thus, as advertised, within mean-field approximation it is the single Q FF-like AMSF state that is always energetically selected. Perhaps the LO-like AMSF form can be realized for a metastable atomic gas with $\lambda_i < 0$, as e.g., realized by a ^{87}Rb - ^{85}Rb mixture.